Unconventional Superconductivity in Strontium Ruthenate

Thomas Scaffidi
Merton College
University of Oxford

A thesis submitted for the degree of
Doctor of Philosophy in Theoretical Physics

Trinity Term 2016

Abstract

In this thesis, a weak coupling formalism is developed to study superconductivity in spin-orbit coupled, multi-orbital systems. This formalism is then applied to Sr_2RuO_4, one of the few candidates for odd-parity superconductivity. We show that spin-orbit coupling and multi-band effects are crucial to understand the physics of this material. Depending on the interaction parameters, the order parameter can either be chiral or helical. In both cases, the gap is highly anisotropic, and has accidental deep minima along certain directions, in accordance with experiments. Focusing then on the chiral case, we show that the total Chern number is -7 instead of the usually assumed $+1$. This leads to drastically different predictions for the thermal and charge Hall conductances. In particular, we show that the absence of measurable charge edge currents is not incompatible with a chiral state. Finally, we study the evolution of superconductivity in Sr_2RuO_4 under $\langle 100 \rangle$ uniaxial strain. We find a good agreement with experiments for our prediction of T_c as a function of strain. Furthermore, we find that (1) the absence of a measurable cusp of T_c at zero strain is not incompatible with a chiral state and that (2) there could be a transition to an even-parity state at larger strain close to a Van Hove singularity. We propose $H_{c,2}/T_c^2$ as a measurable quantity to identify this transition.

Contents

List of Figures

List of Tables

List of Abbreviations

ABM - Anderson-Brinkman-Morel

ARPES - Angle-resolved photo-emission spectroscopy

BCS - Bardeen-Cooper-Schrieffer

BdG - Bogolyubov-de Gennes

BEC - Bose-Einstein condensation

BW - Balian-Werthamer

CDS - Charge-density wave

DFT - Density functional theory

DMFT - Dynamical mean-field theory

DOS - Density of states

FS - Fermi surface

GL - Ginzburg-Landau

HQV - Half-quantum vortices

NMR - Nuclear magnetic resonance

OP - Order parameter

PHS - Particle-hole symmetry

RPA - Random phase approximation

RG - Renormalization group

SC - Superconductivity

SLS - Sublattice symmetry

SOC - Spin-orbit coupling

SDW - Spin-density wave

STM - Scanning tunnelling microscope

TRS - Time-reversal symmetry

TRSB - Time-reversal symmetry breaking

vHS - Van Hove singularity

Publications

During my DPhil, I have published the following articles:

1. T. Scaffidi, G. Möller, "Adiabatic Continuation of Fractional Chern Insulators to Fractional Quantum Hall States", Phys. Rev. Lett. **109**, 246805 (2012)

2. T. Scaffidi, J. C. Romers, S. H. Simon, "Pairing Symmetry and Dominant Band in Sr_2RuO_4", Phys. Rev. B **89**, 220510(R) (2014), Editors' Suggestion

3. T. Scaffidi, S. H. Simon, "Exact Solutions of Fractional Chern Insulators: Interacting Particles in the Hofstadter Model at Finite Size", Phys. Rev. B **90**, 115132 (2014)

4. T. Scaffidi, S. H. Simon, "Large Chern Number and Edge Currents in Sr_2RuO_4", Phys. Rev. Lett. **115**, 087003 (2015)

5. T. Scaffidi, Z. Ringel, "Wave Functions of Symmetry-Protected Topological Phases from Conformal Field Theories", Phys. Rev. B **93**, 115105 (2016)

6. A. Steppke, L. Zhao, M. E. Barber, T. Scaffidi, F. Jerzembeck, H. Rosner, A. S. Gibbs, Y. Maeno, S. H. Simon, A. P. Mackenzie, and C. W. Hicks, "Strong Peak in T_c of Sr_2RuO_4 Under Uniaxial Pressure", ArXiv e-prints (2016), arXiv:1604.06669

7. W. Huang, T. Scaffidi, M. Sigrist, C. Kallin, "Leggett Modes and Multi-Band Superconductivity in Sr_2RuO_4", ArXiv e-prints (2016), arXiv:1605.03800

This thesis incorporates work presented in publications 2, 4 and 6.

1. Introduction

1.1 Historical introduction

One of the most important goals of Physics is to identify universal patterns among the seemingly disparate zoology of particles and phenomena existing in Nature. The periodic table of elements and the standard model of particles are good examples of such a unified understanding. Yet, when a very large number of microscopic particles interact with each other, their behavior as a phase has to be described by a new, emergent theory, just like a large number of water molecules are described in terms of fluid mechanics rather than by the dynamics of each molecule. The next logical step is therefore to establish a "periodic table of phases of matter", i.e. a classification of all the ways in which a macroscopic number of particles can behave. In the case of water molecules, the answer is well known: they can form a gas, a liquid or various solid phases, and these different phases can be distinguished by the symmetries they obey. Similarly, electrons in solids can form various phases, including ones that exhibit highly robust quantum phenomena at a macroscopic scale, like superconductivity, which will be the topic of this thesis.

Superconductivity (SC) was discovered in 1911 by Onnes [16] when he measured a sudden drop in the resistivity of Mercury at a very low critical temperature T_c that could only be reached with liquefied Helium. It was then shown to appear in a large variety of metals, but it evaded a theoretical microscopic understanding until the 1950s and 1960s, when the Bardeen - Cooper - Schrieffer (BCS) theory of superconductivity was developed [17]. This theory showed that the microscopic mechanism behind superconductivity relies on the formation of pairs of electrons with opposite momenta called Cooper pairs. BCS showed that even an infinitesimal attractive interaction between electrons close to the Fermi level is enough to generate superconductivity. These Cooper pairs behave as one single macroscopic quantum object, the condensate, which responds coherently under electromagnetic fields. Furthermore, a gap Δ appears between the energy of the ground state and of the quasi-particle

excitations of the system.

The problem of two electrons forming a bound state over the background of other electrons can be split into different angular momenta channels. The angular momenta channels are named after the corresponding spherical harmonics s, p, d, f,... which correspond to angular momenta of squared norm $\vec{L}^2 = j(j+1)\hbar^2$ with $j = 0, 1, 2, 3, \ldots$ For the first 60 years of the study of superconductivity, all discovered superconductors had $j = 0$ and were therefore s-wave. The origin of the effective attractive interaction was shown to be the interaction of electrons with vibrations of the lattice, whose quanta are called phonons.

Starting in the seventies, several systems were shown to exhibit Cooper pairing but could not be understood using the same phononic mechanism. The superfluidity of ^{3}He discovered in 1971[18] was the first example. It then took almost ten years before two examples of such unconventional pairing were discovered in a solid state system: the heavy fermion compounds [19] and the organic superconductors [20, 21]. In 1986, a series of Copper-based quasi-two-dimensional materials called cuprates were discovered by Bednorz and Muller [22] with critical temperatures above 100 K. These high-T_c compounds brought the field of unconventional superconductivity to a wider audience and are still the subject of extremely active research today. It was quickly understood that the physics of these unconventional superconductors was different, and that this time the correlations arising from the strong Coulomb repulsion between electrons was a crucial part of the problem [23]. This strong repulsion at short distance makes the s-wave channel, for which electrons are close to each other, highly unfavored, and hence can lead to pairing in higher angular momentum channels. In the case of overdoped cuprates, it is by now well established that the pairing occurs in the $d_{x^2-y^2}$-wave channel [24]. In this thesis, our working definition of unconventional superconductivity will be "non-s-wave"[1].

In this thesis, we will study an important example of such unconventional superconductors, Strontium Ruthenate (Sr_2RuO_4). Superconductivity was first discovered

[1]Strictly speaking, angular momentum is only well defined in a rotationally invariant system and thus not in the presence of a lattice. One should then instead use the different irreducible representations of the point group of the lattice. In a lattice setting, the definition of unconventional superconductor we will use is that the order parameter should vanish when summed over the Brillouin zone: $\sum_{\mathbf{k}} \Delta(\mathbf{k}) = 0$ [1]. This order parameter $\Delta(\mathbf{k})$ will be defined below.

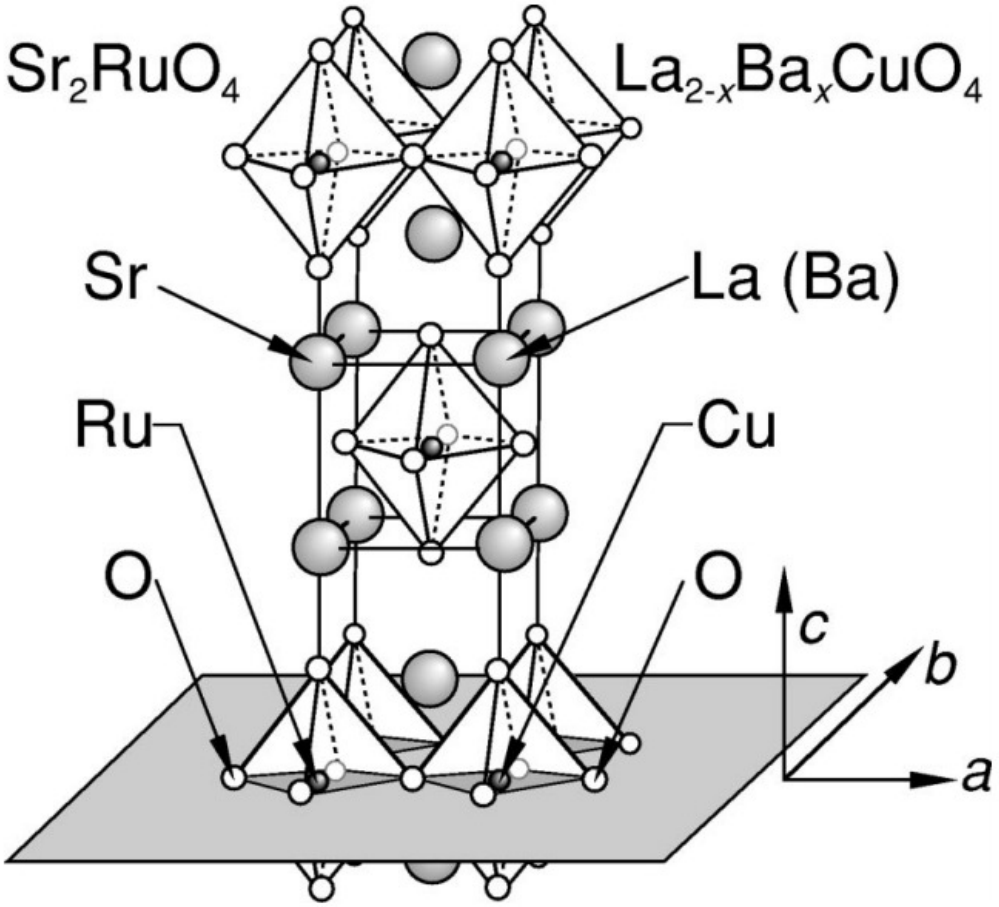

Figure 1.1: Layered perovskite structure of Sr_2RuO_4. Since it has the same structure as $La_{2-x}Ba_xCuO_4$, labels for both compounds are given. Reprinted figure with permission from Ref. [1]: [Andrew Peter Mackenzie and Yoshiteru Maeno, Rev. Mod. Phys., 75, 657-712, 2003]. Copyright 2016 by the American Physical Society.

in this material by Maeno *et al.* in 1994 [25]. Even though it has the same layered perovskite structure as Copper-based compounds, it was realized early on that its Physics was different, as the critical temperature of Sr_2RuO_4 (1.5 K) was 2 orders of magnitude smaller than for cuprates. Shortly after the discovery, it was proposed to be a *p*-wave superconductor by Rice and Sigrist [26]. This proposal was based on an analogy with superfluid ^{3}He for which the pairing was already established to be *p*-wave [27]. Since then, a lot of theoretical and experimental work has been done to try and understand the SC in this compound, but several important questions remain unanswered.

1.2 Motivation

We will give an overview of these questions in the next section, but first, we will lay out the reasons why reaching a convincing microscopic model of SC in Sr_2RuO_4 is extremely desirable: (1) it is one of the very few candidates for odd-parity superconductivity, (2) it is also a candidate for topological superconductivity, an example of a topological phase of matter, which have attracted an enormous amount of attention recently, (3) the normal state is a well-studied Fermi liquid, and samples are among the purest and cleanest of all known materials, making this compound an ideal testbed for microscopic theories of unconventional SC, (4) Sr_2RuO_4 is a prime example of a multi-band superconductor, which have been shown to lead to a variety of exotic effects and have been the subject of intense study, with the examples of MgB_2 [28] and the pnictides [29] being of particular interest.

We now detail each of these points separately.

1.2.1 Sr_2RuO_4 as an odd-parity superconductor

The parity of the angular momentum quantum number j is crucial for the physics of the superconductor. The Pauli exclusion principle states that the wave function of two fermions must be odd under the exchange of the two particles. For most known superconductors, j is even (which means that the orbital wave function is even under particle exchange) and thus the spin wave function must be odd. The only odd spin wave function of two spin 1/2 particles is one of spin zero, called a spin singlet.

One of the few exceptions is Strontium Ruthenate, for which strong experimental evidence points towards p-wave pairing ($j = 1$). The spin wave function must thus be even under particle exchange, which corresponds to a state of spin 1 called a spin triplet. The order parameter is in this case a three-dimensional vector $\vec{d}$, as opposed to a scalar for singlet states. The vectorial nature of the order parameter leads to a flurry of interesting effects, including for example half-quantum vortices (HQV) which are characterised by the relative winding of the phase of the spin-up and spin-down components of the Cooper pair wave function. These HQVs are expected to give rise to zero-energy Majorana quasi-particles, which have attracted a huge amount of

attention recently in relation with the possibility of topological quantum computation [30]. There is some evidence for the observation of these HQVs in mesoscopic samples of Sr_2RuO_4 [31].

1.2.2 Sr_2RuO_4 as a topological superconductor

As stated earlier, phases of matter are traditionally classified according to the symmetries they obey [32]. For example, a gas has a complete rotational spherical symmetry, while a solid breaks it down to, say, a cubic symmetry. Crucially, when it comes to fundamentally quantum particles, like electrons in a material, new phases can arise that have no classical counterpart and that cannot be distinguished by symmetry alone, but instead must be distinguished by some topological properties [33, 34]. Given the central role of symmetries in Physics, the very fact that some phases evade a classification based on symmetry alone could hardly be overestimated. One of the most important frontiers in condensed matter physics is to understand these novel topological phases, thereby making progress towards a more complete classification of what types of matter can exist.

For a given set of symmetries, equivalence classes for gapped phases can be defined by declaring two Hamiltonians to be topologically equivalent if there is a path in the space of symmetry-respecting Hamiltonians that connects the two Hamiltonians without closing the gap [35]. One can then associate one or several numbers to each equivalence class that can only change when the gap closes. These are called topological invariants of the phase. In the well-known case of the quantum Hall effect, this integer number would give the Hall conductance, in units of e^2/h [33]. There are also some gapless modes at the physical boundary between two states in different equivalence classes, and these modes are protected as long as the symmetry is respected and the bulk gap is not closed.

In the case of gapped phases of free fermions, a classification of topological phases was established called the periodic table of superconductors and insulators, or the ten-fold way[2, 36, 37]. The classification, shown in Figure 1.2, depends on the nature of three symmetries denoted TRS (time-reversal symmetry), PHS (particle-hole symmetry) and SLS (sublattice symmetry), and on the number of spatial dimensions

of the system. Time-reversal symmetry consists of reversing the direction of time, $t \to -t$. Particle-hole symmetry consists of exchanging electrons and holes (a hole is the absence of an electron), which is done by exchanging creation and annihilation operators. In the case of superconductors, this symmetry is always present and arises from a redundancy in the Bogolyubov-de Gennes theory (defined in Chapter 2). The sublattice symmetry is given by the product of TRS and PHS. For a given set of symmetries and a number of spatial dimensions, the table entry gives the number of topologically different phases (a dash corresponds to the trival case of only one phase).

Sr_2RuO_4 has attracted a lot of attention for potentially being a chiral $p_x + ip_y$ SC, which lies in the class D of this table. Since Sr_2RuO_4 is a layered material with very small inter-plane hopping, its Fermi surfaces have very small k_z dispersion (see Fig. 1.3), and it can be considered as a two-dimensional system to a good approximation. One therefore finds from the table that the classification of possible topological phases is given by an integer $C \in \mathbb{Z}$, which is given by the winding of the complex phase of the order parameter around the Fermi surface (which is equal to 1 in the $p_x + ip_y$ case in a rotationally invariant system). A chiral $p_x + ip_y$ superconductor has several striking properties [38]: (1) it spontaneously breaks time-reversal symmetry, (2) each of its Cooper pairs has an angular momentum of $\hbar$, leading to a macroscopic value for the total angular momentum: $N\hbar/2$, and (3) it has topologically protected gapless modes at edges and vortices. The edge states are exponentially localised within a coherence length close to the edge, and their dispersion with the momentum parallel to the edge $k_\parallel$ goes only in one direction due to their chirality. We should mention that the above classification was established for quadratic Hamiltonians, while a physical system is bound to have some interactions. The inclusion of interactions was shown to reduce the classification from $\mathbb{Z}$ to $\mathbb{Z}_{16}$ [39].

While the prevailing assumption so far has been the presence of a chiral SC state in Sr_2RuO_4, which lies in the class D of the ten-fold way, we will discuss in Chapter 3 the possibility of a different topological SC state called helical. These helical states lie in the class DIII, and are therefore classified by a $\mathbb{Z}_2$ invariant in two spatial dimensions: they can be either trivial or non-trivial. We will show that in a fairly

System	Cartan nomenclature	TRS	PHS	SLS	$d=1$	$d=2$	$d=3$
standard (Wigner-Dyson)	A (unitary)	0	0	0	-	$\mathbf{Z}$	-
	AI (orthogonal)	$+1$	0	0	-	-	-
	AII (symplectic)	-1	0	0	-	$\mathbf{Z}_2$	$\mathbf{Z}_2$
chiral (sublattice)	AIII (chiral unit.)	0	0	1	$\mathbf{Z}$	-	$\mathbf{Z}$
	BDI (chiral orthog.)	$+1$	$+1$	1	$\mathbf{Z}$	-	-
	CII (chiral sympl.)	-1	-1	1	$\mathbf{Z}$	-	$\mathbf{Z}_2$
BdG	D	0	$+1$	0	$\mathbf{Z}_2$	$\mathbf{Z}$	-
	C	0	-1	0	-	$\mathbf{Z}$	-
	DIII	-1	$+1$	1	$\mathbf{Z}_2$	$\mathbf{Z}_2$	$\mathbf{Z}$
	CI	$+1$	-1	1	-	-	$\mathbf{Z}$

Figure 1.2: Classification of gapped phases of free fermions. For each of the three symmetries TRS, PHS and SLS (defined in the text), a 0 means that the symmetry is absent, a ± 1 means that the symmetry is present and squares to ± 1. Reprinted figure with permission from Ref. [2]: [Andreas P. Schnyder, Shinsei Ryu, Akira Furusaki, and Andreas W. W. Ludwig, Phys. Rev. B 78, 195125, 2008]. Copyright 2016 by the American Physical Society.

large range of parameter space, our calculations predict a helical SC state. Note that half-quantum vortices can appear in both chiral and helical states.

1.2.3 Sr_2RuO_4 as a weakly coupled superconductor

Although Sr_2RuO_4 has the same crystal structure as the cuprate La_2BaCuO_4, it differs from cuprates in several ways. Since the relevant Ruthenium orbitals at the Fermi level are $4d$, instead of $3d$ for Copper, the interaction strength is comparatively smaller, and ruthenates are therefore closer to a regime of small interactions, for which perturbative theoretical techniques exist. Considering that Sr_2RuO_4 is a Fermi liquid above T_c, an itinerant picture, where superconductivity is understood as

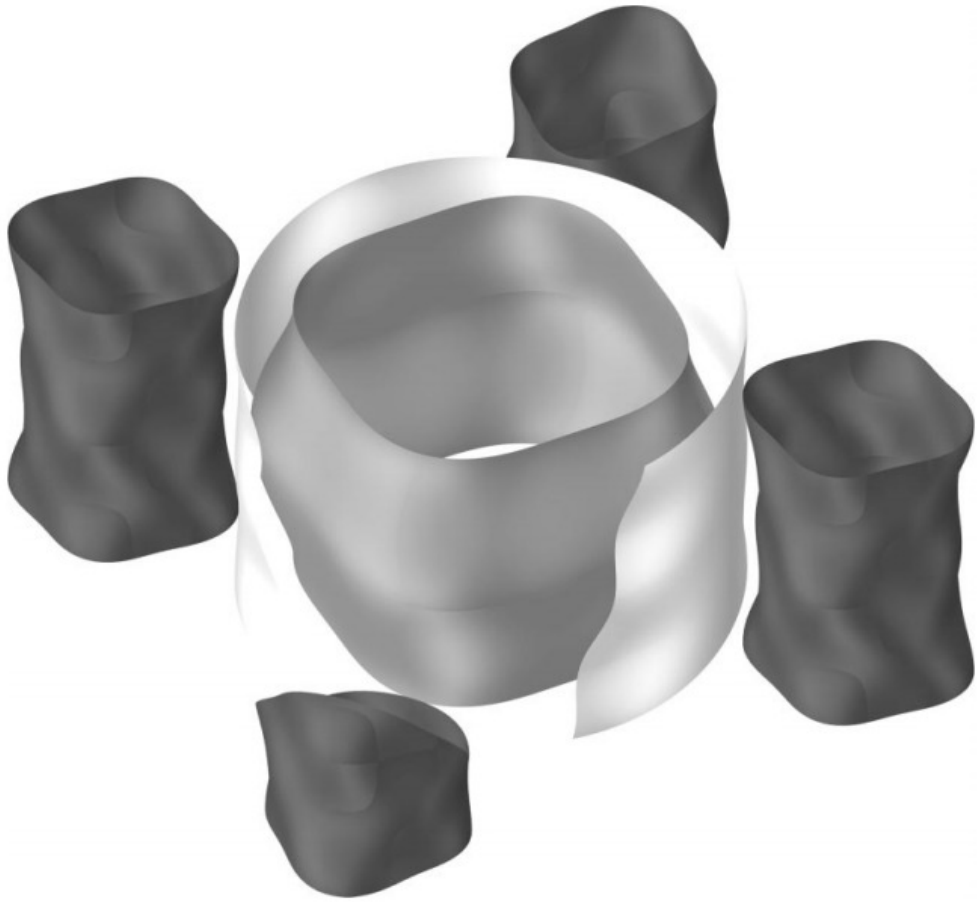

Figure 1.3: Cylindrical Fermi surfaces of Sr_2RuO_4. The ripples due to the out-of-plane dispersion have been exaggerated by a factor of 15. Reprinted figure with permission from Ref. [1]: [Andrew Peter Mackenzie and Yoshiteru Maeno, Rev. Mod. Phys., 75, 657-712, 2003]. Copyright 2016 by the American Physical Society.

the instability of itinerant electrons forming a Fermi liquid, is expected to be valid. Besides, since pure Sr_2RuO_4 is already superconducting, the theoretical complications of dealing with doping and the disorder that it creates is not present. The crystals of Sr_2RuO_4 are extremely free of disorder, and this enabled an extremely thorough knowledge of the Fermi surface (see Figure 1.3) and of the Fermi liquid parameters based on angle-resolved photo-emission spectroscopy (ARPES) and quantum oscillation measurements [1]. All in all, this makes Sr_2RuO_4 an ideal candidate for a convincing microscopic theory of unconventional superconductivity.

1.2.4 Sr_2RuO_4 as a multi-band superconductor

Sr_2RuO_4 has three bands crossing the Fermi level (called $\boldsymbol{\alpha}$, $\boldsymbol{\beta}$ and $\boldsymbol{\gamma}$ and shown in Figure 1.4), and each of them leads to a sizeable contribution to the density of states at the Fermi level. The $\boldsymbol{\gamma}$ band's main orbital contribution is the Ruthenium d_{xy} orbital, which leads to a fairly two-dimensional dispersion relation, and a cylindrical Fermi surface with a fairly circular section. In contrast, the $\boldsymbol{\alpha}$ and $\boldsymbol{\beta}$ bands arise from the relatively small hybridization of the Ruthenium d_{zx} and d_{yz} orbitals, which leads to a quasi-one-dimensional dispersion relation and Fermi surfaces with a section approximately given by a square (see Figure 1.3).

Given this difference, one might expect the superconductivity in these two sets of bands to be fairly decoupled. In this scenario, one of the sets of bands would be the driving force behind superconductivity and would have a large gap, while the other set of bands would only have a small gap induced by proximity effect. Instead, we will show in Chapter 3 that multi-band effects are crucial to understand superconductivity in Sr_2RuO_4.

Superconductivity in multi-band systems can lead to a flurry of exotic phenomena that are not present in a single band case. One example is the unusual behavior under magnetic field of type 1.5 superconductors[40], where different bands have different coherence lengths, some of which above and some of which below the magnetic penetration depth. Besides, as established in MgB_2 [28], the value of several thermodynamic quantities is changed compared to the usual BCS formula, like for example $\Delta(T = 0)/T_c$, the jump in specific heat at T_c, the critical field $H_{c,2}$,... Finally, the relative phase of the gap between different bands can fluctuate, leading to a possibly soft collective mode called the Leggett mode [41]. Strontium Ruthenate provides a great testbed for our understanding of all these effects.

1.3 Open questions about Sr_2RuO_4

The modern theoretical understanding of superconductivity is based on an order parameter, the gap $\Delta(\mathbf{k})$, which becomes non-zero in the superconducting phase [42].

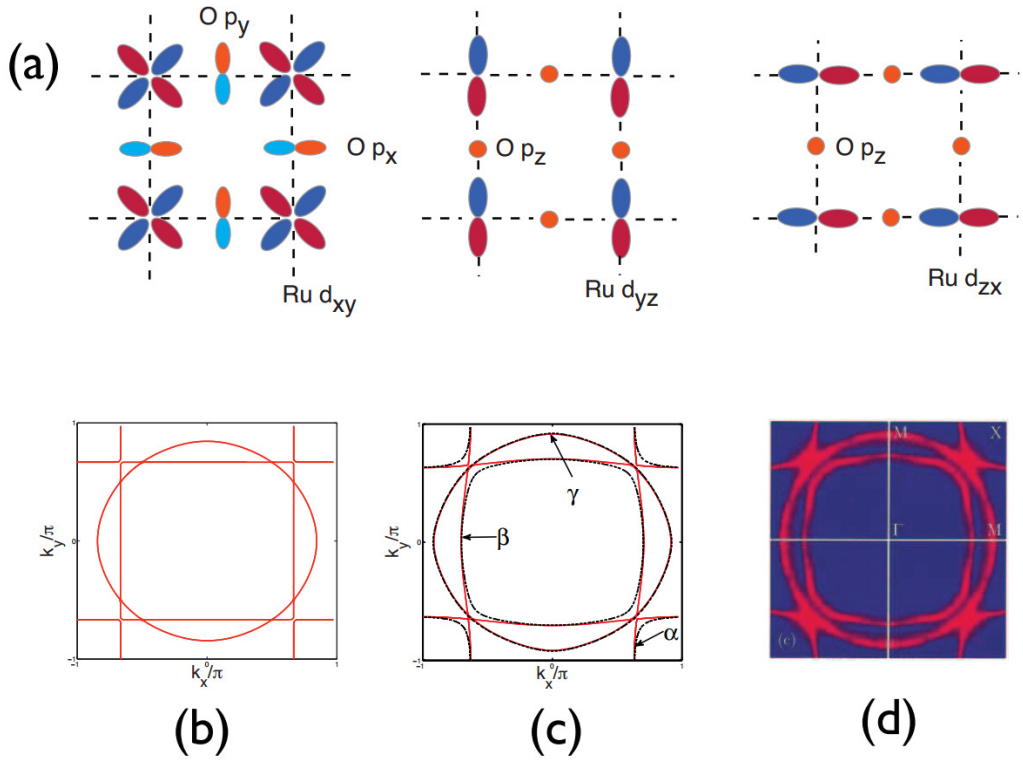

Figure 1.4: (a) The three Ruthenium orbitals which are relevant close to the Fermi level are depicted. They lie on a square lattice. The one on the left ($4d_{xy}$) is fairly isotropic in the plane, while the two on the right ($4d_{yz}$ and $4d_{zx}$) are quasi one-dimensional. The p orbitals of the ligand Oxygen atoms are also shown. (b) Fermi surfaces for the hypothetical bands which would be obtained by including only intra-orbital hopping in a tight-binding calculation, and by neglecting the small hopping along y (x) of the d_{zx} (d_{zy}) orbitals. (c) Fermi surfaces after the inclusion of inter-orbital hopping and spin-orbit coupling. (d) Experimental Fermi surfaces obtained by ARPES [3, 4]. Figure reproduced from Ref. [5] under the terms of the Creative Commons Attribution 3.0 licence.

This order parameter is a function of momentum $\mathbf{k}$, of the spin of the Cooper pair, and of the band[2]. Once this function is known, a large range of properties of the superconducting state can be calculated and compared with experiments. From a theoretical point of view, the Holy Grail would be to find an order parameter that fits all known experiments, and a microscopic theory that explains why this order parameter is favored.

Since the discovery in 1994, an extremely large number of experiments have been performed on the SC state of Sr_2RuO_4. Reviews are given in Refs. [1, 43, 44]. The possible order parameters are therefore highly constrained, and only a few candidates remain. Yet, as of now, no candidate fits all known experiments, and the identification of the order parameter in Sr_2RuO_4 is still an open question. Note that the identification of the order parameter is also a crucial way of checking if the microscopic mechanism assumed to favour it is the right one.

In this thesis, we will use a microscopic weak coupling calculation, introduced in details in Chapter 2, to address two open questions regarding the identification of the order parameter in Sr_2RuO_4. The first one concerns the anisotropy of the gap, both as a function of momentum, and as a function of the band considered. The second one concerns the dichotomy between the two different types of possible odd-parity order parameters, chiral and helical.

Note that there are some other open questions that will not be addressed in this thesis, especially regarding the behavior of superconductivity under magnetic field, and regarding the validity of strictly two-dimensional models. We will give a brief overview of these in the conclusion.

The layered structure of Sr_2RuO_4 translates into small overlaps between atomic orbitals along the c direction (see figure 1.1). Consequently, the inter-layer hoppings are much smaller than the intra-layer ones, and the Fermi surfaces are therefore cylinders with a very weak warping along the c direction (see figure 1.3). For this reason, this work will focus only on the in-plane dynamics of electrons. In the rest of this work, we will use interchangeably a, b, c and x, y, z for the corresponding directions shown in figure 1.1.

[2]We will give a precise definition of the gap in the next chapter, but we can already say that its magnitude $|\Delta(\mathbf{k})|$ gives the energy cost for breaking a Cooper pair.

1.3.1 Gap anisotropy

While conventional superconductors typically have highly isotropic gaps, this is not the case for unconventional superconductors. The momentum space non-uniformity of the gap of unconventional superconductors arises from their larger angular momentum pairing, since simple s-wave pairing is forbidden by the strong short-distance repulsion. For example, the d-wave pairing established in overdoped cuprates leads to a gap of the form $\Delta(\mathbf{k}) = \cos(k_x) - \cos(k_y)$ with nodes along the directions $\langle 110 \rangle$ and $\langle 1\bar{1}0 \rangle$. If $|\Delta(\mathbf{k})| \simeq 0$ for certain momenta on the Fermi surface, low-lying excitations exist at these momenta that dominate the thermodynamic behavior at low T, leading for example to a power law decay of the specific heat (instead of an exponential decay for a fully gapped state). For Sr_2RuO_4, based on the observed power law decay with temperature of several quantities, like specific heat[8], nuclear spin relaxation rate[45], heat conductivity [46, 47], acoustic attenuation[48], penetration depth [49], it was suggested early on that the SC state was not fully gapped. Since, in a tetragonal crystal, odd-parity order parameters do not have symmetry-imposed nodal lines crossing the Fermi surfaces, one should consider the possibility of accidental nodes, that are therefore dependent on the microscopic mechanism responsible for SC.

Another possibility is orbital-dependent superconductivity [50], whereby the gap is of different sizes on different bands. This possibility seems a priori natural for the case of Sr_2RuO_4, since it has bands of very different character. As mentioned before, Sr_2RuO_4 has three bands at the Fermi level : the $\boldsymbol{\gamma}$ band is mainly derived from the Ruthenium $4d_{xy}$ orbital, while the $\boldsymbol{\alpha}$ and $\boldsymbol{\beta}$ bands are mainly derived from the Ruthenium $4d_{xz}$ and $4d_{yz}$ orbitals (see figure 1.4). The $\boldsymbol{\gamma}$ band is fairly isotropic in the plane while the $\boldsymbol{\alpha}$ and $\boldsymbol{\beta}$ bands are quasi one-dimensional. As a result, the spin and density fluctuations, which are thought to be responsible for the effective attractive interaction (see Chapter 2), are of different nature depending on the band they arise from. The relevant quantity to consider in order to make that difference explicit is the particle-hole susceptibility $\chi(\mathbf{q})$. The momenta $\mathbf{Q}$ at which the susceptibility is maximal correspond to the momenta of the predominant fluctuations. In the case of

$\boldsymbol{\gamma}$, χ is peaked at small momenta ($\mathbf{Q} \simeq 0$), meaning that the driving force for SC would be ferromagnetic fluctuations in this case. Instead, for $\boldsymbol{\alpha}$ and $\boldsymbol{\beta}$, the nesting of the Fermi surfaces is such that χ is peaked at an incommensurate antiferromagnetic wavevector $\mathbf{Q_{AF}} \simeq (2k_F, 2k_F)$, where $k_F \simeq 2\pi/3$. This peak in the susceptibility was measured with neutrons [51].

As the two sets of bands have fundamentally different fluctuations, most of the theoretical work so far has been based on the assumption that one can treat them as decoupled systems. Based on this approach, several order parameters were predicted that are largely dominated by either $\boldsymbol{\gamma}$ [26, 52–55] or $\boldsymbol{\alpha}$ and $\boldsymbol{\beta}$ [56–63], but these gaps could not reproduce the observed specific heat evolution below T_c because it is incompatible with a too large difference between the gap on the active and passive bands [9].

Instead, Nomura and Yamada performed a spin-fluctuation-type calculation including the three bands [64]. They predicted a dominant nodeless gap on $\boldsymbol{\gamma}$ and a subdominant (approximately 3 times smaller) gap on $\boldsymbol{\alpha}$ and $\boldsymbol{\beta}$ with accidental near-nodes along $\langle 110 \rangle$ and $\langle 1\bar{1}0 \rangle$. This gap was shown to reproduce semi-quantitatively the behavior of the specific heat with T [64], and under in-plane magnetic fields [65, 66]. Yet, the debate was reopened when a scanning tunneling microscope (STM) [9] experiment gave evidence for the dominant gap to have a nodal behavior down to very low T, in disagreement with Nomura and Yamada's gap. A dominant near-nodal gap on $\boldsymbol{\alpha}$ and $\boldsymbol{\beta}$ and a subdominant (1.5 times smaller) nodeless gap on $\boldsymbol{\gamma}$ was then proposed based on phenomological arguments [9] and single-band weak coupling calculations [61].

We extended this weak-coupling calculation to incorporate all inter-band coupling effects, like spin-orbit coupling and Hund's coupling, and performed a three-band calculation without any bias towards a given set of bands. As explained in Chapter 3, depending on the chosen parameters, three regimes can be found. The first one corresponds to a scenario in which $\boldsymbol{\gamma}$ has a much larger SC gap than $\boldsymbol{\alpha}$ and $\boldsymbol{\beta}$ while the second one corresponds to the opposite case. Our calculations can thus reproduce earlier results obtained with the assumption of a dominant set of bands, be it $\boldsymbol{\gamma}$ or $\boldsymbol{\alpha}$ and $\boldsymbol{\beta}$. Crucially, a third regime appears over a finite region of parameter space

where highly anisotropic gaps of similar size appear on all three bands, and this is the regime we will be focusing on.

1.3.2 Chiral or helical

The second open question regarding Sr_2RuO_4 is related to the spin part of the Cooper pair wavefunction. As explained earlier, when two electrons form a pair, their state can be of total spin 0, i.e. a singlet, or of spin 1, i.e. a triplet. In the former case, the order parameter is given by $\Delta_s(\mathbf{k}) = \Delta_s(-\mathbf{k})$, and in the latter case by $\vec{d}(\mathbf{k}) = -\vec{d}(-\mathbf{k})$. The vector $\vec{d}(\mathbf{k})$, defined in Chapter 2, is such that, for a quantization axis chosen in its normal plane, the Cooper pair wavefunction is given by a linear combination of $|\uparrow\uparrow\rangle$ and $|\downarrow\downarrow\rangle$.

Evidence for odd-parity superconductivity comes from Josephson junction experiments, whereby the critical current was found to be a maximum for devices with junctions on the same side of the crystal and a minimum for devices with junctions on opposite sides[67]. The main piece of evidence in favour of a spin-triplet scenario for Sr_2RuO_4 is the absence of spin susceptibility decrease below T_c measured by Nuclear Magnetic Resonance (NMR) [68, 69] and polarized neutron scattering [70]. In the spin-singlet case, the paired electrons have zero spin and thus do not contribute to the paramagnetic response, which therefore shows a strong monotonic decrease with decreasing temperature below T_c. In the spin-triplet case, the spin susceptibility does not decrease for fields perpendicular to $\vec{d}$ [27]. The existing NMR data shows no susceptibility drop below T_c in Sr_2RuO_4 for magnetic fields in any direction (both in the *ab* plane and perpendicular to it).

In the absence of spin-orbit coupling (SOC), this would make perfect sense since the spin SU(2) symmetry would enable $\vec{d}(\mathbf{k})$ to rotate freely so as to remain perpendicular to any applied magnetic field. In fact, this vector has to belong to one of the irreducible representations of the crystal symmetry group, the tetragonal group D_{4h} (see Table 1.1). If the spin SU(2) symmetry was preserved, all these representations would be degenerate. The vector $\vec{d}(\mathbf{k})$ could then be equal to any linear combination of these and would therefore be able to rotate. Instead, based on ARPES [71, 72] and X-ray scattering [73] experiments, SOC was estimated to be comparatively large in

γ	$\vec{d}(\mathbf{k})$	Dimension	TRSB	Type	^{3}He phase
A_{1u}	$\hat{x}f_x + \hat{y}f_y$	1	No	Helical	BW
A_{2u}	$\hat{x}f_y - \hat{y}f_x$	1	No	Helical	
B_{1u}	$\hat{x}f_x - \hat{y}f_y$	1	No	Helical	
B_{2u}	$\hat{x}f_y + \hat{y}f_x$	1	No	Helical	
E_u	$\hat{z}(f_x \pm if_y)$	2	Yes	Chiral	ABM

Table 1.1: Odd-parity irreducible representations of D_{4h}, from Ref. [12]. TRSB stands for Time Reversal Symmetry Breaking. BW (ABM) stands for the Balian - Werthamer[13] (Anderson - Brinkman - Morel[14, 15]) phase of superfluid ^{3}He. Note that components odd under $k_z \to -k_z$ were not included in this table, as they would correspond to inter-plane components of the pairing, which are expected to be strongly disfavored due to the highly two-dimensional character of Sr_2RuO_4.

Sr_2RuO_4, with estimates ranging from 0.1 to 0.2 eV. This effect is expected to lock $\vec{d}$ in a preferred direction by lifting the degeneracy between the different irreducible representations and favoring one above the others, whose identification is the second open question we will try to address. Since NMR experiments show no susceptibility decrease below T_c for fields both in and out-of-plane, it was proposed that the pinning of $\vec{d}$ is small enough that even the smallest fields used in NMR experiments are enough to rotate it. This leaves two questions unanswered: Why would the pinning of $\vec{d}$ be so small, and what is the most favored $\vec{d}$ orientation at zero field?

The five different odd-parity irreducible representations of D_{4h} are given in Table 1.1. The unit vectors $\hat{x}$, $\hat{y}$, $\hat{z}$ are along the crystal directions a, b and c. The functions $f_{x,y}(\mathbf{k})$ are any functions that transform like $\sin(k_{x,y})$ under the tetragonal symmetry operations. The representations can be split into two groups. The first four, called helical, have $\vec{d}(\mathbf{k})$ in the ab plane and are achiral and time-reversal symmetric. They are two-dimensional counterparts of the BW (also called B) phase of superfluid ^{3}He [13]. In the aforementioned classification of fermionic topological phases, they would lie in class DIII[2] and are therefore classified by a $\mathbb{Z}_2$ invariant. The last one, called chiral, has $\vec{d}(\mathbf{k})$ perpendicular to the ab plane and breaks TRS. It is commonly referred to as the $p_x \pm ip_y$ state, although one should keep in mind that in a lattice setting this is merely the name of a representation. It is a two-dimensional counterpart of the ABM (also called A) phase of superfluid ^{3}He [14, 15, 26]. In the aforementioned classification of fermionic topological phases, it would lie in class D[2] and therefore has a $\mathbb{Z}$ classification characterised by the Chern number C.

It is interesting at this point to draw an analogy with the case of insulators[35] (see Figure 1.5). This analogy is based on the identical form taken by Bogoliubov-de Gennes (BdG) Hamiltonians (defined later) and insulator Hamiltonians. The chiral phases can be seen as the superconducting analogs of integer quantum Hall insulators, or Chern insulators in a lattice setting (class A in the classification of Ref. [2]). In both cases, time-reversal symmetry is broken, and chiral protected edge modes exist whose number and direction of propagation is given by the Chern number. One important difference is that the edge theory is the one of a (spinful) chiral Majorana fermion in the SC case, while it is the one of a Dirac fermion for an insulator. Another difference is that, in the case of the superconductor, time-reversal symmetry is broken spontaneously, and one should therefore expect the presence of domains of opposite chirality. The equilibrium state should have only one domain, with a chirality either positive or negative, because domain walls have a finite cost in energy. In practice, impurities and defects could pin domain walls and prevent them from moving around and forming a single domain. The chiral gapless modes should then be found not only at the edges, but also at domain walls.

The helical phases can be seen as the superconducting analogs of Quantum Spin Hall Effect phases, also known as two-dimensional topological insulators (class AII in Ref. [2])[35]. They can be seen as two copies of a chiral superconductor, one with positive chirality for, say, the $\uparrow\uparrow$ Cooper pairs, and one with negative chirality for the $\downarrow\downarrow$ ones. Since spin and chirality are reversed under time-reversal symmetry, this state is invariant under such a transformation. As a result, there are two counter-propagating gapless modes at the edges, one for each spin species (see Figure 1.5).

The prevailing assumption in the field has been that a chiral phase is favoured in Sr_2RuO_4. This assumption is based on several experiments. First, Muon Spin Relaxation (μSR) studies have shown an increase in relaxation rate below T_c that could be explained by the presence of spontaneous magnetic fields in the bulk generated by the chiral currents at the domain boundaries[74]. Second, a rotation of the polarisation plane of light reflected from a Sr_2RuO_4 surface was measured below T_c[75]. This magneto-optic Kerr effect (MOKE) is evidence for time-reversal symmetry breaking. Third, complicated diffraction patterns observed in superconducting quantum inter-

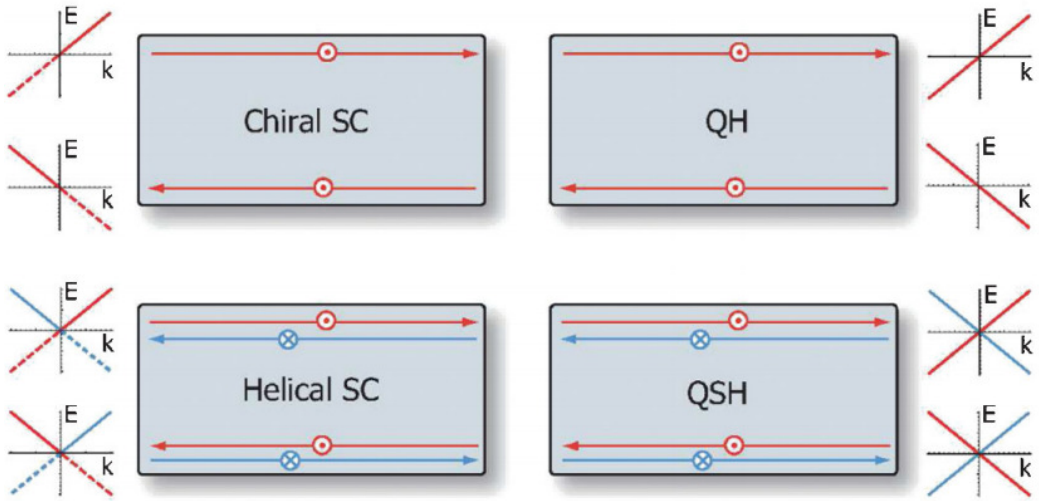

Figure 1.5: Schematic representation of chiral (top) and helical (bottom) edge states for superconductors (left) and quantum Hall phases (right). E stands for the energy of the Hamiltonian eigenstate localized at a given edge, and k for its momentum parallel to the edge. The circled dots and crosses signify the chirality of the edge mode, respectively positive and negative. In the helical case, red and blue correspond to the two different spin species. In the superconducting case, the line giving E is dashed for $E < 0$ to signify that the spectra for positive and negative E are actually redundant in a Bogolyubov - de Gennes calculation. Reprinted figure with permission from Ref. [6]: [Qi, Xiao-Liang and Hughes, Taylor L. and Raghu, S. and Zhang, Shou-Cheng, Phys. Rev. Lett. 102, 187001, 2009]. Copyright 2016 by the American Physical Society.

ference devices were interpreted in terms of domains of different chirality [67, 76, 77].

One should also mention that an in-plane tunneling spectroscopy experiment seems to indicate the presence of gapless edge states[78], but this result does not discriminate between chiral or helical edge states.

Vexingly, several experiments seem to be at odds with a chiral superconducting order parameter. First, the currents that would be expected at edges and domain walls have not been measured. Even though these currents would be screened in the bulk, it was predicted early on that they would still lead to relatively large magnetic fields (approximately 1 mT) close to sample edges [79]. No such magnetic field was measured yet, despite intense scrutiny [80, 81]. In Chapter 4, we will show that for the chiral order parameter predicted by our weak coupling calculation, a very large reduction of edge currents (up to 3 orders of magnitude) should be expected and potentially reconciles the presence of a chiral SC state with the absence of measurable edge currents[82].

Second, a recent experiment [10] measured the evolution of T_c under uniaxial strain and found no visible cusp at zero strain, while, based on symmetry alone, such a cusp is expected for a chiral state[83]. In Chapter 5, we will obtain an estimate of this cusp based on our microscopic calculation and we will show that it is typically too small to be resolved by experiments. Furthermore, we will show that, at larger uniaxial strain, the $\boldsymbol{\gamma}$ band goes through a van Hove singularity at which T_c is maximal, in agreement with a recent experiment[11].

Finally, another discrepancy arises when looking at the critical field $H_{c,2}$ for in-plane fields. The transition becomes first order at low T[84], and the value of $H_{c,2}$ is smaller than expected from anisotropic Ginzburg-Landau theory [85] and from the measured anisotropy of the vortex lattice [86]. These are typical characteristics of a Pauli-limited transition [42], where the depairing arises from Zeeman splitting instead of from the orbital motion of electrons under the magnetic field. The Pauli limited field is found by equating the superconducting condensation energy with the magnetization energy lost compared to the normal state, which is given by $\frac{1}{2}(\chi_n - \chi_s)H^2$, where $\chi_{n,s}$ is the spin susceptibility in the normal (resp. superconducting) state and H is the magnetic field. The issue is that, for an out-of-plane $\vec{d}$, the in-plane

spin susceptibility should not decrease below T_c, and hence there cannot be any Pauli limiting. Instead, a helical state with a $\vec{d}$ locked in-plane would exhibit a decrease in in-plane spin susceptibility, and therefore potentially Pauli limiting. Note that this would be in disagreement with the aforementioned NMR and spin-polarized neutrons experiments, which showed no spin susceptibility decrease.

An important remark is in order. In this introduction, spin has been discussed as if it were a good quantum number, while this is actually not the case in the presence of spin-orbit coupling. As explained in the next chapter, as long as time-reversal symmetry is preserved, it is always possible to define a pseudo-spin, and most of the discussion can be transposed to this setting by replacing spin by pseudo-spin. Yet, through the Zeeman effect, it is the physical spin, and not the pseudo-spin, that is coupled to magnetic fields, and one should always keep that in mind when studying the effect of Zeeman fields on superconductivity, for example in the context of Pauli limiting. The study of the impact of Zeeman fields on the pseudo-spin triplet SC states proposed in this thesis is important but left for future work.

In the light of all these, sometimes conflicting, experimental results, we carried out a microscopic calculation of the favored superconducting phase in Sr_2RuO_4 without including any bias towards a given SC order parameter symmetry. Using a weak coupling calculation, we calculated the critical temperatures of SC order parameters in all possible irreducible representations (including the even-parity ones). This model includes the different effects responsible for lifting the degeneracy between the different odd-parity order parameters: spin-orbit coupling, inter-orbital hopping and Hund's coupling. As explained in Chapter 4, we find that over most of parameter space, odd-parity OPs have a higher T_c than even-parity ones. Furthermore, we find a delicate balance between chiral and helical states, whereby, depending on the parameters, one or the other can be favored.

1.4 Outline

In Chapter 2, we present a weak-coupling calculation that enables us to find the most favoured superconducting order parameter in a generic multi-band, spin-orbit-coupled

system. In Chapter 3, we apply this weak coupling calculation to Sr_2RuO_4, and we use it to address the question of the gap anisotropy, and of the competition between chiral and helical states. In Chapter 4, we calculate the expected spontaneous edge currents for the chiral order parameter predicted in Chapter 3, and we discuss the implications for experiments. In Chapter 5, we calculate the evolution of T_c and of the different SC order parameters when the system is subject to uniaxial strain, again in relation with experiments. We finish with a conclusion.

2. Weak Coupling Theory

2.1 Introduction

It is widely believed that the main difference between conventional and unconventional superconductors is that correlations arising from the repulsion between electrons plays a key role in the latter case and is thought to, at least partially, replace phonons as the microscopic source for electron pairing. It might seem counterintuitive at first that a repulsive interaction between electrons could lead to the formation of Cooper pairs. The idea is that the electron-electron interaction can become effectively attractive due to various screening mechanisms, although the identification of this mechanism is still a matter of debate [87]. Since it was shown by BCS that even a vanishingly small attractive interaction between electrons close to the Fermi level is enough to trigger superconductivity [17], the crux of the problem is to find a microscopic mechanism which screens the bare repulsive interaction enough so that it becomes attractive in some channel. While the details differ, this electronic mechanism for superconductivity is always related to the screening of the bare interaction due to fluctuations of the Fermi liquid [88].

The first proposal for such an electronic mechanism for superconductivity was given by Kohn and Luttinger [89]. They computed the screened interaction perturbatively in the weak interaction limit for a homogeneous electron gas with short-range interactions. Since this problem has rotational invariance, the effective interaction can be decomposed in angular momentum channels. They then showed that, thanks to a singularity at momentum $2k_F$ (k_F is the Fermi momentum) in the second derivative of the Lindhard (or bare) particle-hole susceptibility (defined below) of the 3D free electron gas, regardless of the form of the interaction, there will always be at least one angular momentum channel in which the interaction is attractive. Cooper pairs will then form in that channel. The BCS instability is therefore inevitable for a uniform 3D electron gas with short-range interactions. Note that even though this is strictly

true, the critical temperature T_c can be extremely small since it scales like

$$\frac{T_c}{E_F} \sim e^{-(2l)^4} \tag{2.1}$$

where E_F is the Fermi energy and l is the total angular momentum quantum number ($l = 0$ for s-wave, $l = 1$ for p-wave, ...).

Since the screened interaction is computed perturbatively in the Kohn-Luttinger method, it is exact only in the vanishing interaction limit. It is possible to study superconductivity in this limit thanks to the fact that, unlike for other instabilities like charge and spin density waves, there is no threshold value of the interaction below which the Fermi liquid is stable: Even a vanishingly small interaction will drive superconductivity [89, 90]. Despite the fact that interactions are actually strong in realistic systems, this method was successfully applied to several unconventional superconductors, like cuprates, pnictides and organic superconductors (for a review, see Ref. [88]).

In essence, the calculation developed in this Chapter is a generalization of Kohn and Luttinger's work to the generic case of a multi-band, spin-orbit coupled superconductor on a lattice. The screened interaction will be calculated perturbatively in the weak interaction limit and will be expressed in terms of the bare particle-hole susceptibility, generalized to the multi-orbital case. Unlike in the homogeneous electron gas case, this susceptibility is not known analytically and has to be computed numerically. Furthermore, since lattice systems do not have rotational invariance, an important difference is that the different possible order parameters are classified according to the point group of the lattice instead of angular momentum.

Superconductivity can also be studied at finite interaction. Spin fluctuations can be greatly enhanced by interactions close to a magnetic transition. Within the random phase approximation [91], the bare particle-hole susceptibility $\chi_0^{\mathrm{ph}}(\mathbf{q})$ is renormalised to become

$$\chi_{\mathrm{RPA}}^{\mathrm{ph}}(\mathbf{q}) = \frac{\chi_0^{\mathrm{ph}}(\mathbf{q})}{1 - U\chi_0^{\mathrm{ph}}(\mathbf{q})} \tag{2.2}$$

where the Stoner criterion for magnetic instability is given by $U\chi_0^{\mathrm{ph}}(\mathbf{Q}) = 1$, where $\mathbf{Q}$ is the momentum at which χ_0^{ph} is maximal. Within a spin-fluctuation type theory,

the system sits close to the transition, $\chi_0^{\mathrm{ph}}(\mathbf{Q})U = 1 - \eta$, with $\eta \ll 1$ and $\chi_{\mathrm{RPA}}^{\mathrm{ph}}(\mathbf{q})$ therefore exhibits strong peaks at certain momenta. The symmetry of the order parameter depends crucially on the position of these maxima. Compared to weak coupling, these finite coupling theories have to deal with several complications. First, the spin fluctuations not only affect the effective interaction, but also single-fermion propagators. Second, one needs to deal with the dissipation of the spin fluctuations by the Fermi liquid through the decay into particle-hole pairs, also called Landau damping. Third, one needs to take into account the competition with magnetic order, since the system sits close to it by construction. Functional renormalisation group [92] calculations were developed to study the competition between these different order parameters. One should also mention spin-fermion models, where the soft spin fluctuations are introduced semi-phenomenologically [93].

In this chapter, we present a weak coupling theory of superconductivity in multi-orbital, spin-orbit coupled materials. In Section 2.2, we introduce the model Hamiltonian that will be used throughout this Chapter, the multi-orbital Hubbard model. In Section 2.3, we show how a spin-orbit coupled system can be understood in terms of pseudo-spin if it is time-reversal and parity invariant. We introduce a pseudo-spin $\vec{d}$ vector to describe a pseudo-spin triplet superconducting order parameter. In Section 2.4, we introduce the susceptibility in the Cooper channel as the quantity giving the response to a small field coupled to the superconducting order parameter. We then give the Feynman rules used to compute this susceptibility perturbatively. In Section 2.5, we show that this susceptibility satisfies the Bethe-Salpeter equation, and express the condition of its divergence in terms of the effective interaction. We introduce a pairing matrix whose eigenvalues give T_c and eigenmodes give the order parameter functional forms. In Section 2.6, we calculate the effective interaction in perturbation theory in the pseudo-spin singlet and triplet channels. In Section 2.7, we use a BCS mean-field Hamiltonian with the order parameters found previously to study the system below T_c. We finish with a conclusion.

2.2 Multi-orbital Hubbard model

Our starting point will be one of the most studied models for quantum materials, the multi-orbital Hubbard model[94, 95], whose Hamiltonian is

$$\begin{aligned} H = H_K + H_I = \sum_{\mathbf{k}} \sum_{a,a',s,s'} h_{a,s;a',s'}(\mathbf{k})\ c^\dagger_{\mathbf{k},a,s} c_{\mathbf{k},a',s'} \\ + \frac{1}{4} \sum_{\mathbf{k}_1+\mathbf{k}_2=\mathbf{k}_3+\mathbf{k}_4} \sum_{a_i,s_i} V_{a_1,s_1,a_2,s_2;a_3,s_3,a_4,s_4}\ c^\dagger_{\mathbf{k}_1,a_1,s_1} c^\dagger_{\mathbf{k}_2,a_2,s_2} c_{\mathbf{k}_3,a_3,s_3} c_{\mathbf{k}_4,a_4,s_4} \end{aligned} \tag{2.3}$$

where a is an index that runs over N_b different atomic orbitals in each unit cell, $s = \pm 1$ is the spin index and $\sum_{\mathbf{k}_1+\mathbf{k}_2=\mathbf{k}_3+\mathbf{k}_4}$ stands for a sum over $\mathbf{k}_1$, $\mathbf{k}_2$ and $\mathbf{k}_3$ over the full Brillouin zone, while $\mathbf{k}_4 = \mathbf{k}_1 + \mathbf{k}_2 - \mathbf{k}_3$. Many-electron states are generated by acting with creation operators $c^\dagger_{\mathbf{k},a,s}$ on the vacuum state $|\Omega\rangle$. These operators are the creation operators of plane wave states, $|\mathbf{k}, a, s\rangle = c^\dagger_{\mathbf{k},a,s} |\Omega\rangle$ with:

$$c^\dagger_{\mathbf{k},a,s} = \frac{1}{\sqrt{N}} \sum_{\mathbf{r}} e^{i\mathbf{k}\cdot\mathbf{r}} c^\dagger_{\mathbf{r},a,s} \tag{2.4}$$

where $\mathbf{r}$ are the sites of a given Bravais lattice and N is the total number of sites. We assume a Bravais lattice to simplify notations but it is not a restriction of the scheme. Creation and annihilation operators obey fermionic statistics:

$$\begin{aligned} \{c_i, c_j\} &= 0 \\ \{c^\dagger_i, c^\dagger_j\} &= 0 \\ \{c_i, c^\dagger_j\} &= \delta_{i,j} \end{aligned} \tag{2.5}$$

where $\{a, b\} = ab + ba$ and where i, j are generic indices and $\delta_{i,j}$ is the Kronecker delta.

H_K is the single-particle part of the Hamiltonian. It describes the hopping of electrons between different sites, the chemical potential, and the spin-orbit coupling. We are working in the grand-canonical ensemble, where the number of electrons is not fixed, and the expression given in Eq. 2.3 gives $H = \mathcal{H} - \mu N$, where $\mathcal{H}$ is strictly speaking the Hamiltonian, N is the total number of electrons and μ is the chemical potential. In this ensemble, at a temperature $T = \beta^{-1}$ (we take the Boltzmann

constant k_B to be 1), the expectation value of a given operator $\mathcal{O}$ is given by

$$\langle \mathcal{O} \rangle = \frac{\mathrm{Tr}[\mathcal{O} e^{-\beta H}]}{\mathrm{Tr}[e^{-\beta H}]} \tag{2.6}$$

For the sake of simplicity, in the following, we will always refer to H as the Hamiltonian, even though, strictly speaking, $\mathcal{H}$ is the Hamiltonian.

H_I describes the repulsion between electrons. Note that $V_{a_1,s_1,a_2,s_2;a_3,s_3,a_4,s_4}$ does not depend on momenta, as we will always consider on-site interactions in the following. Note also that for a given unordered set of indices $(\mathbf{k}_1, a_1, s_1; \mathbf{k}_2, a_2, s_2)$ for creation operators and $(\mathbf{k}_3, a_3, s_3; \mathbf{k}_4, a_4, s_4)$ for annihilation operators, there are always four terms in the sum for H_I that will match this set. The four different terms correspond to permutation of the indices between $\mathbf{k}_1, a_1, s_1$ and $\mathbf{k}_2, a_2, s_2$, and between $\mathbf{k}_3, a_3, s_3$ and $\mathbf{k}_4, a_4, s_4$. We choose a parametrization of the interaction such that these four terms are equal, which, given the anticommutation relation of fermionic operators, is ensured by imposing

$$\begin{aligned} V_{a_1,s_1,a_2,s_2;a_3,s_3,a_4,s_4} &= V_{a_2,s_2,a_1,s_1;a_4,s_4,a_3,s_3} \\ &= -V_{a_1,s_1,a_2,s_2;a_4,s_4,a_3,s_3} \\ &= -V_{a_2,s_2,a_1,s_1;a_3,s_3,a_4,s_4}. \end{aligned} \tag{2.7}$$

In the following, we will sometimes use t to refer to the energy scale of the hoppings and U to the energy scale of the interaction. We therefore have

$$\begin{aligned} h_{a,s;a',s'}(\mathbf{k}) &= t\ \tilde{h}_{a,s;a',s'}(\mathbf{k}) \\ V_{a_1,s_1,a_2,s_2;a_3,s_3,a_4,s_4} &= U\ \tilde{V}_{a_1,s_1,a_2,s_2;a_3,s_3,a_4,s_4} \end{aligned} \tag{2.8}$$

where $\tilde{h}_{a,s;a',s'}(\mathbf{k})$ and $\tilde{V}_{a_1,s_1,a_2,s_2;a_3,s_3,a_4,s_4}$ are dimensionless quantities defined such that the largest hopping amplitude in $\tilde{h}_{a,s;a',s'}(\mathbf{k})$ is 1 and such that the largest interaction matrix element in $\tilde{V}_{a_1,s_1,a_2,s_2;a_3,s_3,a_4,s_4}$ is 1.

While the discussion given in this Chapter is very general, we will often give the example of the single-orbital Hubbard model on a D-dimensional hypercubic lattice

for illustrative purposes. This model is given by

$$H = \sum_{\mathbf{k}} \xi(\mathbf{k}) \sum_{s} c^{\dagger}_{\mathbf{k},s} c_{\mathbf{k},s} + U \sum_{\mathbf{k}_1+\mathbf{k}_2=\mathbf{k}_3+\mathbf{k}_4} c^{\dagger}_{\mathbf{k}_1,\uparrow} c^{\dagger}_{\mathbf{k}_2,\downarrow} c_{\mathbf{k}_3,\downarrow} c_{\mathbf{k}_4,\uparrow} \tag{2.9}$$

It is easily checked that this corresponds to $V_{s_1,s_2;s_3,s_4} = U\delta_{s_1,-s_2}\delta_{s_3,-s_4}(\delta_{s_2,s_3} - \delta_{s_2,s_4})$ in the parametrization of Eq. 2.3. The single-particle energy ξ is obtained by diagonalizing the hoppings. For example, for nearest-neighbor hopping and $D = 2$ (square lattice), one has

$$H_K = -t \left(\sum_{\mathbf{r}} c^{\dagger}_{\mathbf{r}+\hat{x}} c_{\mathbf{r}} + c^{\dagger}_{\mathbf{r}+\hat{y}} c_{\mathbf{r}} + \text{h.c.} \right) - \mu \sum_{\mathbf{r}} c^{\dagger}_{\mathbf{r}} c_{\mathbf{r}} \tag{2.10}$$

where $\mathbf{r}$ runs over all sites, $\hat{x}$ and $\hat{y}$ are the unit vectors (the lattice constant is taken to be 1), t is the tunnelling amplitude and μ is the chemical potential. This leads to $\xi(\mathbf{k}) = -2t(\cos(k_x) + \cos(k_y)) - \mu$.

In this chapter, we start from the Hubbard Hamiltonian and present a weak coupling calculation of the superconducting instability arising in this model. In order to relate the so-obtained results to a given material, one should of course first establish the relevance of the Hubbard model to the material. This will be done in details in the next chapter for the case of Sr_2RuO_4, but we can already give a short justification. As a starting point to study a given material, one can use an Hartree-Fock type calculation to obtain a band structure that incorporates interactions between electrons at a mean-field level [94]. If this band structure happens to have conduction bands with a small bandwidth compared to the typical size of the effective interactions between electrons populating this band, the correlations arising from the interactions are expected to be too important to be neglected in a mean-field calculation. The Hubbard model is then used as an effective model where a tight-binding approximation is used to reproduce the narrow band and an on-site interaction is used to reproduce the effective interaction between electrons of this band. Compared to the bare Coulomb repulsion, this interaction is screened by the valence and conduction bands and therefore decays exponentially with distance. Typically, this screened interaction is sizeable only over a few lattice sites, and the approximation of keeping

only the on-site part of the interaction is then justified.

2.3 Pseudo-spin basis

We first diagonalize the single-particle Hamiltonian H_K. Without spin-orbit coupling, this Hamiltonian is diagonal in spin space, and each of the two spin species has the same hoppings, $h_{a,s;a',s'}(\mathbf{k}) = h_{a,a'}(\mathbf{k})\delta_{s,s'}$. After diagonalization, one obtains N_b doubly-degenerate bands, where the degeneracy comes from the spin degree of freedom, $H_K = \sum_{\mathbf{k},\alpha} \xi_\alpha(\mathbf{k})(c^\dagger_{\mathbf{k},\alpha,\uparrow}c_{\mathbf{k},\alpha,\uparrow} + c^\dagger_{\mathbf{k},\alpha,\downarrow}c_{\mathbf{k},\alpha,\downarrow})$, where α is the band index.

While the discussion so far has been fairly general, the impact of spin-orbit coupling can vary a lot depending on the materials. The type of systems considered in this thesis are such that the relevant dynamics happens in partially filled bands of the d orbitals of some transition metal element, like Copper ($3d$), Iron ($3d$), Ruthenium ($4d$), Iridium ($5d$),... In these compounds, the transition metal is typically surrounded by so-called ligand ions, like Oxygen in the case Sr_2RuO_4 or Selenium in the case of Iron Selenide, FeSe. In the perovskite structure of Sr_2RuO_4, the Oxygen ions form an octahedron around Ruthenium atoms (see Figure 1.1). Since we are only interested in the bands crossing the Fermi level, our tight-binding model will only include the atomic orbitals that have a sizeable contribution at the Fermi level, and the spin-orbit coupling will thus only be taken into account for these orbitals.

Starting from the idealized case of an isolated transition metal ion, two effects are to be taken into account: the effect of the ligand ions (i.e. the so-called crystal field), and spin-orbit coupling. The terms arising in the Hamiltonian from these two effects do not commute and one typically resorts to the following approximation: (1) diagonalize the largest of the two terms, (2) treat the second term in perturbation theory to split the remaining degeneracies. In this thesis, we will treat the case of a dominant crystal field, as it is the case relevant for Sr_2RuO_4. Note that the case of a dominant spin-orbit coupling is also of interest since it occurs for transition metals atoms with a $5d$ shell, like Iridium. Iridates were shown to exhibit a large range of interesting phases [96].

First, one should treat the effect of the ligand ions. This so-called crystal field

breaks rotational invariance down to the discrete symmetry group of the configuration of ligand ions. The crystal field generates a splitting between different atomic orbitals consistently with this reduced symmetry. In the case of Sr_2RuO_4, this crystal field splits the e_g doublet ($d_{x^2-y^2}$ and d_{z^2}) from the t_{2g} triplet (d_{xz}, d_{yz} and d_{xy}), and only the latter orbitals are relevant close to the Fermi level. The e_g orbitals point towards the vertices of the octahedra, i.e. the position of the Oxygen atoms, while the t_{2g} orbitals point towards the edges of the octahedra. The t_{2g} orbitals are therefore less hybridised with the Oxygen p orbitals.

Second, one should add the effect of the spin-orbit interaction. For an isolated atom with full rotational invariance, this term would be written as

$$H_{\mathrm{SOC}}^{\mathrm{atom}} = \eta \vec{L} \cdot \vec{S} \tag{2.11}$$

where η is the SOC constant which, within our formalism, is better kept as an adjustable phenomenological parameter, $\vec{L}$ is the orbital angular momentum and $\vec{S}$ is the spin angular momentum. In contrast, in the presence of a strong crystal field, the spin-orbit coupling is treated perturbatively and diagonalized within the subspace of the orbitals relevant close to the Fermi level. When the crystal field is the dominating effect, the most convenient basis of atomic orbitals is the one of real atomic orbitals, like d_{xz}, d_{yz} and d_{xy}, as opposed to L_z eigenvectors. In the following, we will use a as a generic index for these real orbitals used in the tight-binding Hamiltonian. Finally, summing over all atoms, the SOC term is inserted in the tight-binding model as

$$H_{\mathrm{SOC}} = \eta \sum_i P \vec{L}_i \cdot \vec{S}_i \; P \tag{2.12}$$

where i is the atom index and P is the projector to the subspace of real atomic orbitals relevant close to the Fermi level, which are indexed by $a = 1, \ldots, N_b$.

The single-particle Hamiltonian H_K can now be written as $H_K = H_{\mathrm{Hop}} + H_{\mathrm{SOC}}$ where H_{Hop} gives both intra- and inter-orbital hopping terms. While this Hamiltonian does not have a spin $SU(2)$ symmetry because of H_{SOC}, it still has time-reversal symmetry and parity. Thanks to these two symmetries, the bands are still doubly-degenerate, as we now show. A time-reversal symmetric system is a system that is

invariant under a transformation where the time t is replaced by $-t$. An inversion (or parity) symmetric system is a system that is invariant under a transformation where the spatial coordinates (x, y, z) are replaced by $(-x, -y, -z)$. More specifically, the time-reversal operator is defined as the anti-unitary operator $\mathcal{T} = T\mathcal{K}$, where $\mathcal{K}$ is the complex conjugation operator and T is given by

$$T\left|\mathbf{k}, a, s\right\rangle = s\left|-\mathbf{k}, a, -s\right\rangle. \tag{2.13}$$

The inversion operator is defined as

$$\mathcal{P}\left|\mathbf{k}, a, s\right\rangle = \left|-\mathbf{k}, a, s\right\rangle \tag{2.14}$$

where, in order to simplify notations, we have assumed that all a orbitals are even under parity, which is the case for the d orbitals we will be interested in. A system is time-reversal symmetric if its Hamiltonian satisfies $\mathcal{T}H\mathcal{T}^{-1} = H$ and inversion symmetric if $\mathcal{P}H\mathcal{P}^{-1} = H$. Say we have a single-particle eigenvector of H_K given by $\left|\mathbf{k}, \alpha\right\rangle = \sum_{a,s} u^{\alpha}_{a,s}\left|\mathbf{k}, a, s\right\rangle$. By time-reversal symmetry and inversion symmetry, we know that $\mathcal{PT}\left|\mathbf{k}, \alpha\right\rangle$ is is also an eigenvector with the same energy and the same momentum. It therefore only remains to show that these two states are not the same, which is easily shown by showing that their overlap vanishes: $\langle\mathbf{k}, \alpha|\mathcal{PT}|\mathbf{k}, \alpha\rangle = \sum_{a,s} u^{*}_{a,s}u^{*}_{a,-s}s = \sum_{a}(u^{*}_{a,\uparrow}u^{*}_{a,\downarrow} - u^{*}_{a,\downarrow}u^{*}_{a,\uparrow}) = 0$.

Since each band is doubly degenerate, it will be useful to define a pseudo-spin $\sigma = \pm 1$ to index these two degenerate states. After diagonalization, the Hamiltonian reads

$$H_K = \sum_{\alpha}\sum_{\mathbf{k}} \xi_{\mathbf{k},\alpha}(c^{\dagger}_{\mathbf{k},\alpha,\sigma=+1}c_{\mathbf{k},\alpha,\sigma=+1} + c^{\dagger}_{\mathbf{k},\alpha,\sigma=-1}c_{\mathbf{k},\alpha,\sigma=-1}). \tag{2.15}$$

with

$$c^{\dagger}_{\mathbf{k},\alpha,\sigma} = \sum_{a,s} u^{\alpha,\sigma}_{a,s}(\mathbf{k})c^{\dagger}_{\mathbf{k},a,s}. \tag{2.16}$$

We can now rewrite the entire Hamiltonian given in Eq. 2.3 in the band and pseudo-

spin basis:

$$H = H_K + H_I = \sum_{\alpha}\sum_{\mathbf{k}} \xi_{\mathbf{k},\alpha}(c^{\dagger}_{\mathbf{k},\alpha,\sigma=+1}c_{\mathbf{k},\alpha,\sigma=+1} + c^{\dagger}_{\mathbf{k},\alpha,\sigma=-1}c_{\mathbf{k},\alpha,\sigma=-1}) + \frac{1}{4}\sum_{\mathbf{k}_1+\mathbf{k}_2=\mathbf{k}_3+\mathbf{k}_4}\sum_{\alpha_i,\sigma_i} V_{\mathbf{k}_1,\alpha_1,\sigma_1,\mathbf{k}_2,\alpha_2,\sigma_2;\mathbf{k}_3,\alpha_3,\sigma_3,\mathbf{k}_4,\alpha_4,\sigma_4} c^{\dagger}_{\mathbf{k}_1,\alpha_1,\sigma_1}c^{\dagger}_{\mathbf{k}_2,\alpha_2,\sigma_2}c_{\mathbf{k}_3,\alpha_3,\sigma_3}c_{\mathbf{k}_4,\alpha_4,\sigma_4} \tag{2.17}$$

where

$$V_{\mathbf{k}_1,\alpha_1,\sigma_1,\mathbf{k}_2,\alpha_2,\sigma_2;\mathbf{k}_3,\alpha_3,\sigma_3,\mathbf{k}_4,\alpha_4,\sigma_4} = \sum_{a_i,s_i} V_{a_1,s_1,a_2,s_2;a_3,s_3,a_4,s_4}\; u^{\alpha_1,\sigma_1}_{a_1,s_1}(\mathbf{k}_1)\; u^{\alpha_2,\sigma_2}_{a_2,s_2}(\mathbf{k}_2)\; (u^{\alpha_3,\sigma_3}_{a_3,s_3}(\mathbf{k}_3))^*\; (u^{\alpha_4,\sigma_4}_{a_4,s_4}(\mathbf{k}_4))^* \tag{2.18}$$

From Eq. 2.7, it is easy to see that

$$\begin{aligned} V_{\mathbf{k}_1,\alpha_1,\sigma_1,\mathbf{k}_2,\alpha_2,\sigma_2;\mathbf{k}_3,\alpha_3,\sigma_3,\mathbf{k}_4,\alpha_4,\sigma_4} &= V_{\mathbf{k}_2,\alpha_2,\sigma_2,\mathbf{k}_1,\alpha_1,\sigma_1;\mathbf{k}_4,\alpha_4,\sigma_4,\mathbf{k}_3,\alpha_3,\sigma_3} \\ &= -V_{\mathbf{k}_2,\alpha_2,\sigma_2,\mathbf{k}_1,\alpha_1,\sigma_1;\mathbf{k}_3,\alpha_3,\sigma_3,\mathbf{k}_4,\alpha_4,\sigma_4} \\ &= -V_{\mathbf{k}_1,\alpha_1,\sigma_1,\mathbf{k}_2,\alpha_2,\sigma_2;\mathbf{k}_4,\alpha_4,\sigma_4,\mathbf{k}_3,\alpha_3,\sigma_3}. \end{aligned} \tag{2.19}$$

2.3.1 Pseudo-spin and crystal symmetries

One needs to choose a convention to decide which state is $\sigma = +1$ and which one is $\sigma = -1$, and this decision should be made at every $\mathbf{k}$ point. While this is purely a matter of convention, some choices are more advantageous if one wants to use similar tools and notations that exist in the case of $SU(2)$-invariant systems.

In analogy with the $SU(2)$-invariant case, it is advantageous to choose the pseudo-spin basis so that $T\,|\mathbf{k},\alpha,\sigma\rangle = \sigma\,|-\mathbf{k},\alpha,-\sigma\rangle$ and $\mathcal{P}\,|\mathbf{k},\alpha,\sigma\rangle = |-\mathbf{k},\alpha,\sigma\rangle$. Furthermore, besides $\mathcal{P}$, the point group of the crystal can also include discrete rotational symmetries. With the inclusion of spin-orbit coupling, these rotations should act simultaneously in real space and in spin space in order to commute with the Hamiltonian. For each element of the point group, one obtains an element of the so-called double group [12] by performing it in both real and spin space. A given element of the double group $\mathcal{R}$ acts in the following way:

$$\mathcal{R}\,|\mathbf{k},a,s\rangle = \mathcal{R}^O\mathcal{R}^S\,|\mathbf{k},a,s\rangle = R^O_{a,a'}R^S_{s,s'}\,|\mathcal{R}\mathbf{k},a',s'\rangle \tag{2.20}$$

where $R^O_{a,a'}$ is the rotation matrix in the space of atomic orbitals, $R^S_{s,s'}$ is the rotation matrix in spin space, $\mathcal{R}\mathbf{k}$ is the image of the vector $\mathbf{k}$ under the rotation $\mathcal{R}$ and where the summation over repeated indices is implied. If $\mathcal{R}$ is a rotation of angle θ and axis $\hat{n}$, one has $\mathcal{R}^O = e^{-i\theta\hat{n}\cdot\vec{L}}$ and $\mathcal{R}^S = e^{-i\theta\hat{n}\cdot\vec{S}}$ ($\hbar$ is set to one everywhere in this thesis). From Eq. 2.14, we find that for the parity transformation, i.e. $\mathcal{R} = \mathcal{P}$, one has $\mathcal{R}^O = \mathbb{1}$, $\mathcal{R}^S = \mathbb{1}$ and of course $\mathcal{R}\mathbf{k} = -\mathbf{k}$.

In analogy with the case without spin-orbit coupling, it is advantageous to choose the pseudo-spin basis so that the following relation holds:

$$\mathcal{R}\left|\mathbf{k},\alpha,\sigma\right\rangle = R^S_{\sigma,\sigma'}\left|\mathcal{R}\mathbf{k},\alpha,\sigma'\right\rangle. \tag{2.21}$$

In this way, under discrete rotations of the double group, each band behaves as if it were a single (s-wave) orbital, and the pseudo-spin behaves in the same way as a regular spin would. The advantage of this basis choice is that the pseudo-spin triplet superconducting order parameter $\vec{d}$ will transform like a vector under the double group, and the pseudo-spin singlet order parameter will transform like a scalar. This will be explained in the next Section.

One simple way to achieve this is to proceed as follows. First, for each $\mathbf{k}$ in the irreducible Brillouin zone (the smallest subset of the BZ such that any $\mathbf{k}$ can be folded back to it by an element of the point group) and for each band α, pick an arbitrary eigenvector and assign it the value of $\sigma = +1$, i.e. declare it to be $\left|\mathbf{k},\alpha,\sigma=+1\right\rangle$. Once this is done, $\left|\mathbf{k},\alpha,\sigma=-1\right\rangle$ is defined up to a phase, which we fix by posing $\left|\mathbf{k},\alpha,\sigma=-1\right\rangle \equiv \mathcal{T}\mathcal{P}\left|\mathbf{k},\alpha,\sigma=+1\right\rangle$. Second, for every $\mathbf{k}$ point outside the irreducible BZ, define the basis as

$$\left|\mathbf{k},\alpha,\sigma\right\rangle = \left(\left(R^S\right)^{-1}\right)_{\sigma,\sigma'}\mathcal{R}\left|\mathcal{R}^{-1}\mathbf{k},\alpha,\sigma'\right\rangle \tag{2.22}$$

where $\mathcal{R}^{-1}\mathbf{k}$ is in the irreducible BZ.

Note that, due to the double covering of $SO(3)$ by $SU(2)$, elements of the double group that correspond to 2π rotations have $R^S = -\mathbb{1}$ and are therefore not the identity element. The solutions for finding $\mathcal{R}$ such that $\mathcal{R}^{-1}\mathbf{k}$ is in the irreducible BZ are therefore only obtained modulo these 2π rotations. This simply leads to

a sign ambiguity in the above scheme, which can be easily fixed by restricting $\mathcal{R}$ in Eq. 2.22 to rotations of angles in the range $[0, 2\pi[$. This arbitrary choice of sign will be inconsequential in the following, since we will only be interested in the transformation of Cooper pair operators, for which two electrons are transformed at the same time and the -1 factors would therefore cancel.

2.3.2 Superconducting order parameter in pseudo-spin basis

In the next section, we will introduce the superconducting order parameter as the non-zero expectation value of Cooper pair operators of the form

$$\phi_{\sigma,\sigma'}(\mathbf{k}, \alpha) \equiv c_{\mathbf{k},\alpha,\sigma} c_{-\mathbf{k},\alpha,\sigma'} \tag{2.23}$$

In the single orbital $SU(2)$-invariant case, Balian and Werthamer [13] introduced the following parametrization of the spin degrees of freedom of the Cooper pair:

$$\begin{pmatrix} \phi_{\uparrow\uparrow}(\mathbf{k}) & \phi_{\uparrow\downarrow}(\mathbf{k}) \\ \phi_{\downarrow\uparrow}(\mathbf{k}) & \phi_{\downarrow\downarrow}(\mathbf{k}) \end{pmatrix} = \frac{1}{\sqrt{2}} \begin{pmatrix} -\phi_{d_x}(\mathbf{k}) + i\phi_{d_y}(\mathbf{k}) & \phi_{d_z}(\mathbf{k}) + \phi_{d_0}(\mathbf{k}) \\ \phi_{d_z}(\mathbf{k}) - \phi_{d_0}(\mathbf{k}) & \phi_{d_x}(\mathbf{k}) + i\phi_{d_y}(\mathbf{k}) \end{pmatrix}, \tag{2.24}$$

where $\phi_{ss'}(\mathbf{k}) = c_{\mathbf{k},s} c_{-\mathbf{k},s'}$. This parametrization is advantageous because the spin singlet (resp. triplet) order parameter ϕ_{d_0} (resp. $\phi_{\vec{d}}$) is a scalar (resp. vector) under any spin-space rotation $\mathcal{R}^S$:

$$\begin{aligned} \mathcal{R}^S \phi_{d_0}(\mathbf{k}) (\mathcal{R}^S)^{-1} &= \phi_{d_0}(\mathbf{k}) \\ \mathcal{R}^S \phi_{\vec{d}}(\mathbf{k}) (\mathcal{R}^S)^{-1} &= \phi_{\mathcal{R}\vec{d}}(\mathbf{k}). \end{aligned} \tag{2.25}$$

In analogy with the $SU(2)$-invariant case, we rearrange the pseudo-spin degrees of freedom in a singlet ϕ_{d_0} and a triplet $\phi_{\vec{d}}$:

$$\begin{pmatrix} \phi_{++} & \phi_{+-} \\ \phi_{-+} & \phi_{--} \end{pmatrix} = \frac{1}{\sqrt{2}} \begin{pmatrix} -\phi_{d_x} + i\phi_{d_y} & \phi_{d_z} + \phi_{d_0} \\ \phi_{d_z} - \phi_{d_0} & \phi_{d_x} + i\phi_{d_y} \end{pmatrix}, \tag{2.26}$$

where we have left the indices $\mathbf{k}, \alpha$ implicit. Now, using the property of the pseudo-spin basis given in Eq. 2.21, one can check that the pseudo-spin order parameters

behave in the appropriate way under any element of the double group $\mathcal{R}$:

$$\begin{aligned} \mathcal{R}\phi_{d_0}(\mathbf{k},\alpha)\mathcal{R}^{-1} &= \phi_{d_0}(\mathcal{R}\mathbf{k},\alpha) \\ \mathcal{R}\phi_{\vec{d}}(\mathbf{k},\alpha)\mathcal{R}^{-1} &= \phi_{\mathcal{R}\vec{d}}(\mathcal{R}\mathbf{k},\alpha) \end{aligned} \tag{2.27}$$

This means that, when classifying the different possible pseudo-spin order parameters, we can use the irreducible representations of the point group.

2.4 Linear response

In order to study the onset of superconductivity, let us compute the susceptibility of the system to the appearance of a superconducting order parameter within linear response theory. The divergence of this quantity will mark the onset of superconductivity. The order parameter is given by the non-zero expectation value of the Cooper pair creation operator $\phi^\dagger_{\mathbf{k},\alpha,\sigma,\sigma'} \equiv c^\dagger_{\mathbf{k},\alpha,\sigma} c^\dagger_{-\mathbf{k},\alpha,\sigma'}$.

In general, one should consider the possibility of other order parameters, including Cooper pairing at finite momentum and frequencies, and spin-density wave (SDW) or charge-density wave (CDW) order. Instead, in the weak coupling limit, it was shown (see for example Ref. [90]) that, except for a few exceptions that will be discussed below, the only instability is the zero-frequency, zero-momentum Cooper pairing and it is therefore sufficient to consider only this order parameter. Note that we only considered pairing between electrons of the same band. This is justified if the superconducting gap scale is much smaller than the energy separation between the different bands close to the Fermi level, which is generically true in the $U/t \to 0$ limit.

A non-zero expectation value of ϕ breaks the $U(1)$ symmetry $c_{\mathbf{k},\alpha,\sigma,\sigma'} \to c_{\mathbf{k},\alpha,\sigma,\sigma'} e^{i\theta}$ associated with the conservation of the total number (or charge) of electrons. As such, if we naively compute a thermal expectation value of the type $\mathrm{Tr}[e^{-\beta H}\phi_{\mathbf{k},\alpha,\sigma,\sigma'}]/\,\mathrm{Tr}[e^{-\beta H}]$, it would always be zero by symmetry. Instead, one can imagine applying a vanishingly small field coupled to the superconducting order parameter, calculate the thermal average with that small field, and then take the field to zero at the end. With this small

perturbation, the Hamiltonian becomes $H + H_J$ with

$$H_J = \sum_{\mathbf{k}} J_{\mathbf{k},\alpha,\sigma,\sigma'} \phi_{\mathbf{k},\alpha,\sigma,\sigma'} + h.c. \tag{2.28}$$

where $J_{\mathbf{k},\alpha,\sigma,\sigma'}$ is some arbitrary complex function much smaller than the energy scale set by H. As a reminder, $H = H_K + H_I$ is the unperturbed Hamiltonian and was given previously. We want to compute the expectation value of ϕ for the perturbed system:

$$\langle \phi_{\mathbf{k},\alpha,\sigma,\sigma'} \rangle = \frac{\mathrm{Tr}[e^{-\beta(H+H_J)} \phi_{\mathbf{k},\alpha,\sigma,\sigma'}]}{\mathrm{Tr}[e^{-\beta(H+H_J)}]} \tag{2.29}$$

2.4.1 Field theory formalism

It is now advantageous to use the coherent state fermionic field theory derived from the Hamiltonian $H + H_J$ [90]:

$$\begin{aligned} S + S_J &= S_K + S_I + S_J \\ &= \frac{1}{\beta} \sum_{\mathbf{k},\omega,\alpha,\sigma} (i\omega - \xi_{\mathbf{k},\alpha}) \overline{\Psi}_{\mathbf{k},\omega,\alpha,\sigma} \Psi_{\mathbf{k},\omega,\alpha,\sigma} \\ &- \frac{1}{4} \frac{1}{\beta^3} \sum_{\mathbf{k}_i,\omega_i,\alpha_i,\sigma_i} V_{\mathbf{k}_1,\alpha_1,\sigma_1,\mathbf{k}_2,\alpha_2,\sigma_2;\mathbf{k}_3,\alpha_3,\sigma_3,\mathbf{k}_4,\alpha_4,\sigma_4} \overline{\Psi}_{\mathbf{k}_1,\omega_1,\alpha_1,\sigma_1} \overline{\Psi}_{\mathbf{k}_2,\omega_2,\alpha_2,\sigma_2} \Psi_{\mathbf{k}_3,\omega_3,\alpha_3,\sigma_3} \Psi_{\mathbf{k}_4,\omega_4,\alpha_4,\sigma_4} \\ &- \frac{1}{\beta} \sum_{\mathbf{k},\omega,\alpha,\sigma,\sigma'} J_{\mathbf{k},\alpha,\sigma,\sigma'} \Psi_{-\mathbf{k},-\omega,\alpha,\sigma'} \Psi_{\mathbf{k},\omega,\alpha,\sigma} + (J_{\mathbf{k},\alpha,\sigma,\sigma'})^* \overline{\Psi}_{\mathbf{k},\omega,\alpha,\sigma} \overline{\Psi}_{-\mathbf{k},-\omega,\alpha,\sigma'} \end{aligned} \tag{2.30}$$

where $\Psi_{\mathbf{k},\omega,\alpha,\sigma}$ is a Grassman number and has the dimension of the inverse of an energy, the sum over ω_i is such that $\omega_1 + \omega_2 = \omega_3 + \omega_4$ and the sum over $\mathbf{k}_i$ is such that $\mathbf{k}_1 + \mathbf{k}_2 = \mathbf{k}_3 + \mathbf{k}_4$ modulo a reciprocal lattice vector. Grassman numbers anticommute with each other, commute with regular numbers, and square to zero [90]. The Matsubara frequencies that are summed over are given by $\omega = \frac{(2n+1)\pi}{\beta}$, with n any integer. In the zero-temperature limit, $\frac{1}{\beta}\sum_\omega \to \int_{-\infty}^{\infty} \frac{d\omega}{2\pi}$. In the thermodynamic limit, $\sum_{\mathbf{k}} \to \int \frac{d\mathbf{k}}{(2\pi)^D}$ where the integral is over the Brillouin zone and D is the number of spatial dimensions.

For a given operator $\mathcal{O}$, one defines its evolution in imaginary time τ by $\mathcal{O}_\tau = e^{(H+H_J)\tau} \mathcal{O} e^{-(H+H_J)\tau}$. If $\mathcal{O}_\tau$ is expressed in terms of c_τ and $c_\tau^\dagger$ in a normal-ordered

way (i.e. with each creation operator to the left of its annihilation operator), its expectation value is obtained in the field theory formalism by replacing each c ($c^\dagger$) by the corresponding Grassman number Ψ ($\overline{\Psi}$). Within this formalism, we can now compute the expectation value given earlier:

$$\begin{aligned}\langle \phi_{\mathbf{k},\alpha,\sigma,\sigma'} \rangle &= \langle \Psi_{-\mathbf{k},\tau=0,\alpha,\sigma'} \Psi_{\mathbf{k},\tau=0,\alpha,\sigma} \rangle_{S+S_J} \\ &= Z^{-1} \int D(\overline{\Psi},\Psi)\ e^{S+S_J}\ \Psi_{-\mathbf{k},\tau=0,\alpha,\sigma'} \Psi_{\mathbf{k},\tau=0,\alpha,\sigma}\end{aligned} \tag{2.31}$$

with $Z = \int D(\overline{\Psi},\Psi)\ e^{S+S_J}$. We now use the fact that the perturbation H_J is small to write $e^{S_J} \simeq 1 + S_J$, leading to

$$\left\langle \phi_{\mathbf{k}_1,\alpha_1,\sigma_1,\sigma_1'} \right\rangle \simeq -\frac{1}{\beta} \sum_{\mathbf{k}_2,\omega_2,\alpha_2,\sigma_2,\sigma_2'} (J_{\mathbf{k}_2,\alpha_2,\sigma_2,\sigma_2'})^* \left\langle \overline{\Psi}_{\mathbf{k}_2,\omega_2,\alpha_2,\sigma_2} \overline{\Psi}_{-\mathbf{k}_2,-\omega_2,\alpha_2,\sigma_2'} \Psi_{-\mathbf{k}_1,\tau=0,\alpha_1,\sigma_1'} \Psi_{\mathbf{k}_1,\tau=0,\alpha_1,\sigma_1} \right\rangle_S . \tag{2.32}$$

Using

$$\begin{aligned}\Psi_\tau &= \frac{1}{\beta} \sum_\omega e^{-i\omega\tau} \Psi_\omega \\ \overline{\Psi}_\tau &= \frac{1}{\beta} \sum_\omega e^{i\omega\tau} \overline{\Psi}_\omega,\end{aligned} \tag{2.33}$$

we can now Fourier transform the two last Grassman variables, leading to

$$\begin{aligned}\left\langle \phi_{\mathbf{k}_1,\alpha_1,\sigma_1,\sigma_1'} \right\rangle &= -\frac{1}{\beta^3} \sum_{\mathbf{k}_2,\omega_1,\omega_2,\alpha_2,\sigma_2,\sigma_2'} \chi^{\mathrm{SC}}_{\mathbf{k}_1,\omega_1,\alpha_1,\sigma_1,\sigma_1';\mathbf{k}_2,\omega_2,\alpha_2,\sigma_2,\sigma_2'} (J_{\mathbf{k}_2,\alpha_2,\sigma_2,\sigma_2'})^* \\ \chi^{\mathrm{SC}}_{\mathbf{k}_1,\omega_1,\alpha_1,\sigma_1,\sigma_1';\mathbf{k}_2,\omega_2,\alpha_2,\sigma_2,\sigma_2'} &= \left\langle \overline{\Psi}_{\mathbf{k}_2,\omega_2,\alpha_2,\sigma_2} \overline{\Psi}_{-\mathbf{k}_2,-\omega_2,\alpha_2,\sigma_2'} \Psi_{-\mathbf{k}_1,-\omega_1,\alpha_1,\sigma_1'} \Psi_{\mathbf{k}_1,\omega_1,\alpha_1,\sigma_1} \right\rangle_S .\end{aligned} \tag{2.34}$$

χ^{SC} is the susceptibility in the Cooper channel, and will be shown to diverge in the thermodynamic limit at a critical temperature T_c. In order to evaluate χ^{SC}, we use a perturbation expansion in the interaction S_I, and we are left with having to evaluate only expectation values with respect to S_K, which can be done by using Wick's theorem since S_K is quadratic. This perturbation theory is best described in terms of Feynman diagrams [97].

The Feynman rules to compute a fermionic correlator are the following. Solid lines are free electron propagators $G_0(\mathbf{k},\omega,\alpha,\sigma) = (i\omega - \xi_{\mathbf{k},\alpha})^{-1}$. For each fermionic

operator $\Psi_{\mathbf{k},\omega,\alpha,\sigma}$ ($\overline{\Psi}_{\mathbf{k},\omega,\alpha,\sigma}$) in the correlator, there is an external leg entering (resp. exiting) the diagram with the same indices $\mathbf{k}, \omega, \alpha, \sigma$. For a given set of external legs, one should sum over all diagrams that connect these external legs. One should not sum over diagrams that include disconnected components that are not linked to the external legs, as these diagrams are cancelled by the denominator in the definition of the expectation value.

A vertex is the association of two incoming and two outgoing fermionic propagators linked by a dashed line, as shown in Fig. 2.4. Momenta and Matsubara frequencies are conserved at each vertex. Thanks to this property, for a given diagram, all sums over internal momenta can be performed readily, except for n_{loop} of them, where n_{loop} is the number of loops in the diagram. Each connected component of the diagram has an overall factor given by $\beta\delta_{\sum_i \omega_i}\delta_{\sum_i \mathbf{k}_i}$, where $\omega_i, \mathbf{k}_i$ are the external frequencies and momenta of that connected component. For each internal propagator, one should sum over its α, σ indices. For each fermionic loop, the diagram picks up a minus sign. A fermionic loop is a loop formed by electron propagators.

The factor of $\frac{1}{4} = \frac{1}{2!2!}$ in the action in front of $-V_{\mathbf{k}_1,\alpha_1,\sigma_1,\mathbf{k}_2,\alpha_2,\sigma_2;\mathbf{k}_3,\alpha_3,\sigma_3,\mathbf{k}_4,\alpha_4,\sigma_4}$ (abbreviated as $-V_{1,2;3,4}$ in the following) takes care of the 4 possible leg permutations of a given vertex ($1 \leftrightarrow 2$ and $3 \leftrightarrow 4$), which all give the same contribution. Two diagrams that only differ by such a permutation are called equivalent. One can therefore sum only over one example diagram in each equivalence class and use a factor of $-V_{1,2;3,4}$ for each vertex. This is correct as long as there are 4^v diagrams in each equivalence class, where v is the number of vertices. In certain equivalence classes, two or more of their fermionic legs can be permuted without changing the diagram. In that case, the number of diagrams is therefore smaller, say $4^v/m$. One should then divide the contribution from this equivalence class by m, which is called the symmetry factor [97].

We are only interested in the divergent part of χ^{SC}, which will arise from the

connected part of the expectation value, defined by

$$\begin{aligned}\chi^{\mathrm{SC},c}_{\mathbf{k}_1,\omega_1,\alpha_1,\sigma_1,\sigma_1';\mathbf{k}_2,\omega_2,\alpha_2,\sigma_2,\sigma_2'} &= \left\langle \overline{\Psi}_{\mathbf{k}_2,\omega_2,\alpha_2,\sigma_2}\overline{\Psi}_{-\mathbf{k}_2,-\omega_2,\alpha_2,\sigma_2'}\Psi_{-\mathbf{k}_1,-\omega_1,\alpha_1,\sigma_1'}\Psi_{\mathbf{k}_1,\omega_1,\alpha_1,\sigma_1}\right\rangle_S \\ &- \left\langle \overline{\Psi}_{-\mathbf{k}_2,-\omega_2,\alpha_2,\sigma_2'}\Psi_{-\mathbf{k}_1,-\omega_1,\alpha_1,\sigma_1'}\right\rangle_S \left\langle \overline{\Psi}_{\mathbf{k}_2,\omega_2,\alpha_2,\sigma_2}\Psi_{\mathbf{k}_1,\omega_1,\alpha_1,\sigma_1}\right\rangle_S \\ &+ \left\langle \overline{\Psi}_{-\mathbf{k}_2,-\omega_2,\alpha_2,\sigma_2'}\Psi_{\mathbf{k}_1,\omega_1,\alpha_1,\sigma_1}\right\rangle_S \left\langle \overline{\Psi}_{\mathbf{k}_2,\omega_2,\alpha_2,\sigma_2}\Psi_{-\mathbf{k}_1,-\omega_1,\alpha_1,\sigma_1'}\right\rangle_S\end{aligned} \tag{2.35}$$

Since all the diagrams contributing to $\chi^{\mathrm{SC},c}$ will be proportional to $\beta\delta_{\sum_i \omega_i}\delta_{\sum_i \mathbf{k}_i}$ times the four external propagators, we now define

$$\begin{aligned}-\mathcal{V}_{\mathbf{k}_1,\omega_1,\alpha_1,\sigma_1,\sigma_1';\mathbf{k}_2,\omega_2,\alpha_2,\sigma_2,\sigma_2'} \equiv \frac{1}{2}\beta^{-1}&(i\omega_1-\xi_1)(-i\omega_1-\xi_1)(i\omega_2-\xi_2)(-i\omega_2-\xi_2) \\ &\chi^{\mathrm{SC},c}_{\mathbf{k}_1,\omega_1,\alpha_1,\sigma_1,\sigma_1';\mathbf{k}_2,\omega_2,\alpha_2,\sigma_2,\sigma_2'}\end{aligned} \tag{2.36}$$

with $\xi_1 = \xi_{\mathbf{k}_1,\alpha_1} = \xi_{-\mathbf{k}_1,\alpha_1}$ and $\xi_2 = \xi_{\mathbf{k}_2,\alpha_2} = \xi_{-\mathbf{k}_2,\alpha_2}$. The minus sign in front is a useful convention so that a negative value of $\mathcal{V}$ indicates attraction, while a positive value indicates repulsion. The factor of $\frac{1}{2}$ is a convenient convention whose usefulness will become clear later.

2.5 Bethe-Salpeter equation

Based on its previous definition, one finds that $-\mathcal{V}_{\mathbf{k}_1,\omega_1,\alpha_1,\sigma_1,\sigma_1';\mathbf{k}_2,\omega_2,\alpha_2,\sigma_2,\sigma_2'}$ is given by the sum of all connected diagrams with two outgoing external legs ($\mathbf{k}_2,\omega_2,\alpha_2,\sigma_2$ and $-\mathbf{k}_2,-\omega_2,\alpha_2,\sigma_2'$) and two incoming external legs ($\mathbf{k}_1,\omega_1,\alpha_1,\sigma_1$ and $-\mathbf{k}_1,-\omega_1,\alpha_1,\sigma_1'$), where the external propagators and delta functions are stripped off, and where an overall factor of $\frac{1}{2}$ is added (see Figure 2.2). In order to calculate this, it is advantageous to define $-\Gamma_{\mathbf{k}_1,\omega_1,\alpha_1,\sigma_1,\sigma_1';\mathbf{k}_2,\omega_2,\alpha_2,\sigma_2,\sigma_2'}$ in the exact same way, except that only two-particle irreducible (2PI) diagrams are kept (see Figure 2.3). A 2-particle irreducible diagram is a connected diagram that cannot be split into two admissible diagrams by cutting any two internal propagators. Γ is also called the irreducible vertex and gives the effective interaction between electrons.

As a function of Γ, the total susceptibility is given as an infinite sum of ladders,

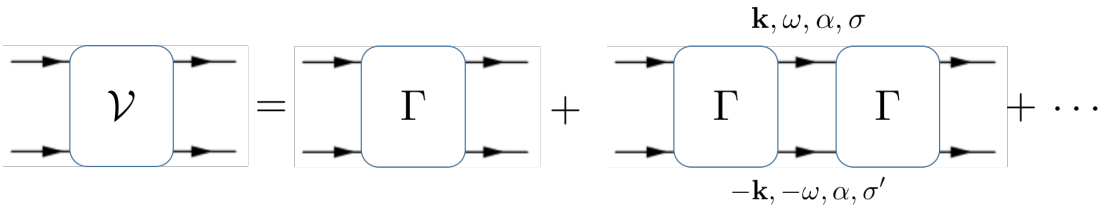

Figure 2.1: Infinite sum of ladder diagrams.

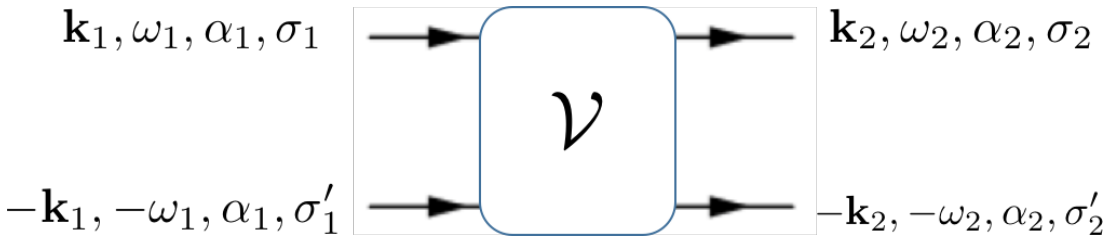

Figure 2.2: Effective vertex in the Cooper channel, given by the sum of all diagrams with the four external legs represented on the figure, and with certain prefactors defined in the text.

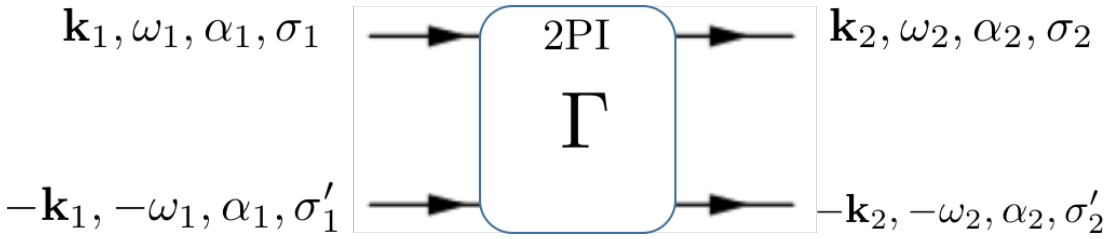

Figure 2.3: Γ is defined in the same way as $\mathcal{V}$, except that only 2-particle irreducible diagrams are summed over.

as shown in Figure 2.1:

$$\begin{aligned} -\mathcal{V} &= -\Gamma + \Gamma \diamond \mathcal{G}^0 \diamond \Gamma - \Gamma \diamond \mathcal{G}^0 \diamond \Gamma \diamond \mathcal{G}^0 \diamond \Gamma + \dots \\ &= -\Gamma + \Gamma \diamond \mathcal{G}^0 \diamond \mathcal{V} \end{aligned} \tag{2.37}$$

where

$$(A \diamond B)_{\mathbf{k}_1,\omega_1,\alpha_1,\sigma_1,\sigma_1';\mathbf{k}_2,\omega_2,\alpha_2,\sigma_2,\sigma_2'} = \frac{1}{\beta} \sum_{\mathbf{k},\omega,\alpha,\sigma,\sigma'} A_{\mathbf{k}_1,\omega_1,\alpha_1,\sigma_1,\sigma_1';\mathbf{k},\omega,\alpha,\sigma,\sigma'} B_{\mathbf{k},\omega,\alpha,\sigma,\sigma';\mathbf{k}_2,\omega_2,\alpha_2,\sigma_2,\sigma_2'} \tag{2.38}$$

and

$$\mathcal{G}^0_{\mathbf{k}_1,\omega_1,\alpha_1,\sigma_1,\sigma_1';\mathbf{k}_2,\omega_2,\alpha_2,\sigma_2,\sigma_2'} = \beta \delta_{\mathbf{k}_1,\omega_1,\alpha_1,\sigma_1,\sigma_1';\mathbf{k}_2,\omega_2,\alpha_2,\sigma_2,\sigma_2'} (i\omega_1 - \xi_{\mathbf{k}_1,\alpha_1})^{-1} \, (-i\omega_1 - \xi_{-\mathbf{k}_1,\alpha_1})^{-1}. \tag{2.39}$$

Combining these definitions, one finds

$$\left(\Gamma \diamond \mathcal{G}^0 \diamond \Gamma\right)_{\mathbf{k}_1,\omega_1,\alpha_1,\sigma_1,\sigma_1';\mathbf{k}_2,\omega_2,\alpha_2,\sigma_2,\sigma_2'} = \frac{1}{\beta}\sum_{\mathbf{k},\omega,\alpha,\sigma,\sigma'} (i\omega - \xi_{\mathbf{k},\alpha})^{-1}\,(-i\omega - \xi_{-\mathbf{k},\alpha})^{-1}\Gamma_{\mathbf{k}_1,\omega_1,\alpha_1,\sigma_1,\sigma_1';\mathbf{k},\omega,\alpha,\sigma,\sigma'}\Gamma_{\mathbf{k},\omega,\alpha,\sigma,\sigma';\mathbf{k}_2,\omega_2,\alpha_2,\sigma_2,\sigma_2'} \tag{2.40}$$

Equation 2.37 is the Bethe-Salpeter equation [98]. Several comments are in order at this point. Two approximations were made. First, we used free propagators instead of renormalized ones. This is justified in the weak coupling limit by the fact that the use of renormalized propagators would only lead to subdominant corrections in U/t [99]. Second, we did not allow for the pair of internal propagators with opposite momenta and frequencies linking two consecutive Γ blocks to be on different bands. The sum over internal momenta and frequencies for each such pair leads to a logarithmically diverging contribution that is responsible for the pairing instability. This diverging contribution only arises in the case where the two propagators in the pair have the same energy, which forces them to be on the same band due to inversion symmetry. This is why we have left out diagrams where the two rails of the ladder are on different bands, as they lead to non-divergent terms. Finally, we note that the permutation of propagators inside such a pair leads to a symmetry factor of $1/2$ for each pair. The factor of $1/2$ introduced in the definition of ν and Γ takes care of this.

The solution of the Bethe-Salpeter equation is given by

$$\mathcal{V} = (1 + \Gamma \diamond \mathcal{G}_0)^{-1} \diamond \Gamma \tag{2.41}$$

where the inverse is understood for the $\diamond$ product. The eigenvectors ψ of the operator $\Gamma \diamond \mathcal{G}_0$ are given by

$$\Gamma \diamond \mathcal{G}_0 \diamond \psi = \lambda\psi \tag{2.42}$$

The Cooper susceptibility $\mathcal{V}$ becomes divergent for $\lambda = -1$, marking the onset of superconductivity. The onset of superconductivity therefore corresponds to the solution

of the following equation:

$$\frac{1}{\beta}\sum_{\mathbf{k},\omega,\alpha,\sigma,\sigma'}\Gamma_{\mathbf{k}_1,\omega_1,\alpha_1,\sigma_1,\sigma_1';\mathbf{k},\omega,\alpha,\sigma,\sigma'}(i\omega-\xi_{\mathbf{k},\alpha})^{-1}\,(-i\omega-\xi_{-\mathbf{k},\alpha})^{-1}\psi_{\mathbf{k},\omega,\alpha,\sigma,\sigma'}=-\psi_{\mathbf{k}_1,\omega_1,\alpha_1,\sigma_1,\sigma_1'} \tag{2.43}$$

2.5.1 Frequency dependence

One now needs to calculate Γ, which is the step where physical insight about the mechanism driving superconductivity is needed. We first treat the dependence of Γ on the Matsubara frequencies. For conventional superconductors, the effective interaction between electrons due to electron-phonon coupling is attractive at low frequencies and repulsive at high frequencies. Low and high frequencies are to be understood compared to the typical phonon frequency, the Debye frequency ω_D. An approximation for Γ that was shown to capture the right qualitative behaviour is then given by [97]:

$$\Gamma_{\mathbf{k}_1,\omega_1,\alpha_1,\sigma_1,\sigma_1';\mathbf{k}_2,\omega_2,\alpha_2,\sigma_2,\sigma_2'}=\begin{cases}\Gamma^{\text{Phon.}}_{\mathbf{k}_1,\alpha_1,\sigma_1,\sigma_1';\mathbf{k}_2,\alpha_2,\sigma_2,\sigma_2'} & \text{if } |\omega_1|,|\omega_2|<\omega_D\\ 0 \quad \text{otherwise}\end{cases} \tag{2.44}$$

where $\Gamma^{\text{Phon.}}_{\mathbf{k}_1,\alpha_1,\sigma_1,\sigma_1';\mathbf{k}_2,\alpha_2,\sigma_2,\sigma_2'}$ has a dominant short-range attractive component leading to the celebrated s-wave order parameter in conventional superconductors.

For a purely electronic mechanism, a natural cutoff would be of the order of the bare bandwidth $\omega_c \sim W \sim v_F k_F$. Actually, in a spin-fluctuation type scenario where the renormalized interaction is calculated from the random phase approximation, this cutoff is largely reduced if the Fermi liquid is close to a magnetic instability. Due to the proximity to this phase transition, the spin fluctuations exhibit a "critical slowing down" [100], whereby their velocity is reduced from the Fermi velocity: $v' \sim v_F(1-\rho U)/\rho U$, where ρ is the density of states at the Fermi level. According to the Stoner criterion, the magnetic transition appears at $\rho U = 1$. Close to to the transition, one has $\rho U = 1-\eta$ with $\eta \ll 1$ and the cutoff is therefore strongly reduced: $\omega_c' \sim v' k_F \sim \eta W$. From the above discussion, it is clear that, in the limit

$U/t \to 0$ treated in this thesis, the cutoff will be given by the bare bandwidth since $\rho U \to 0$.

Neglecting the frequency dependence of Γ apart from the presence of a cutoff, we will therefore take

$$\Gamma_{\mathbf{k}_1,\omega_1,\alpha_1,\sigma_1,\sigma_1';\mathbf{k}_2,\omega_2,\alpha_2,\sigma_2,\sigma_2'} = \begin{cases} \Gamma_{\mathbf{k}_1,\alpha_1,\sigma_1,\sigma_1';\mathbf{k}_2,\alpha_2,\sigma_2,\sigma_2'} & \text{if } |\omega_1|, |\omega_2| < \omega_c \\ 0 \quad \text{otherwise} \end{cases} \tag{2.45}$$

where, crucially, $\Gamma_{\mathbf{k}_1,\alpha_1,\sigma_1,\sigma_1';\mathbf{k}_2,\alpha_2,\sigma_2,\sigma_2'}$ is repulsive at short distance but attractive at large distance, leading to unconventional order parameters. $\Gamma_{\mathbf{k}_1,\alpha_1,\sigma_1,\sigma_1';\mathbf{k}_2,\alpha_2,\sigma_2,\sigma_2'}$ will be calculated perturbatively in the following.

A solution is now found by posing

$$\psi_{\mathbf{k},\omega,\alpha,\sigma,\sigma'} = \begin{cases} \Delta_{\mathbf{k},\alpha,\sigma,\sigma'} \text{ if } |\omega| < \omega_c \\ 0 \text{ otherwise} \end{cases} \tag{2.46}$$

and by rewriting Equation 2.43 as

$$\frac{1}{\beta} \sum_{\mathbf{k},\alpha,\sigma,\sigma'} \Gamma_{\mathbf{k}_1,\alpha_1,\sigma_1,\sigma_1';\mathbf{k},\alpha,\sigma,\sigma'} \Delta_{\mathbf{k},\alpha,\sigma,\sigma'} \sum_{|\omega|<\omega_c} (i\omega - \xi_{\mathbf{k},\alpha})^{-1} (-i\omega - \xi_{-\mathbf{k},\alpha})^{-1} = -\Delta_{\mathbf{k}_1,\alpha_1,\sigma_1,\sigma_1'}. \tag{2.47}$$

As usual, the frequency sum can be performed by substituting $i\omega$ by a complex variable z and using Cauchy's theorem:

$$\frac{1}{\beta} \sum_{|\omega|<\omega_c} g(i\omega) = \sum_j \mathrm{Res}_{z=z_j}[g(z)] n_F(z_j) - \oint_{|z|=\omega_c} \frac{dz}{2\pi i} n_F(z) g(z) \tag{2.48}$$

where j indexes the poles of $g(z)$ enclosed by the contour defined by $|z| = \omega_c$ and where $n_F(z) = (e^{\beta z}+1)^{-1}$. We want to apply this formula for $g(z) = (z-\xi_{\mathbf{k},\alpha})^{-1}(-z-\xi_{-\mathbf{k},\alpha})^{-1}$. For a given value of $\mathbf{k}$, the two poles in the complex plane are situated at $z = \pm\xi_{\mathbf{k},\alpha}$. There are therefore two possibilities: either $\xi_{\mathbf{k},\alpha} < \omega_c$ and the contour encloses these poles, or $\xi_{\mathbf{k},\alpha} > \omega_c$ and it does not. Since the superconducting critical

temperature T_c will emerge as a new energy scale exponentially smaller than the cutoff, one can assume $\beta\omega_c \gg 1$ and therefore neglect the second term in the right hand side of Eq. 2.48, leading to

$$\frac{1}{\beta}\sum_{|\omega|<\omega_c}(i\omega-\xi_{\mathbf{k},\alpha})^{-1}(-i\omega-\xi_{-\mathbf{k},\alpha})^{-1} \simeq \begin{cases} \frac{\tanh\left(\frac{1}{2}\beta\xi_{\mathbf{k},\alpha}\right)}{2\xi_{\mathbf{k},\alpha}} & \text{if } |\xi_{\mathbf{k},\alpha}|<\omega_c \\ 0 \quad \text{otherwise} \end{cases} \tag{2.49}$$

Going back to Equation 2.47, the onset of superconductivity is controlled by the following equation:

$$\sum_{\alpha,\sigma,\sigma'}\sum_{\mathbf{k}}{}' \Gamma_{\mathbf{k}_1,\alpha_1,\sigma_1,\sigma_1';\mathbf{k},\alpha,\sigma,\sigma'}\Delta_{\mathbf{k},\alpha,\sigma,\sigma'}\frac{\tanh\left(\frac{1}{2}\beta\xi_{\mathbf{k},\alpha}\right)}{2\xi_{\mathbf{k},\alpha}} = -\Delta_{\mathbf{k}_1,\alpha_1,\sigma_1,\sigma_1'}. \tag{2.50}$$

where $\sum_{\mathbf{k}}'$ is a sum over all momenta such that $|\xi_{\mathbf{k},\alpha}| < \omega_c$. This is the famous linearised gap equation [42], which can also be obtained by imposing self-consistency in a mean-field treatment of superconductivity, as explained in the following.

2.5.2 Solution of the linearised gap equation

In order to solve the last equation, it is advantageous to rewrite the sum over momenta by a sum over $(\xi, \hat{\mathbf{k}})$, where $\hat{\mathbf{k}}$ lies on the iso-surface defined by $\xi_{\hat{\mathbf{k}},\alpha} = \xi$:

$$\sum_{\alpha}\sum_{\mathbf{k}}{}' \cdots = \sum_{\alpha}\int_{-\omega_c}^{\omega_c} d\xi\ \rho_{\xi,\alpha}\int_{S_{\xi,\alpha}}\frac{d\hat{\mathbf{k}}}{|S_{\xi,\alpha}|}\frac{\overline{v}_{\xi,\alpha}}{v_{\xi,\hat{\mathbf{k}},\alpha}}\ldots \tag{2.51}$$

where $\rho_{\xi,\alpha} = \int_{S_{\xi,\alpha}}\frac{d\hat{\mathbf{k}}}{(2\pi)^D}\frac{1}{v_{\xi,\hat{\mathbf{k}},\alpha}}$ is the density of states of band α at energy ξ, $S_{\xi,\alpha}$ is the Fermi surface of band α at energy ξ, $|S_{\xi,\alpha}|$ is the area of this Fermi surface, $v_{\xi,\hat{\mathbf{k}},\alpha}$ is the group velocity of band α at energy ξ and momentum $\hat{\mathbf{k}}$, and $\overline{v}_{\xi,\alpha} = \left(\int_{S_{\xi,\alpha}}\frac{d\hat{\mathbf{k}}}{|S_{\xi,\alpha}|}\frac{1}{v_{\xi,\hat{\mathbf{k}},\alpha}}\right)^{-1}$ its average.

The gap equation can be rewritten as

$$\int_{-\omega_c}^{\omega_c} d\xi\ f(\xi)\frac{\tanh\left(\frac{\beta\xi}{2}\right)}{2\xi} = -\Delta_{(\xi_1,\hat{\mathbf{k}}_1),\alpha_1,\sigma_1,\sigma_1'} \tag{2.52}$$

with

$$f(\xi) \equiv \sum_{\alpha} \rho_{\xi,\alpha} \int_{S_{\xi,\alpha}} \frac{d\hat{\mathbf{k}}}{|S_{\xi,\alpha}|} \frac{\overline{v}_{\xi,\alpha}}{v_{\xi,\hat{\mathbf{k}},\alpha}} \sum_{\sigma,\sigma'} \Gamma_{(\xi_1,\hat{\mathbf{k}}_1),\alpha_1,\sigma_1,\sigma_1';(\xi,\hat{\mathbf{k}}),\alpha,\sigma,\sigma'} \Delta_{(\xi,\hat{\mathbf{k}}),\alpha,\sigma,\sigma'} \tag{2.53}$$

Due to the $\tanh\left(\frac{\beta\xi}{2}\right)/2\xi$ factor, the sum is dominated by behaviour at small ξ, and we can use the following Taylor expansion:

$$f(\xi) = f(0) + f'(0)\xi + \frac{1}{2}f''(0)\xi^2 + \dots \tag{2.54}$$

This leads to

$$\int_{-\omega_c}^{\omega_c} d\xi \; f(\xi) \frac{\tanh\left(\frac{\beta\xi}{2}\right)}{2\xi} = f(0) \log\left(\frac{2e^{\gamma}\beta\omega_c}{\pi}\right) + \dots \tag{2.55}$$

where $\dots$ stands for terms that are regular in the $T \to 0$ limit. These terms would lead to multiplicative factors of order one for T_c, which we will neglect.

Finally, the gap equation becomes

$$\sum_{\alpha} \rho_{\alpha} \int_{S_{\alpha}} \frac{d\hat{\mathbf{k}}}{|S_{\alpha}|} \frac{\overline{v}_{\alpha}}{v_{\hat{\mathbf{k}},\alpha}} \sum_{\sigma,\sigma'} \Gamma_{\hat{\mathbf{k}}_1,\alpha_1,\sigma_1,\sigma_1';\hat{\mathbf{k}},\alpha,\sigma,\sigma'} \Delta_{\hat{\mathbf{k}},\alpha,\sigma,\sigma'} = -\log\left(\frac{2e^{\gamma}\beta\omega_c}{\pi}\right)^{-1} \Delta_{\hat{\mathbf{k}}_1,\alpha_1,\sigma_1,\sigma_1'}. \tag{2.56}$$

where all quantities are evaluated at the Fermi level.

It is now advantageous to introduce the dimensionless pairing matrix g and its eigenmodes defined by

$$\sum_{\alpha} \sum_{\sigma,\sigma'} \int_{S_{\alpha}} \frac{d\hat{\mathbf{k}}}{|S_{\alpha}|} g_{\hat{\mathbf{k}}_1,\alpha_1,\sigma_1,\sigma_1';\hat{\mathbf{k}},\alpha,\sigma,\sigma'} \varphi_{\hat{\mathbf{k}},\alpha,\sigma,\sigma'} = \lambda \; \varphi_{\hat{\mathbf{k}}_1,\alpha_1,\sigma_1,\sigma_1'} \tag{2.57}$$

where

$$g_{\hat{\mathbf{k}}_1,\alpha_1,\sigma_1,\sigma_1';\hat{\mathbf{k}}_2,\alpha_2,\sigma_2,\sigma_2'} \equiv \sqrt{\rho_{\alpha_1} \frac{\overline{v}_{\alpha_1}}{v_{\hat{\mathbf{k}}_1,\alpha_1}}} \Gamma_{\hat{\mathbf{k}}_1,\alpha_1,\sigma_1,\sigma_1';\hat{\mathbf{k}}_2,\alpha_2,\sigma_2,\sigma_2'} \sqrt{\rho_{\alpha_2} \frac{\overline{v}_{\alpha_2}}{v_{\hat{\mathbf{k}}_2,\alpha_2}}}. \tag{2.58}$$

Since Γ is non-singular in the limit $T \to 0$ and we expect $T_c \ll W$, we neglect the temperature dependence of Γ and we will compute it at $T = 0$ in the next section.

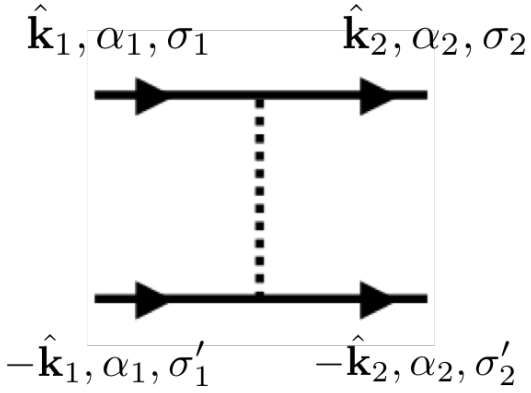

Figure 2.4: Only diagram at order U.

For each $\lambda < 0$, we have a solution of the linearised gap equation given by

$$\begin{aligned} T_c &= \mathcal{W} \exp\left(\frac{1}{\lambda}\right) \\ \Delta_{\hat{\mathbf{k}},\alpha,\sigma,\sigma'} \propto \tilde{\varphi}_{\hat{\mathbf{k}},\alpha,\sigma,\sigma'} &\equiv \sqrt{\frac{\rho_\alpha \ \overline{v}_\alpha}{v_{\hat{\mathbf{k}},\alpha}}}^{-1} \ \varphi_{\hat{\mathbf{k}},\alpha,\sigma,\sigma'} \end{aligned} \tag{2.59}$$

where $\mathcal{W} = \frac{2e^\gamma \omega_c}{\pi} \simeq 1.13 \ \omega_c$ is of the order of the bandwidth. By solving the eigenproblem of Eq. 2.57, we thus obtain T_c from the eigenvalue and the order parameter Δ from the eigenvector. The eigenmode with the most negative eigenvalue corresponds to the order parameter with the highest T_c. After discretization of the Fermi surfaces, g becomes a hermitian matrix that is readily diagonalized numerically.

Note that the eigenvectors of g are orthonormal:

$$\sum_\alpha \sum_{\sigma,\sigma'} \int_{S_\alpha} \frac{d\hat{\mathbf{k}}}{|S_\alpha|} \left(\varphi^{(i)}_{\mathbf{k},\alpha,\sigma,\sigma'}\right)^* \varphi^{(j)}_{\mathbf{k},\alpha,\sigma,\sigma'} = \delta_{i,j} \tag{2.60}$$

where i and j are eigenvector indices.

2.6 Calculation of the effective interaction

What is now left to do is to compute Γ at leading order in U/t for the interaction given in Eq. 3.11 by using the Feynman rules given in Section 2.4.1. As a reminder, $\Gamma_{\mathbf{k}_1,\omega_1,\alpha_1,\sigma_1,\sigma_1';\mathbf{k}_2,\omega_2,\alpha_2,\sigma_2,\sigma_2'}$ is defined as the sum of all connected, irreducible diagrams

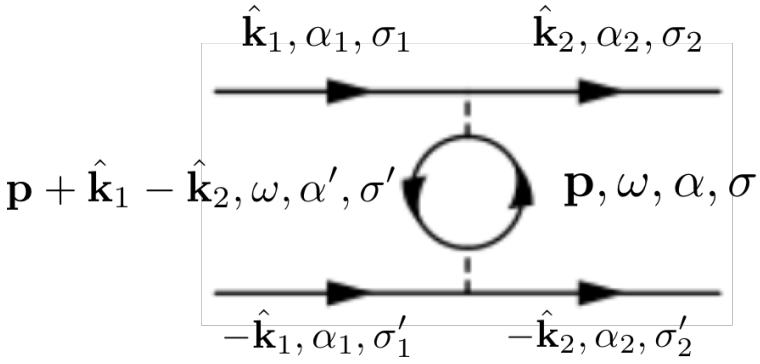

Figure 2.5: First diagram at order U^2. The external legs have $\omega = 0$.

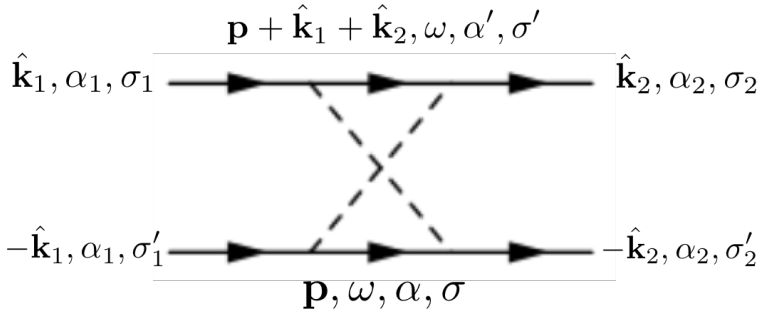

Figure 2.6: Second diagram at order U^2. The external legs have $\omega = 0$.

with two outgoing external legs ($\mathbf{k}_2, \omega_2, \alpha_2, \sigma_2$ and $-\mathbf{k}_2, -\omega_2, \alpha_2, \sigma_2'$) and two incoming external legs ($\mathbf{k}_1, \omega_1, \alpha_1, \sigma_1$ and $-\mathbf{k}_1, -\omega_1, \alpha_1, \sigma_1'$), where the external propagators and Delta functions are stripped off, and where an overall factor of $\frac{1}{2}$ is added (see Figure 2.2). Given the results of last section, we will only need the zero frequency components of the effective interaction: $\Gamma_{\hat{\mathbf{k}}_1,\alpha_1,\sigma_1,\sigma_1';\hat{\mathbf{k}}_2,\alpha_2,\sigma_2,\sigma_2'} \equiv \Gamma_{\hat{\mathbf{k}}_1,\omega_1=0,\alpha_1,\sigma_1,\sigma_1';\hat{\mathbf{k}}_2,\omega_2=0,\alpha_2,\sigma_2,\sigma_2'}$. The external propagators of our diagrams will therefore have $\omega = 0$.

At order U, there is only one diagram, shown in figure 2.4. Its contribution to Γ is

$$\Gamma^{(1)}_{\hat{\mathbf{k}}_1,\alpha_1,\sigma_1,\sigma_1';\hat{\mathbf{k}}_2,\alpha_2,\sigma_2,\sigma_2'} = \frac{1}{2} V_{\hat{\mathbf{k}}_1,\alpha_1,\sigma_1,-\hat{\mathbf{k}}_1,\alpha_1,\sigma_1';-\hat{\mathbf{k}}_2,\alpha_2,\sigma_2',\hat{\mathbf{k}}_2,\alpha_2,\sigma_2}. \tag{2.61}$$

As a reminder, in the case of a single-orbital, spin $SU(2)$-symmetric Hubbard model, the interaction is given by

$$V^{\text{Hub.}}_{s_1,s_1';s_2',s_2} = U\delta_{s_1,-s_1'}\delta_{s_2,-s_2'}(\delta_{s_1',s_2'} - \delta_{s_1',s_2}). \tag{2.62}$$

This would lead to

$$\Gamma^{(1),\mathrm{Hub.}}_{\hat{\mathbf{k}}_1,s_1,s_1';\hat{\mathbf{k}}_2,s_2,s_2'} = \frac{1}{2}U\delta_{s_1,-s_1'}\delta_{s_2,-s_2'}(\delta_{s_1',s_2'} - \delta_{s_1',s_2}). \tag{2.63}$$

At order U^2, there are two diagrams, given in Figures 2.5 and 2.6. Their contribution can be expressed in terms of the following function:

$$\begin{aligned} F_{\hat{\mathbf{k}}_1,\alpha_1,\sigma_1,\sigma_1';\hat{\mathbf{k}}_2,\alpha_2,\sigma_2,\sigma_2'} \equiv &- \sum_{\alpha,\alpha',\sigma,\sigma'} \sum_{\mathbf{p}} \frac{1}{\beta} \sum_{\omega} (i\omega - \xi_{\mathbf{p},\alpha})^{-1} (i\omega - \xi_{\mathbf{p}+\hat{\mathbf{k}}_1-\hat{\mathbf{k}}_2,\alpha'})^{-1} \\ &V_{\hat{\mathbf{k}}_1,\alpha_1,\sigma_1,\mathbf{p},\alpha,\sigma;\mathbf{p}+\hat{\mathbf{k}}_1-\hat{\mathbf{k}}_2,\alpha',\sigma',\hat{\mathbf{k}}_2,\alpha_2,\sigma_2} V_{-\hat{\mathbf{k}}_1,\alpha_1,\sigma_1';\mathbf{p}+\hat{\mathbf{k}}_1-\hat{\mathbf{k}}_2,\alpha',\sigma';\mathbf{p},\alpha,\sigma;-\hat{\mathbf{k}}_2,\alpha_2,\sigma_2}. \end{aligned} \tag{2.64}$$

In terms of this function, we have

$$\Gamma^{(2)}_{\hat{\mathbf{k}}_1,\alpha_1,\sigma_1,\sigma_1';\hat{\mathbf{k}}_2,\alpha_2,\sigma_2,\sigma_2'} = \frac{1}{2}\left(-F_{\hat{\mathbf{k}}_1,\alpha_1,\sigma_1,\sigma_1';\hat{\mathbf{k}}_2,\alpha_2,\sigma_2,\sigma_2'} + F_{\hat{\mathbf{k}}_1,\alpha_1,\sigma_1,\sigma_1';-\hat{\mathbf{k}}_2,\alpha_2,\sigma_2',\sigma_2}\right) \tag{2.65}$$

where the first term corresponds to the first diagram, and the second term corresponds to the second diagram. The minus sign comes from the fermionic loop in the first diagram. We can now evaluate the Matsubara sum, leading to

$$\begin{aligned} F_{\hat{\mathbf{k}}_1,\alpha_1,\sigma_1,\sigma_1';\hat{\mathbf{k}}_2,\alpha_2,\sigma_2,\sigma_2'} = &- \sum_{\alpha,\alpha',\sigma,\sigma'} \sum_{\mathbf{p}} \frac{n(\xi_{\mathbf{p},\alpha}) - n(\xi_{\mathbf{p}+\hat{\mathbf{k}}_1-\hat{\mathbf{k}}_2,\alpha'})}{\xi_{\mathbf{p},\alpha} - \xi_{\mathbf{p}+\hat{\mathbf{k}}_1-\hat{\mathbf{k}}_2,\alpha'}} \\ &V_{\hat{\mathbf{k}}_1,\alpha_1,\sigma_1;\mathbf{p},\alpha,\sigma;\mathbf{p}+\hat{\mathbf{k}}_1-\hat{\mathbf{k}}_2,\alpha',\sigma';\hat{\mathbf{k}}_2,\alpha_2,\sigma_2} V_{-\hat{\mathbf{k}}_1,\alpha_1,\sigma_1';\mathbf{p}+\hat{\mathbf{k}}_1-\hat{\mathbf{k}}_2,\alpha',\sigma';\mathbf{p},\alpha,\sigma;-\hat{\mathbf{k}}_2,\alpha_2,\sigma_2}. \end{aligned} \tag{2.66}$$

This function can be computed numerically by using the tetrahedron method [101]. Within the approximations made above, one can neglect the temperature dependence of this function and compute it at $T = 0$.

Note that in the single-orbital case, this function would simply be given by

$$F^{\mathrm{Hub.}}_{\hat{\mathbf{k}}_1,s_1,s_1';\hat{\mathbf{k}}_2,s_2,s_2'} = U^2\chi^{\mathrm{ph}}(\hat{\mathbf{k}}_1 - \hat{\mathbf{k}}_2)(\delta_{s_1,s_1'}\delta_{s_2,s_2'}\delta_{s_1,s_2} + \delta_{s_1,-s_1'}\delta_{s_2,-s_2'}\delta_{s_1,-s_2}) \tag{2.67}$$

where $\chi^{\mathrm{ph}}(\mathbf{q})$ is the Lindhard susceptibility, defined by

$$\chi^{\mathrm{ph}}(\mathbf{q}) = -\sum_{\mathbf{p}} \frac{n(\xi_{\mathbf{p}}) - n(\xi_{\mathbf{p}+\mathbf{q}})}{\xi_{\mathbf{p}} - \xi_{\mathbf{p}+\mathbf{q}}}. \tag{2.68}$$

2.6.1 Pseudo-spin dependence

When looking for the eigenmodes $\varphi_{\mathbf{k},\alpha,\sigma,\sigma'}$ of the effective interaction, it is advantageous to go to the aforementioned pseudo-spin basis, since Γ has a block-diagonal structure in that basis. The pseudo-spin transformation separates the pseudo-spin degrees of freedom in a singlet φ_{d_0} and a triplet $\varphi_{\vec{d}}$:

$$\begin{pmatrix} \varphi_{++} & \varphi_{+-} \\ \varphi_{-+} & \varphi_{--} \end{pmatrix} = \frac{1}{\sqrt{2}} \begin{pmatrix} -\varphi_{d_x} + i\varphi_{d_y} & \varphi_{d_z} + \varphi_{d_0} \\ \varphi_{d_z} - \varphi_{d_0} & \varphi_{d_x} + i\varphi_{d_y} \end{pmatrix}, \tag{2.69}$$

where we have left the indices $\mathbf{k}, \alpha$ implicit. Using this unitary transformation on $\Gamma_{\hat{\mathbf{k}}_1,\alpha_1,\sigma_1,\sigma_1';\hat{\mathbf{k}}_2,\alpha_2,\sigma_2,\sigma_2'}$, we obtain $\Gamma_{\hat{\mathbf{k}}_1,\alpha_1,d_{\mu,1};\hat{\mathbf{k}}_2,\alpha_2,d_{\mu,1}}$ with $\mu = 0, x, y, z$.

In the following, we will use the notation $\Gamma_{\sigma_1,\sigma_1';\sigma_2,\sigma_2'}$ for the matrix

$$(\Gamma_{\sigma_1,\sigma_1';\sigma_2,\sigma_2'})_{\hat{\mathbf{k}}_1,\alpha_1;\hat{\mathbf{k}}_2,\alpha_2} \equiv \Gamma_{\hat{\mathbf{k}}_1,\alpha_1,\sigma_1,\sigma_1';\hat{\mathbf{k}}_2,\alpha_2,\sigma_2,\sigma_2'} \tag{2.70}$$

and $\Gamma_{d_{\mu,1};d_{\mu,2}}$ for the matrix

$$(\Gamma_{d_{\mu,1};d_{\mu,2}})_{\hat{\mathbf{k}}_1,\alpha_1;\hat{\mathbf{k}}_2,\alpha_2} \equiv \Gamma_{\hat{\mathbf{k}}_1,\alpha_1,d_{\mu,1};\hat{\mathbf{k}}_2,\alpha_2,d_{\mu,2}}. \tag{2.71}$$

Using inversion symmetry, we find $\Gamma_{\sigma_1,\sigma_1';\sigma_2,\sigma_2'} = \Gamma_{\sigma_1',\sigma_1;\sigma_2',\sigma_2}$. Using this last relation, we find $\Gamma_{d_0;\vec{d}} = 0$, which means that the pseudo-spin singlet and triplet channels are decoupled.

Furthermore, Γ is invariant under the double group symmetry operations discussed in Section 2.3.1:

$$\begin{aligned} \mathcal{R}(\Gamma_{d_0;d_0})_{\hat{\mathbf{k}}_1,\alpha_1;\hat{\mathbf{k}}_2,\alpha_2}\mathcal{R}^{-1} &\equiv (\Gamma_{d_0;d_0})_{\mathcal{R}\hat{\mathbf{k}}_1,\alpha_1;\mathcal{R}\hat{\mathbf{k}}_2,\alpha_2} = (\Gamma_{d_0;d_0})_{\hat{\mathbf{k}}_1,\alpha_1;\hat{\mathbf{k}}_2,\alpha_2} \\ \mathcal{R}(\Gamma_{\vec{d};\vec{d}})_{\hat{\mathbf{k}}_1,\alpha_1;\hat{\mathbf{k}}_2,\alpha_2}\mathcal{R}^{-1} &\equiv (\Gamma_{\mathcal{R}\vec{d};\mathcal{R}\vec{d}})_{\mathcal{R}\hat{\mathbf{k}}_1,\alpha_1;\mathcal{R}\hat{\mathbf{k}}_2,\alpha_2} = (\Gamma_{\vec{d};\vec{d}})_{\hat{\mathbf{k}}_1,\alpha_1;\hat{\mathbf{k}}_2,\alpha_2}. \end{aligned} \tag{2.72}$$

This means that its eigenvectors can be classified according to the irreducible representations of the point group.

As explained in Section 3.2.2, the interaction considered for the case of Sr_2RuO_4

actually conserves total pseudo-spin modulo 4 thanks to a $z \to -z$ mirror symmetry. In that case, $\Gamma_{\sigma_1,\sigma_1';\sigma_2,\sigma_2'}$ is non-zero only when $\frac{1}{2}(\sigma_1+\sigma_1') = \frac{1}{2}(\sigma_2+\sigma_2') \mod 2$ (which means that $\Gamma_{+1,-1;+1,+1} = 0$ for example) and the d_z and the d_x, d_y sectors are therefore not coupled. In matrix form, one can write $\Gamma_{d_{\mu,1};d_{\mu,2}}$ as

$$\begin{pmatrix} \Gamma_{d_0,d_0} & 0 & 0 & 0 \\ 0 & \Gamma_{d_z,d_z} & 0 & 0 \\ 0 & 0 & \Gamma_{d_x,d_x} & \Gamma_{d_x,d_y} \\ 0 & 0 & \Gamma_{d_y,d_x} & \Gamma_{d_y,d_y} \end{pmatrix} \tag{2.73}$$

in the basis $[d_0, d_z, d_x, d_y]$. The matrix elements are given by

$$\begin{aligned} \Gamma_{d_0,d_0} &= \Gamma_{+-;+-} - \Gamma_{+-;-+} \\ \Gamma_{d_z,d_z} &= \Gamma_{+-;+-} + \Gamma_{+-;-+} \\ \Gamma_{d_x,d_x} &= \frac{1}{2}(\Gamma_{++;++} - \Gamma_{++;--} - \Gamma_{--;++} + \Gamma_{--;--}) \\ \Gamma_{d_x,d_y} &= i\frac{1}{2}(-\Gamma_{++;++} - \Gamma_{++;--} + \Gamma_{--;++} + \Gamma_{--;--}) \\ \Gamma_{d_y,d_x} &= -i\frac{1}{2}(-\Gamma_{++;++} + \Gamma_{++;--} - \Gamma_{--;++} + \Gamma_{--;--}) \\ \Gamma_{d_y,d_y} &= \frac{1}{2}(\Gamma_{++;++} + \Gamma_{++;--} + \Gamma_{--;++} + \Gamma_{--;--}). \end{aligned} \tag{2.74}$$

We can now inject the formulas found for $\Gamma_{\sigma_1,\sigma_1';\sigma_2,\sigma_2'}$ in the last section. It is advantageous to define the following matrices

$$(F^{\pm}_{\sigma_1,\sigma_1';\sigma_2,\sigma_2'})_{\hat{\mathbf{k}}_1,\alpha_1;\hat{\mathbf{k}}_2,\alpha_2} = -\frac{1}{2}\left(F_{\hat{\mathbf{k}}_1,\alpha_1,\sigma_1,\sigma_1';\hat{\mathbf{k}}_2,\alpha_2,\sigma_2,\sigma_2'} \pm F_{\hat{\mathbf{k}}_1,\alpha_1,\sigma_1,\sigma_1';-\hat{\mathbf{k}}_2,\alpha_2,\sigma_2,\sigma_2'}\right). \tag{2.75}$$

The operator F^+ (F^-) is non-zero only in the even (odd) parity subspace, defined by $\varphi_{\hat{\mathbf{k}},\alpha} = \varphi_{-\hat{\mathbf{k}},\alpha}$ ($\varphi_{\hat{\mathbf{k}},\alpha} = -\varphi_{-\hat{\mathbf{k}},\alpha}$).

2.6.1.1 Pseudo-spin triplet

Using inversion symmetry and the fact that we have an on-site interaction, it is easy to see that $\Gamma^{(1)}_{\sigma_1,\sigma_1';\sigma_2,\sigma_2'} = -\Gamma^{(1)}_{\sigma_1,\sigma_1';\sigma_2',\sigma_2} = -\Gamma^{(1)}_{\sigma_1',\sigma_1;\sigma_2,\sigma_2'}$. The order U term is therefore

zero in the triplet channel.

As mentioned previously, there are two decoupled sectors, corresponding to two different orientations of $\vec{d}$: out-of-plane (d_z) and in-plane (d_x, d_y). Since the order U term is zero, we go directly to the order U^2 term. In the d_z case, the effective interaction is given by

$$\Gamma^{(2)}_{d_z,d_z} = F^-_{+,-;+,-} + F^-_{+,-;-,+}. \tag{2.76}$$

In the in-plane case, the effective interaction is given by

$$\begin{aligned}
\Gamma^{(2)}_{d_x,d_x} &= \frac{1}{2}(F^-_{++;++} - F^-_{++;--} - F^-_{--;++} + F^-_{--;--}) \\
\Gamma^{(2)}_{d_x,d_y} &= i\frac{1}{2}(-F^-_{++;++} - F^-_{++;--} + F^-_{--;++} + F^-_{--;--}) \\
\Gamma^{(2)}_{d_y,d_x} &= -i\frac{1}{2}(-F^-_{++;++} + F^-_{++;--} - F^-_{--;++} + F^-_{--;--}) \\
\Gamma^{(2)}_{d_y,d_y} &= \frac{1}{2}(F^-_{++;++} + F^-_{++;--} + F^-_{--;++} + F^-_{--;--}).
\end{aligned} \tag{2.77}$$

In the single-orbital Hubbard case, this would lead to

$$(\Gamma^{(2),\text{Hub.}}_{d_z,d_z})_{\hat{\mathbf{k}}_1;\hat{\mathbf{k}}_2} = \frac{1}{2}\left(U^2\chi^{\text{ph}}(\hat{\mathbf{k}}_1 + \hat{\mathbf{k}}_2) - U^2\chi^{\text{ph}}(\hat{\mathbf{k}}_1 - \hat{\mathbf{k}}_2)\right) \tag{2.78}$$

and

$$\begin{aligned}
(\Gamma^{(2),\text{Hub.}}_{d_x,d_x})_{\hat{\mathbf{k}}_1;\hat{\mathbf{k}}_2} &= \frac{1}{2}(U^2\chi^{\text{ph}}(\hat{\mathbf{k}}_1 + \hat{\mathbf{k}}_2) - U^2\chi^{\text{ph}}(\hat{\mathbf{k}}_1 - \hat{\mathbf{k}}_2)) \\
(\Gamma^{(2),\text{Hub.}}_{d_x,d_y})_{\hat{\mathbf{k}}_1;\hat{\mathbf{k}}_2} &= 0 \\
(\Gamma^{(2),\text{Hub.}}_{d_y,d_x})_{\hat{\mathbf{k}}_1;\hat{\mathbf{k}}_2} &= 0 \\
(\Gamma^{(2),\text{Hub.}}_{d_y,d_y})_{\hat{\mathbf{k}}_1;\hat{\mathbf{k}}_2} &= \frac{1}{2}(U^2\chi^{\text{ph}}(\hat{\mathbf{k}}_1 + \hat{\mathbf{k}}_2) - U^2\chi^{\text{ph}}(\hat{\mathbf{k}}_1 - \hat{\mathbf{k}}_2)).
\end{aligned} \tag{2.79}$$

In the single-orbital Hubbard model case, Γ is isotropic in $\vec{d}$, since, without spin-orbit coupling, the system is $SU(2)$ invariant. This is not the case in general since the in-plane and out-of-plane sectors of Γ are in general different. In the next Chapter, we will show how the difference between the in-plane and out-of-plane sectors due to spin-orbit coupling favours certain order parameters in Sr_2RuO_4.

2.6.1.2 Pseudo-spin singlet

In the singlet channel, the order U term is non-zero:

$$(\Gamma^{(1)}_{d_0,d_0})_{\hat{\mathbf{k}}_1,\alpha_1;\hat{\mathbf{k}}_2,\alpha_2} = V_{\hat{\mathbf{k}}_1,\alpha_1,+,-\hat{\mathbf{k}}_1,\alpha_1,-;-\hat{\mathbf{k}}_2,\alpha_2,-,\hat{\mathbf{k}}_2,\alpha_2,+}. \tag{2.80}$$

In the single-orbital Hubbard case, one would have

$$(\Gamma^{(1),\text{Hub.}}_{d_0,d_0})_{\hat{\mathbf{k}}_1;\hat{\mathbf{k}}_2} = U. \tag{2.81}$$

If $\Gamma^{(1)}_{d_0,d_0}$ has at least one negative eigenvalue, the most negative one gives the leading instability in the pseudo-spin singlet channel, and there is no need to look at order U^2. This is what would happen for the attractive single-orbital Hubbard model, i.e. for $U < 0$.

Instead, in the case of a repulsive bare interaction, relevant to electrons in a solid, the eigenvalues of $\Gamma^{(1)}_{d_0,d_0}$ will be either positive or zero, and there will therefore be no divergence at order U. Nevertheless, a negative eigenvalue could appear at order U^2 in the subspace $\mathcal{S}$ defined by the zero eigenvalues of $\Gamma^{(1)}_{d_0,d_0}$. One should therefore diagonalize $P_{\mathcal{S}}\Gamma^{(2)}_{d_0,d_0}P_{\mathcal{S}}$, where $P_{\mathcal{S}}$ is the projector onto $\mathcal{S}$ and where

$$\Gamma^{(2)}_{d_0,d_0} = F^{+}_{+,-;+,-} - F^{+}_{+,-;-,+}. \tag{2.82}$$

In the single-orbital Hubbard case, the space S is easily defined: it is the space of all $\varphi_{\hat{\mathbf{k}}}$ such that $\sum_{\hat{\mathbf{k}}} \varphi_{\hat{\mathbf{k}}} = 0$. The uniform s-wave order parameter $\varphi_{\hat{\mathbf{k}}} = \varphi \; \forall \; \mathbf{k}$ present in conventional superconductors is therefore disfavored because of the bare repulsion. On the other hand, all order parameters in non-trivial (i.e. non s-wave) irreducible representations of the point group [1] are contained in $\mathcal{S}$ since they satisfy $\sum_{\hat{\mathbf{k}}} \varphi_{\hat{\mathbf{k}}} = 0$ by symmetry. For example, on a square lattice, these non-trivial representations would be given by A_{2g}, B_{1g} and B_{2g} as shown in Table 5.3. In order to find the most

[1] One should of course only consider even-parity representations in the singlet channel in order to satisfy the Pauli principle.

favored of these order parameters, one should diagonalize $P_{\mathcal{S}}\Gamma^{(2)}_{d_0,d_0}P_{\mathcal{S}}$, with

$$(\Gamma^{(2),\text{Hub.}}_{d_0,d_0})_{\hat{\mathbf{k}}_1;\hat{\mathbf{k}}_2} = \frac{1}{2}\left(U^2\chi^{\text{ph}}(\hat{\mathbf{k}}_1+\hat{\mathbf{k}}_2) + U^2\chi^{\text{ph}}(\hat{\mathbf{k}}_1-\hat{\mathbf{k}}_2)\right). \tag{2.83}$$

2.7 Generalized BCS formalism

In the last sections, we have established the presence of a divergence of the susceptibility to Cooper pairing at a critical temperature T_c, corresponding to the most negative eigenvalue of the effective interaction in the Cooper channel. The momentum and band anisotropy of the order parameter was then shown to be given by the corresponding eigenvector. The motivation came from a system in which an infinitesimally small field couples directly to the order parameter. While this technique works well to study the superconducting instability coming from the Fermi liquid, it is not well suited to the study of the system below T_c.

Instead, in order to study the superconducting phase, it would be advantageous to use the Bardeen-Cooper-Schrieffer (BCS) formalism [17] generalized to anisotropic, spin-orbit coupled, multi-orbital systems. We start from a reduced BCS Hamiltonian of the following form:

$$H_{BCS} = H_K + \frac{1}{2}\sum_{\alpha_1,d_{\mu_1}}\sum_{\alpha_2,d_{\mu_2}}{\sum_{\mathbf{k}_1,\mathbf{k}_2}}' V^{BCS}_{\mathbf{k}_1,\alpha_1,d_{\mu_1};\mathbf{k}_2,\alpha_2,d_{\mu_2}}\phi^\dagger_{\mathbf{k}_1,\alpha_1,d_{\mu_1}}\phi_{\mathbf{k}_2,\alpha_2,d_{\mu_2}} \tag{2.84}$$

where H_K is the single-particle part of the Hamiltonian defined in Eq. 3.11, ϕ was defined in Eq. 2.26 and $\sum'_{\mathbf{k}_1,\mathbf{k}_2}$ is a sum over momenta such that $|\xi_{\mathbf{k}_1,\alpha_1}|, |\xi_{\mathbf{k}_2,\alpha_2}| < \omega_c$. In the following, we will omit the $'$ on the sum symbols, but all sums over momenta should be taken with that energy cutoff. Using the effective interaction calculated in the previous sections, we take

$$V^{BCS}_{\mathbf{k}_1,\alpha_1,d_{\mu_1};\mathbf{k}_2,\alpha_2,d_{\mu_2}} = \Gamma_{\mathbf{k}_1,\alpha_1,d_{\mu_1};\mathbf{k}_2,\alpha_2,d_{\mu_2}}. \tag{2.85}$$

We now follow the standard mean-field treatment of this Hamiltonian, by assuming

the following two operators acquire a non-zero expectation value

$$\begin{aligned}\Delta_{\mathbf{k}_1,\alpha_1,d_{\mu_1}} &= \frac{1}{\sqrt{2}}\sum_{\mathbf{k}_2,\alpha_2,d_{\mu_2}} V^{BCS}_{\mathbf{k}_1,\alpha_1,d_{\mu_1};\mathbf{k}_2,\alpha_2,d_{\mu_2}} \left\langle \phi_{\mathbf{k}_2,\alpha_2,d_{\mu_2}} \right\rangle \\ \overline{\Delta}_{\mathbf{k}_2,\alpha_2,d_{\mu_2}} &= \frac{1}{\sqrt{2}}\sum_{\mathbf{k}_1,\alpha_1,d_{\mu_1}} \left\langle \phi^\dagger_{\mathbf{k}_1,\alpha_1,d_{\mu_1}} \right\rangle V^{BCS}_{\mathbf{k}_1,\alpha_1,d_{\mu_1};\mathbf{k}_2,\alpha_2,d_{\mu_2}}.\end{aligned} \tag{2.86}$$

Using these formulas, and neglecting fluctuations, we obtain

$$H_{BCS} = H_K + \frac{1}{2}\sqrt{2}\sum_{\mathbf{k},\alpha,d_\mu}(\Delta_{\mathbf{k},\alpha,d_\mu}\phi^\dagger_{\mathbf{k},\alpha,d_\mu} + \overline{\Delta}_{\mathbf{k},\alpha,d_\mu}\phi_{\mathbf{k},\alpha,d_\mu}) + \overline{\Delta}(V^{BCS})^{-1}\Delta \tag{2.87}$$

with

$$\overline{\Delta}(V^{BCS})^{-1}\Delta = \sum_{\mathbf{k}_1,\alpha_1,d_{\mu,1}}\sum_{\mathbf{k}_2,\alpha_2,d_{\mu,2}} \overline{\Delta}_{\mathbf{k}_1,\alpha_1,d_{\mu,1}}(V^{BCS})^{-1}_{\mathbf{k}_1,\alpha_1,d_{\mu,1};\mathbf{k}_2,\alpha_2,d_{\mu,2}}\Delta_{\mathbf{k}_2,\alpha_2,d_{\mu,2}}. \tag{2.88}$$

This Hamiltonian is now quadratic and can be rewritten as

$$H_{BCS} = \frac{1}{2}\sum_{\mathbf{k},\alpha}\psi^\dagger_{\mathbf{k},\alpha}\mathcal{H}_{\mathbf{k},\alpha}\psi_{\mathbf{k},\alpha} + \text{Constant} \tag{2.89}$$

with $\psi^\dagger_{\mathbf{k},\alpha} = [c^\dagger_{\mathbf{k},\alpha,+}c^\dagger_{\mathbf{k},\alpha,-}c_{-\mathbf{k},\alpha,+}c_{-\mathbf{k},\alpha,-}]$ and

$$\mathcal{H}_{\mathbf{k},\alpha} = \begin{pmatrix} \xi_{\mathbf{k},\alpha} & 0 & -\Delta_{\mathbf{k},\alpha,d_x} + i\Delta_{\mathbf{k},\alpha,d_y} & \Delta_{\mathbf{k},\alpha,d_z} + \Delta_{\mathbf{k},\alpha,d_0} \\ 0 & \xi_{\mathbf{k},\alpha} & \Delta_{\mathbf{k},\alpha,d_z} - \Delta_{\mathbf{k},\alpha,d_0} & \Delta_{\mathbf{k},\alpha,d_x} + i\Delta_{\mathbf{k},\alpha,d_y} \\ -\overline{\Delta}_{\mathbf{k},\alpha,d_x} - i\overline{\Delta}_{\mathbf{k},\alpha,d_y} & \overline{\Delta}_{\mathbf{k},\alpha,d_z} - \overline{\Delta}_{\mathbf{k},\alpha,d_0} & -\xi_{\mathbf{k},\alpha} & 0 \\ \overline{\Delta}_{\mathbf{k},\alpha,d_z} + \overline{\Delta}_{\mathbf{k},\alpha,d_0} & \overline{\Delta}_{\mathbf{k},\alpha,d_x} - i\overline{\Delta}_{\mathbf{k},\alpha,d_y} & 0 & -\xi_{\mathbf{k},\alpha} \end{pmatrix}. \tag{2.90}$$

Note that we used inversion symmetry to write $\xi_{\mathbf{k},\alpha} = \xi_{-\mathbf{k},\alpha}$.

In the previous sections, we diagonalized Γ (more precisely, the pairing matrix g), and we showed that each mode provides a distinct solution of the linearized gap equation with a different value of T_c. These modes are classified according to the irreducible representations of the point group of the lattice. While this works for identifying the mode with the highest T_c, these modes actually become coupled

in the superconducting phase when one goes beyond the linearized version of the self-consistency equation, or equivalently, when one includes quartic terms in the Ginzburg-Landau formalism. In general, one should therefore solve H_{BCS} for all temperatures, and the functional form of the gap can generically have a temperature dependence.

Instead, we make the usual approximation that the order parameter functional form is temperature independent, and that only its overall magnitude depends on T [102]:

$$\Delta_{\mathbf{k},\alpha,d_\mu}(T) = \Delta(T)\ \tilde{\varphi}_{\mathbf{k},\alpha,d_\mu} \tag{2.91}$$

where $\tilde{\varphi}_{\mathbf{k},\alpha,d_\mu}$ is the mode found in Section 2.5, normalized so that

$$\max_{\mathbf{k},\alpha} \sum_{\mu} |\tilde{\varphi}_{\mathbf{k},\alpha,d_\mu}|^2 = 1 \tag{2.92}$$

and where $\Delta(T)$ sets the energy scale of the gap.

2.7.1 Singlet

Let us now discuss different cases. As explained in the previous section, in an inversion-symmetric problem, one can always distinguish between pseudo-spin singlet and triplet. In the singlet case, the only non-zero component of the gap is $\Delta_{\mathbf{k},\alpha,d_0}$. For notational convenience, we define $\Delta_{\mathbf{k},\alpha,d_0} \equiv \Delta_{\mathbf{k},\alpha}$ and the Hamiltonian becomes

$$\mathcal{H}_{\mathbf{k},\alpha} = \begin{pmatrix} \xi_{\mathbf{k},\alpha} & 0 & 0 & \Delta_{\mathbf{k},\alpha} \\ 0 & \xi_{\mathbf{k},\alpha} & -\Delta_{\mathbf{k},\alpha} & 0 \\ 0 & -\overline{\Delta}_{\mathbf{k},\alpha} & -\xi_{\mathbf{k},\alpha} & 0 \\ \overline{\Delta}_{\mathbf{k},\alpha} & 0 & 0 & -\xi_{\mathbf{k},\alpha} \end{pmatrix}. \tag{2.93}$$

Since this matrix can be split into two decoupled blocks, the Hamiltonian can be split into two terms. Using $\Delta_{\mathbf{k},\alpha} = \Delta_{-\mathbf{k},\alpha}$ coming from fermionic statistics, it is easy to see that these two terms are the same, and we therefore only need to diagonalize one of the blocks. Since the Hamiltonian is block diagonal in band space, we can diagonalize

each band separately and omit the band index for now. We can now diagonalize the Hamiltonian using a Bogolyubov transformation:

$$\begin{aligned} c^\dagger_{\mathbf{k},+} &= v'_{\mathbf{k}} a^\dagger_{\mathbf{k}} + v^*_{\mathbf{k}} b_{\mathbf{k}} \\ c^\dagger_{-\mathbf{k},-} &= v'_{\mathbf{k}} b^\dagger_{\mathbf{k}} - v^*_{\mathbf{k}} a_{\mathbf{k}} \end{aligned} \tag{2.94}$$

with

$$\begin{aligned} v'_{\mathbf{k}} &= ie^{-i\Theta_{\mathbf{k}}/2}\cos(\theta_{\mathbf{k}}) \\ v_{\mathbf{k}} &= -ie^{i\Theta_{\mathbf{k}}/2}\sin(\theta_{\mathbf{k}}) \\ \cot(2\theta_{\mathbf{k}}) &= \frac{\xi_{\mathbf{k}}}{|\Delta_{\mathbf{k}}|} \end{aligned} \tag{2.95}$$

where we have parametrized the gap as $\Delta_{\mathbf{k}} = |\Delta_{\mathbf{k}}|e^{i\Theta_{\mathbf{k}}}$ and where $|v'_{\mathbf{k}}|^2 + |v_{\mathbf{k}}|^2 = 1$ in order to preserve anticommutation relations. We also give the inverse transformation for later convenience:

$$\begin{aligned} a^\dagger_{\mathbf{k}} &= (v'_{\mathbf{k}})^* c^\dagger_{\mathbf{k},+} - v^*_{\mathbf{k}} c_{-\mathbf{k},-} \\ b^\dagger_{\mathbf{k}} &= (v'_{\mathbf{k}})^* c^\dagger_{-\mathbf{k},-} + v^*_{\mathbf{k}} c_{\mathbf{k},+}. \end{aligned} \tag{2.96}$$

The Hamiltonian now reads

$$H_{BCS} = \sum_{\mathbf{k},\alpha} E_{\mathbf{k},\alpha}(a^\dagger_{\mathbf{k},\alpha}a_{\mathbf{k},\alpha} + b^\dagger_{\mathbf{k},\alpha}b_{\mathbf{k},\alpha}) + \sum_{\mathbf{k},\alpha}(\xi_{\mathbf{k},\alpha} - E_{\mathbf{k},\alpha}) + \overline{\Delta}(V^{BCS})^{-1}\Delta \tag{2.97}$$

where $E_{\mathbf{k},\alpha} = \sqrt{\xi^2_{\mathbf{k},\alpha} + |\Delta_{\mathbf{k},\alpha}|^2}$.

The gap equation is now obtained by imposing self-consistency:

$$\begin{aligned} \Delta_{\mathbf{k}_1,\alpha_1} &= \frac{1}{\sqrt{2}} \sum_{\mathbf{k}_2,\alpha_2} V^{BCS}_{\mathbf{k}_1,\alpha_1;\mathbf{k}_2,\alpha_2} \langle \phi_{\mathbf{k}_2,\alpha_2} \rangle \\ &= \sum_{\mathbf{k}_2,\alpha_2} V^{BCS}_{\mathbf{k}_1,\alpha_1;\mathbf{k}_2,\alpha_2} (v'_{\mathbf{k}_2,\alpha_2})^* v_{\mathbf{k}_2,\alpha_2} \left(1 - \left\langle a^\dagger_{\mathbf{k}_2,\alpha_2} a_{\mathbf{k}_2,\alpha_2} \right\rangle - \left\langle b^\dagger_{\mathbf{k}_2,\alpha_2} b_{\mathbf{k}_2,\alpha_2} \right\rangle\right) \\ &= -\sum_{\mathbf{k}_2,\alpha_2} V^{BCS}_{\mathbf{k}_1,\alpha_1;\mathbf{k}_2,\alpha_2} \Delta_{\mathbf{k}_2,\alpha_2} \frac{\tanh(E_{\mathbf{k}_2,\alpha_2}/2T)}{2E_{\mathbf{k}_2,\alpha_2}} \end{aligned} \tag{2.98}$$

where the d_0 index is implicit.

At $T = 0$, the gap equation becomes

$$\Delta_{\mathbf{k}_1,\alpha_1} = -\sum_{\mathbf{k}_2,\alpha_2} V^{BCS}_{\mathbf{k}_1,\alpha_1;\mathbf{k}_2,\alpha_2} \Delta_{\mathbf{k}_2,\alpha_2} \frac{1}{2E_{\mathbf{k}_2,\alpha_2}}. \tag{2.99}$$

The sum over momenta is again dominated by the Fermi surface contribution due to the $1/E_{\mathbf{k},\alpha}$ factor. Using the same Taylor expansion used in Section 2.5.2, one finds

$$\varphi_{\hat{\mathbf{k}}_1,\alpha_1} = -\sum_{\alpha_2} \int_{S_{\alpha_2}} \frac{d\hat{\mathbf{k}}_2}{|S_{\alpha_2}|} g_{\hat{\mathbf{k}}_1,\alpha_1;\hat{\mathbf{k}}_2,\alpha_2} \varphi_{\hat{\mathbf{k}}_2,\alpha_2} \int_{-\omega_c}^{\omega_c} d\xi \frac{1}{2E_{\mathbf{k}_2,\alpha_2}}. \tag{2.100}$$

After performing the integral over ξ, the equation becomes

$$\varphi_{\hat{\mathbf{k}}_1,\alpha_1} = -\sum_{\alpha_2} \int_{S_{\alpha_2}} \frac{d\hat{\mathbf{k}}_2}{|S_{\alpha_2}|} g_{\hat{\mathbf{k}}_1,\alpha_1,d_0;\hat{\mathbf{k}}_2,\alpha_2,d_0} \varphi_{\hat{\mathbf{k}}_2,\alpha_2} \log\left(\frac{2\omega_c}{\Delta(0)|\tilde{\varphi}_{\hat{\mathbf{k}}_2,\alpha_2}|}\right) \tag{2.101}$$

where φ and $\tilde{\varphi}$ were defined in Section 2.5.2. We choose the normalization of $\tilde{\varphi}$ so that $\max_{\hat{\mathbf{k}},\alpha} |\tilde{\varphi}_{\hat{\mathbf{k}},\alpha}| = 1$. We now take the inner product with the same eigenvector φ and use the orthonormality of the eigenvectors of g to write

$$1 = -\lambda \sum_{\alpha_2} \int_{S_{\alpha_2}} \frac{d\hat{\mathbf{k}}_2}{|S_{\alpha_2}|} |\varphi_{\hat{\mathbf{k}}_2,\alpha_2}|^2 \log\left(\frac{2\omega_c}{\Delta(0)|\tilde{\varphi}_{\hat{\mathbf{k}}_2,\alpha_2}|}\right). \tag{2.102}$$

After rearranging terms, we finally find

$$\Delta(0) = 2\omega_c \exp\left(\frac{1}{\lambda}\right) \exp\left(-\langle \log(|\tilde{\varphi}|)\rangle\right) \tag{2.103}$$

with

$$\langle \log(|\tilde{\varphi}|)\rangle = \sum_{\alpha} \int_{S_\alpha} \frac{d\hat{\mathbf{k}}}{|S_\alpha|} |\varphi_{\hat{\mathbf{k}},\alpha}|^2 \log(|\tilde{\varphi}_{\hat{\mathbf{k}},\alpha}|). \tag{2.104}$$

We can then divide by T_c to obtain

$$\frac{2\Delta(0)}{T_c} = 3.53 \ \exp\left(-\langle \log(|\tilde{\varphi}|)\rangle\right) \geq 3.53 \tag{2.105}$$

where 3.53 is the well known BCS value for a uniform gap, and the exponential factor departs from 1 for non-uniform gaps.

2.7.2 Triplet

In the pseudo-spin triplet case, the $\mathcal{H}$ matrix is in general given by

$$\mathcal{H}_{\mathbf{k},\alpha} = \begin{pmatrix} \xi_{\mathbf{k},\alpha} & 0 & -\Delta_{\mathbf{k},\alpha,d_x} + i\Delta_{\mathbf{k},\alpha,d_y} & \Delta_{\mathbf{k},\alpha,d_z} \\ 0 & \xi_{\mathbf{k},\alpha} & \Delta_{\mathbf{k},\alpha,d_z} & \Delta_{\mathbf{k},\alpha,d_x} + i\Delta_{\mathbf{k},\alpha,d_y} \\ -\overline{\Delta}_{\mathbf{k},\alpha,d_x} - i\overline{\Delta}_{\mathbf{k},\alpha,d_y} & \overline{\Delta}_{\mathbf{k},\alpha,d_z} & -\xi_{\mathbf{k},\alpha} & 0 \\ \overline{\Delta}_{\mathbf{k},\alpha,d_z} & \overline{\Delta}_{\mathbf{k},\alpha,d_x} - i\overline{\Delta}_{\mathbf{k},\alpha,d_y} & 0 & -\xi_{\mathbf{k},\alpha} \end{pmatrix}. \tag{2.106}$$

In the following, we will sometimes use the convenient notation $\vec{d} = \Delta_{d_x}\hat{x} + \Delta_{d_y}\hat{y} + \Delta_{d_z}\hat{z}$, where the dependence on $\mathbf{k}, \alpha$ is implicit.

As mentioned before, due to a mirror symmetry present in Sr_2RuO_4, $\vec{d}$ will always be pointing either out-of-plane ($d_x = d_y = 0$) or in-plane ($d_z = 0$). These states can be called equal-pseudo-spin paired, in analogy with the equal-spin-paired (ESP) states described in Ref. [27].

Let us treat the case of out-of-plane $\vec{d}$ first. Posing $\Delta_{\mathbf{k},\alpha,d_z} \equiv \Delta_{\mathbf{k},\alpha}$, the matrix reads

$$\mathcal{H}_{\mathbf{k},\alpha} = \begin{pmatrix} \xi_{\mathbf{k},\alpha} & 0 & 0 & \Delta_{\mathbf{k},\alpha} \\ 0 & \xi_{\mathbf{k},\alpha} & \Delta_{\mathbf{k},\alpha} & 0 \\ 0 & \overline{\Delta}_{\mathbf{k},\alpha} & -\xi_{\mathbf{k},\alpha} & 0 \\ \overline{\Delta}_{\mathbf{k},\alpha} & 0 & 0 & -\xi_{\mathbf{k},\alpha} \end{pmatrix}. \tag{2.107}$$

It is easily checked that the two blocks lead to the same term in the Hamiltonian. Following the same calculation as for the singlet, we obtain the exact same Hamiltonian as in Eq. 2.112, the same gap equation as in Eq. 2.98, and the same formula for $\Delta(0)$, with d_0 replaced by d_z.

Let us now treat the in-plane $\vec{d}$ case. Once $\vec{d}$ can take different orientations as a function of momentum, one should distinguish between unitary and non-unitary states. A unitary state is such that $\vec{d} \times \vec{d}^* = 0$, a condition which ensures that the state does not have any imbalance between the two (pseudo-)spin species. At zero magnetic field, unitary states are therefore always expected to be favoured over non-unitary ones. For a unitary state with in-plane $\vec{d}$, it is easy to see that one can in full

generality always choose a real $\vec{d}$. Posing $\Delta_{\mathbf{k},\alpha} = -\Delta_{\mathbf{k},\alpha,d_x} + i\Delta_{\mathbf{k},\alpha,d_y}$, the Hamiltonian matrix becomes

$$\mathcal{H}_{\mathbf{k},\alpha} = \begin{pmatrix} \xi_{\mathbf{k},\alpha} & 0 & \Delta_{\mathbf{k},\alpha} & 0 \\ 0 & \xi_{\mathbf{k},\alpha} & 0 & -\overline{\Delta}_{\mathbf{k},\alpha} \\ \overline{\Delta}_{\mathbf{k},\alpha} & 0 & -\xi_{\mathbf{k},\alpha} & 0 \\ 0 & -\Delta_{\mathbf{k},\alpha} & 0 & -\xi_{\mathbf{k},\alpha} \end{pmatrix}. \tag{2.108}$$

This time the two blocks lead to two different contributions to the Hamiltonian that are related to each other by time-reversal symmetry.

The Bogolyubov transformation can be written as

$$\begin{aligned} c^\dagger_{\mathbf{k},\sigma} &= v'_{\mathbf{k},\sigma} a^\dagger_{\mathbf{k},\sigma} + v^*_{\mathbf{k},\sigma} b_{\mathbf{k},\sigma} \\ c^\dagger_{-\mathbf{k},\sigma} &= v'_{\mathbf{k},\sigma} b^\dagger_{\mathbf{k},\sigma} - v^*_{\mathbf{k},\sigma} a_{\mathbf{k},\sigma} \end{aligned} \tag{2.109}$$

with

$$\begin{aligned} v'_{\mathbf{k},\sigma} &= ie^{-i\phi_{\mathbf{k},\sigma}/2}\cos(\theta_{\mathbf{k},\sigma}) \\ v_{\mathbf{k},\sigma} &= -ie^{i\phi_{\mathbf{k},\sigma}/2}\sin(\theta_{\mathbf{k},\sigma}) \\ \cot(2\theta_{\mathbf{k},\sigma}) &= \frac{\xi_{\mathbf{k}}}{|\Delta_{\mathbf{k},\sigma}|} \end{aligned} \tag{2.110}$$

where $\Delta_{\mathbf{k},\sigma} = |\Delta_{\mathbf{k},\sigma}|e^{i\phi_{\mathbf{k},\sigma}}$, $\Delta_{\mathbf{k},+} = \Delta_{\mathbf{k}}$ and $\Delta_{\mathbf{k},-} = -\overline{\Delta}_{\mathbf{k}}$. We also give the inverse transformation for later convenience:

$$\begin{aligned} a^\dagger_{\mathbf{k},\sigma} &= (v'_{\mathbf{k},\sigma})^* c^\dagger_{\mathbf{k},\sigma} - v^*_{\mathbf{k},\sigma} c_{-\mathbf{k},\sigma} \\ b^\dagger_{\mathbf{k},\sigma} &= (v'_{\mathbf{k},\sigma})^* c^\dagger_{-\mathbf{k},\sigma} + v^*_{\mathbf{k},\sigma} c_{\mathbf{k},\sigma} \end{aligned} \tag{2.111}$$

with $a^\dagger_{-\mathbf{k},\sigma} = b^\dagger_{\mathbf{k},\sigma}$. Note that the band indices are implicit in all these expressions.

After this Bogolyubov transformation, the Hamiltonian reads

$$\begin{aligned} H_{BCS} &= \frac{1}{2}\sum_{\mathbf{k},\alpha} E_{\mathbf{k},\alpha}(a^\dagger_{\mathbf{k},\alpha,+}a_{\mathbf{k},\alpha,+} + b^\dagger_{\mathbf{k},\alpha,+}b_{\mathbf{k},\alpha,+} + a^\dagger_{\mathbf{k},\alpha,-}a_{\mathbf{k},\alpha,-} + b^\dagger_{\mathbf{k},\alpha,-}b_{\mathbf{k},\alpha,-}) \\ &= \sum_{\mathbf{k},\alpha} E_{\mathbf{k},\alpha}(a^\dagger_{\mathbf{k},\alpha,+}a_{\mathbf{k},\alpha,+} + a^\dagger_{\mathbf{k},\alpha,-}a_{\mathbf{k},\alpha,-}) \end{aligned} \tag{2.112}$$

where $E_{\mathbf{k},\alpha} = \sqrt{\xi^2_{\mathbf{k},\alpha} + |\Delta_{\mathbf{k},\alpha,+}|^2} = \sqrt{\xi^2_{\mathbf{k},\alpha} + |\Delta_{\mathbf{k},\alpha,-}|^2}$ and where we omitted the addi-

tive constant $\sum_{\mathbf{k},\alpha}(\xi_{\mathbf{k},\alpha} - E_{\mathbf{k},\alpha}) + \overline{\Delta}(V^{BCS})^{-1}\Delta$. The gap equation is again obtained by imposing self-consistency:

$$\begin{aligned}
\Delta_{\mathbf{k}_1,\alpha_1,d_a} &= \frac{1}{\sqrt{2}} \sum_{\mathbf{k}_2,\alpha_2,d_b} V^{BCS}_{\mathbf{k}_1,\alpha_1,d_a;\mathbf{k}_2,\alpha_2,d_b} \langle \phi_{\mathbf{k}_2,\alpha_2,d_b} \rangle \\
&= \frac{1}{\sqrt{2}} \sum_{\mathbf{k}_2,\alpha_2,d_b} V^{BCS}_{\mathbf{k}_1,\alpha_1,d_a;\mathbf{k}_2,\alpha_2,d_b} (\sum_{\sigma} U_{d_b,\sigma\sigma} \langle \phi_{\mathbf{k}_2,\alpha_2,\sigma\sigma} \rangle) \\
&= \frac{1}{\sqrt{2}} \sum_{\mathbf{k}_2,\alpha_2,d_b} V^{BCS}_{\mathbf{k}_1,\alpha_1,d_a;\mathbf{k}_2,\alpha_2,d_b} (\sum_{\sigma} U_{d_b,\sigma\sigma} (v'_{\mathbf{k}_2,\alpha_2,\sigma})^* v_{\mathbf{k}_2,\alpha_2,\sigma} (1 - 2n(E_{\mathbf{k}_2,\alpha_2}))) \\
&= - \sum_{\mathbf{k}_2,\alpha_2,d_b} V^{BCS}_{\mathbf{k}_1,\alpha_1,d_a;\mathbf{k}_2,\alpha_2,d_b} (\sum_{\sigma} U_{d_b,\sigma\sigma} \Delta_{\mathbf{k}_2,\alpha_2,\sigma,\sigma}) \frac{\tanh(E_{\mathbf{k}_2,\alpha_2}/2T)}{2E_{\mathbf{k}_2,\alpha_2}} \\
&= - \sum_{\mathbf{k}_2,\alpha_2,d_b} V^{BCS}_{\mathbf{k}_1,\alpha_1,d_a;\mathbf{k}_2,\alpha_2,d_b} \Delta_{\mathbf{k}_2,\alpha_2,d_b} \frac{\tanh(E_{\mathbf{k}_2,\alpha_2}/2T)}{2E_{\mathbf{k}_2,\alpha_2}}
\end{aligned} \tag{2.113}$$

where U is the unitary matrix for the change of basis from $\{(\sigma\sigma') = (++), (--)\}$ to $\{d_a = d_x, d_y\}$.

The equation for $\Delta(0)$ is the same as in the singlet case:

$$\Delta(0) = 2\omega_c \exp\left(\frac{1}{\lambda}\right) \exp\left(-\langle \log(|\tilde{\varphi}|) \rangle\right) \tag{2.114}$$

but with a generalized version of $\langle \log(|\tilde{\varphi}|) \rangle$:

$$\langle \log(|\tilde{\varphi}|) \rangle = \sum_{\alpha} \int_{S_\alpha} \frac{d\hat{\mathbf{k}}}{|S_\alpha|} \left(|\varphi_{\hat{\mathbf{k}},\alpha,d_x}|^2 + |\varphi_{\hat{\mathbf{k}},\alpha,d_y}|^2 \right) \log\left(\sqrt{|\tilde{\varphi}_{\hat{\mathbf{k}},\alpha,d_x}|^2 + |\tilde{\varphi}_{\hat{\mathbf{k}},\alpha,d_y}|^2} \right). \tag{2.115}$$

2.7.3 Specific heat jump

BCS theory predicts a jump in specific heat ΔC at T_c. The ratio of ΔC to its value in the normal state C_n is a number which, for a clean superconductor in the weak coupling limit, depends only on the momentum-space anisotropy of the gap. For a gap norm given at the Fermi surface by $|\Delta_{\hat{\mathbf{k}},\alpha}| = \Delta |f_{\hat{\mathbf{k}},\alpha}|$, where Δ is a positive

constant, this ratio is given by [102, 103]

$$\frac{\Delta C}{C_n}(T_c) = \frac{12}{7\zeta(3)} \frac{\left\langle |f_{\hat{\mathbf{k}},\alpha}|^2 \right\rangle_{\mathrm{FS}}^2}{\left\langle |f_{\hat{\mathbf{k}},\alpha}|^4 \right\rangle_{\mathrm{FS}}} \tag{2.116}$$

where

$$\langle h_{\mathbf{k},\alpha} \rangle_{\mathrm{FS}} = \frac{1}{\rho} \sum_{\alpha} \int_{\mathrm{FS}_\alpha} \frac{d\hat{\mathbf{k}}}{(2\pi)^D} \frac{1}{v_{\mathbf{k},\alpha}} h_{\mathbf{k},\alpha}, \tag{2.117}$$

where $\frac{12}{7\zeta(3)} \simeq 1.43$, where ρ is the total density of states at the Fermi level and where

$$|f_{\hat{\mathbf{k}},\alpha}| = \sqrt{\sum_{d_\mu} |\tilde{\varphi}_{\mathbf{k},\alpha,d_\mu}|^2}. \tag{2.118}$$

One can easily insert the gap functions predicted in the previous sections in this formula to obtain a prediction for $\frac{\Delta C}{C_n}$ and compare it with experiments. This will be used in Chapter 3 for the case of Sr_2RuO_4.

2.8 Conclusion

We give here a summary of the main results established in this Chapter. Given a multi-orbital hopping model describing a metal and an interaction Hamiltonian, one can study the onset of superconductivity in the infinitely small interaction limit by the following procedure. First, diagonalize the single-particle Hamiltonian, define a momentum-dependent pseudo-spin basis if spin-orbit coupling is present, and locate the Fermi surfaces for the different bands, $\{\hat{\mathbf{k}}, \alpha\}$. Second, compute and diagonalize the pairing matrix $g_{\hat{\mathbf{k}}_1,\alpha_1,d_{\mu_1};\hat{\mathbf{k}}_2,\alpha_2,d_{\mu_2}}$, where d_0 gives the pseudo-spin singlet sector, and $d_{x,y,z}$ give the pseudo-spin triplet sector. The eigenequation is given by

$$\sum_{\alpha} \sum_{d_\mu} \int_{S_\alpha} \frac{d\hat{\mathbf{k}}}{|S_\alpha|} g_{\hat{\mathbf{k}}_1,\alpha_1,d_{\mu_1};\hat{\mathbf{k}},\alpha,d_\mu} \varphi_{\hat{\mathbf{k}},\alpha,d_\mu} = \lambda \, \varphi_{\hat{\mathbf{k}}_1,\alpha_1,d_{\mu_1}}. \tag{2.119}$$

The pairing matrix is directly related to the 2-particle irreducible effective vertex in the Cooper channel calculated at leading order in U/t:

$$g_{\hat{\mathbf{k}}_1,\alpha_1,d_{\mu_1};\hat{\mathbf{k}}_2,\alpha_2,d_{\mu_2}} \equiv \sqrt{\rho_{\alpha_1}\frac{\overline{v}_{\alpha_1}}{v_{\hat{\mathbf{k}}_1,\alpha_1}}}\Gamma_{\hat{\mathbf{k}}_1,\alpha_1,d_{\mu_1};\hat{\mathbf{k}}_2,\alpha_2,d_{\mu_2}}\sqrt{\rho_{\alpha_2}\frac{\overline{v}_{\alpha_2}}{v_{\hat{\mathbf{k}}_2,\alpha_2}}}. \tag{2.120}$$

After discretization of the Fermi surfaces, $\hat{\mathbf{k}}_1$ and $\hat{\mathbf{k}}_2$ only take a finite number of values, and g becomes a hermitian matrix that is easily diagonalized numerically. The most negative eigenvalue λ gives the most favored superconducting order parameter, with a critical temperature given by $T_c \propto e^{1/\lambda}$ and an order parameter functional form given by the corresponding eigenvector. One can then study the superconducting phase by using a BCS mean-field Hamiltonian where the gap functional form is assumed independent of T.

2.8.1 Range of validity

The discussion in this Chapter is valid as long as the non-interacting particle-hole susceptibility χ^{ph} is non-divergent. If χ^{ph} diverges, instabilities different from BCS can appear even in the weak coupling limit and the assumption of BCS being the only instability therefore breaks down. This is always the case in one dimension, where χ has a divergence at $2k_F$ because of the perfect nesting of the Fermi surface given by two points at $\pm k_F$. In this case, there is competition between the BCS instability and the charge-density wave instability. They actually exactly cancel each other so that fermions in 1D form a Luttinger liquid that remains gapless even in the presence of interactions [90, 104, 105]. A divergent non-interacting particle-hole susceptibility can also occur in 2D at a Van Hove singularity [106], but requires fine-tuning of the hoppings and of the electron density. A Van Hove singularity is a divergence of the density of states that arises when the chemical potential goes through an extremum or a saddle-point of the dispersion relation. We will discuss the evolution of the superconducting state in Sr_2RuO_4 across such as a Van Hove singularity in Chapter 5. While for a strictly two-dimensional system the weak coupling analysis breaks

down strictly at the Van Hove point, it is still valid arbitrarily close to it, as long as the interaction is small enough. Furthermore, if one actually takes into account the inter-layer coupling in Sr_2RuO_4 , one obtains a 3D system for which the density of states does not diverge at a Van Hove point (only its derivative does)[106].

3. Application to Sr_2RuO_4

3.1 Introduction

First let us summarise the two open questions about Sr_2RuO_4 that will be discussed in this chapter. More background about these questions can be found in Chapter 1. Strontium ruthenate [1, 25, 43] is a layered perovskite material exhibiting a transition at 1.5 K from a Fermi liquid to a superconducting phase. Strong experimental evidence points towards an odd-parity order parameter (OP) [67, 68, 70, 76]. Based on multiple experiments[74–76, 107–109], the prevailing candidate for the symmetry of the OP has been the chiral p-wave state, $\vec{d} = (p_x \pm ip_y)\hat{\mathbf{z}}$, which breaks time-reversal symmetry (TRS), hosts topologically protected chiral edge states and is analogous to superfluid ^{3}He-A [14, 15].

On the other hand, this state is supposed to carry edge currents at sample edges and domain walls, which have been elusive so far despite intense scrutiny (these edge currents will be discussed in Chapter 4)[80, 81]. As a result, other OP symmetries have been considered theoretically [26, 110–112], including the helical states, $\vec{d} = p_x\hat{x} \pm p_y\hat{y}$ and $\vec{d} = p_y\hat{x} \pm p_x\hat{y}$. These phases can be viewed as time-reversal invariant versions of chiral superconductors. Their edges host two counter-propagating Majorana modes of opposite pseudo-spin whose net charge current is zero.

Another controversy exists regarding the band(s) on which the superconducting instability is dominant. The Fermi surface (FS) of Sr_2RuO_4 is made of three cylindrical sheets: The $\boldsymbol{\gamma}$ band is mainly derived from the Ru $4d_{xy}$ orbital and is fairly isotropic in the basal plane, while the $\boldsymbol{\alpha}$ and $\boldsymbol{\beta}$ bands are mainly derived from the Ru $4d_{xz}$ and $4d_{yz}$ orbitals and are quasi-one-dimensional (see Fig. 3.1).

The prevailing assumption in the field has been that $\boldsymbol{\gamma}$ is the active band. This assumption was based on specific heat data [65] and backed by several calculations[26, 52–55] that predicted a dominant gap on $\boldsymbol{\gamma}$ and a subdominant, near-nodal gap on

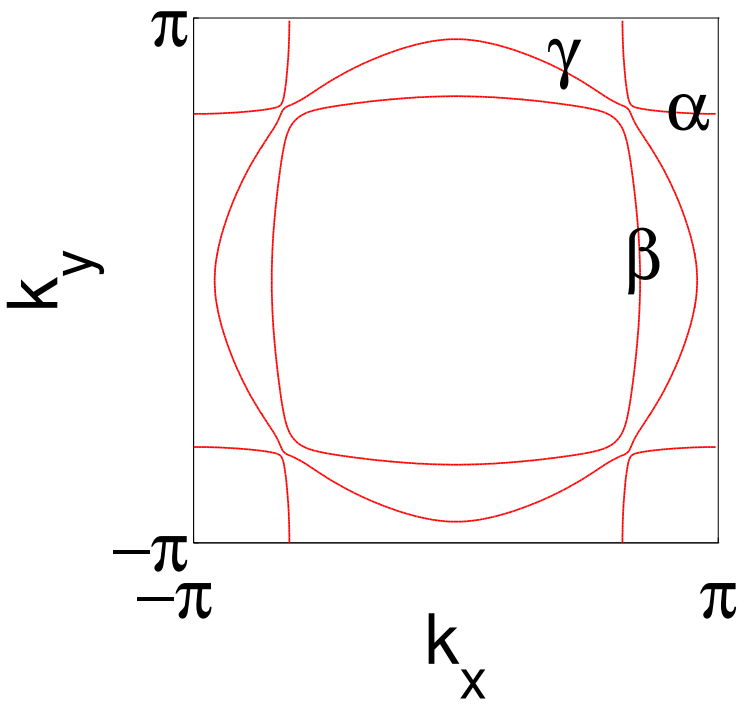

Figure 3.1: Fermi surfaces for the tight-binding model given in Eq. (3.1).

$\boldsymbol{\alpha}$ and $\boldsymbol{\beta}$. Since the $\boldsymbol{\gamma}$ band is fairly isotropic in the *ab* plane with a fairly large interaction-induced mass renormalization, it has been suggested that the system is a two-dimensional electronic analog of ^{3}He.

This scenario was challenged by various works. First, several calculations predicted a dominant gap on $\boldsymbol{\alpha}$ and $\boldsymbol{\beta}$ [56–63]. In particular, Raghu *et al.* [61](see also [62]) showed that, in absence of band coupling and in the weak-coupling limit, $\boldsymbol{\alpha}$ and $\boldsymbol{\beta}$ are the active bands. Second, Firmo *et al.* [9] reported a phenomenological model with a gap amplitude of similar size on the three bands but slightly larger on $\boldsymbol{\alpha}$ and $\boldsymbol{\beta}$ than on $\boldsymbol{\gamma}$ that is consistent with specific heat and scanning tunnelling microscopy (STM) measurements.

Since spin-orbit coupling is responsible for both the hybridization between the different sets of bands and for the splitting between the critical temperatures of chiral and helical states, it is highly desirable to perform a calculation where it is treated at a microscopic level, which was not the case in Refs. [9, 61]. The formalism developed in Chapter 2 is therefore particularly well-suited to address these questions. This

formalism enables us to study the orientation of $\vec{d}$ at a microscopic level and to determine the gap on the three bands. We find similarly sized gaps on the three bands without the necessity of fine-tuning. Depending on the interaction parameter, we find two order parameters that are compatible with the thermodynamic data: either a chiral gap whose amplitude is slightly larger on $\boldsymbol{\gamma}$, or a helical gap whose amplitude is slightly larger on $\boldsymbol{\alpha}$ and $\boldsymbol{\beta}$.

3.2 Model

3.2.1 Tight-binding

The first step is to obtain a Hamiltonian that reproduces the properties of the normal state above T_c, which is a well-studied Fermi liquid [113]. Density-functional theory (DFT) calculations for Sr_2RuO_4 [71, 72] predict the presence of three bands at the Fermi level whose wavefunctions have a high overlap with three Ruthenium atomic orbitals: $4d_{xz}$, $4d_{yz}$ and $4d_{xy}$. We therefore used a tight-binding Hamiltonian based on these three atomic orbitals.

The Ruthenium atoms form a body-centered tetragonal lattice with unit cell dimensions of $a = 0.3862$ nm in the ab plane and $c = 1.2722$ nm along the c direction (see Figure 1.1). Due to the high ratio of c/a, Sr_2RuO_4 is a highly anisotropic Fermi liquid, as evidenced by transport measurements [1] and the tiny Fermi surface dispersion along k_z (see Figure 1.3). We will therefore neglect the hoppings along the c direction altogether and consider a unique plane of Ruthenium oxide. Note that, within such a plane, the Ruthenium atoms form a square lattice. Based on this approach, the following tight-binding Hamiltonian for electrons hopping on a square lattice will be used[114, 115]

$$H_K = H_{\text{Hop}} + H_{\text{SOC}} = \sum_{\mathbf{k},s} \psi_s^\dagger(\mathbf{k}) h_s(\mathbf{k}) \psi_s(\mathbf{k}) \tag{3.1}$$

where $\psi_s(\mathbf{k}) = [c_{\mathbf{k},A,s}; c_{\mathbf{k},B,s}; c_{\mathbf{k},C,-s}]^T$ with $s = 1$ (-1) for up (down) spins. The matrix

$h_s(\mathbf{k})$ is given by

$$h_s(\mathbf{k}) = \begin{pmatrix} E_A(\mathbf{k}) & E_{AB}(\mathbf{k}) - si\eta & i\eta \\ E_{AB}(\mathbf{k}) + si\eta & E_B(\mathbf{k}) & -s\eta \\ -i\eta & -s\eta & E_C(\mathbf{k}) \end{pmatrix} \tag{3.2}$$

where

$$\begin{aligned} E_A(\mathbf{k}) &= -2t\cos(k_x) - 2t^{\perp}\cos(k_y) - \mu \\ E_B(\mathbf{k}) &= -2t^{\perp}\cos(k_x) - 2t\cos(k_y) - \mu \\ E_C(\mathbf{k}) &= -2t'(\cos(k_x) + \cos(k_y)) - 4t''\cos(k_x)\cos(k_y) - \mu_C \\ E_{AB}(\mathbf{k}) &= -4t'''\sin(k_x)\sin(k_y) \end{aligned} \tag{3.3}$$

and where A, B and C stand for the Ru orbitals $4d_{xz}$, $4d_{yz}$ and $4d_{xy}$ on each lattice site. The spin-orbit coupling (SOC) parameter is η and the interorbital hopping term is $E_{AB}(\mathbf{k})$.

As explained in Chapter 2, thanks to time-reversal and inversion symmetry, each band formed by the diagonalization of H_K is doubly-degenerate and can be indexed by a pseudo-spin σ:

$$H_K = \sum_{\mathbf{k},\alpha,\sigma} \xi_{\mathbf{k},\alpha} c^{\dagger}_{\mathbf{k},\alpha,\sigma} c_{\mathbf{k},\alpha,\sigma} \tag{3.4}$$

with $\sigma = 1$ (-1) for $+$ $(-)$ pseudospin and $\alpha = \boldsymbol{\alpha}, \boldsymbol{\beta}, \boldsymbol{\gamma}$. Note that we use bold symbols for the actual bands of Sr_2RuO_4, as opposed to the non-bold greek letters α and β which are used as generic band indices.

From the form of the Hamiltonian given in Eq. 3.2, one sees that H_K is block diagonal, where the two blocks are given by $[c_{\mathbf{k},A,\uparrow}; c_{\mathbf{k},B,\uparrow}; c_{\mathbf{k},C,\downarrow}]$ and $[c_{\mathbf{k},A,\downarrow}; c_{\mathbf{k},B,\downarrow}; c_{\mathbf{k},C,\uparrow}]$. This originates from an element of the double group (defined in Chapter 2): the mirror symmetry $z \to -z$ applied in both real and spin space. The action of this symmetry is given by the operator M_z which commutes with H_K and is given by

$$M_z c^{\dagger}_{\mathbf{k},a,s} M_z^{-1} = s(-1)^{\delta_{a,A}}(-1)^{\delta_{a,B}} c^{\dagger}_{\mathbf{k},a,s} \tag{3.5}$$

where $a = A, B, C$ is the orbital index, $\delta_{a,b}$ is 1 is $a = b$ and 0 otherwise, and where we

used the fact that, in our 2D model, we only use momenta $\mathbf{k}$ with $k_z = 0$. We also used the fact that the A ($4d_{xz}$) and B ($4d_{yz}$) orbitals are odd under this symmetry while the C orbital (d_{xy}) is even. The two blocks defined above are given by, respectively, the odd and even sectors of M_z. Given this symmetry, it is natural to assign pseudo-spin up $\sigma = +1$ to the block $[c_{\mathbf{k},A,\downarrow}; c_{\mathbf{k},B,\downarrow}; c_{\mathbf{k},C,\uparrow}]$ and pseudo-spin down $\sigma = -1$ to the block $[c_{\mathbf{k},A,\uparrow}; c_{\mathbf{k},B,\uparrow}; c_{\mathbf{k},C,\downarrow}]$. The $|\mathbf{k}, \alpha, \sigma\rangle$ basis is then defined up to a phase choice for each momentum $\mathbf{k}$. It was explained in Chapter 2 how to choose this phase appropriately across momentum space so that superconducting order parameters in pseudo-spin basis transform in the appropriate way under double group symmetry operations.

We now give a short comment on the origin of the form of the SOC term used in H_K. Spin-orbit coupling was treated in the approximation of a single Ruthenium atom within the environment of its neighbouring ligand Oxygen ions forming an octahedron (see Figure 1.1). These ions generate a so-called crystal field that splits the e_g doublet ($d_{x^2-y^2}$ and d_{z^2}) from the t_{2g} triplet (d_{xz}, d_{yz} and d_{xy}). Since, because of this crystal field, only the t_{2g} orbitals have a sizable weight at the Fermi level, we approximate the spin-orbit coupling term by:

$$H_{\text{SOC}} = 2\eta \sum_i P_{t_{2g}} \vec{L}_i \cdot \vec{S}_i \; P_{t_{2g}} \tag{3.6}$$

where i the Ru site index, the operator P gives the projection to the t_{2g} triplet, $\vec{L}$ is the orbital angular momentum and $\vec{S}$ is the spin angular momentum. After a Fourier transform, the spin-orbit coupling Hamiltonian becomes [114, 115]

$$H_{\text{SOC}} = i\eta \sum_{\mathbf{k}} \sum_{l,m,n} \epsilon_{lmn} \sum_{s,s'} \sigma^n_{ss'} c^\dagger_{\mathbf{k}ls} c_{\mathbf{k}ms'}$$

where l, m, n are orbital indices, s, s' are spin indices, σ^n is the n-th Pauli matrix and ϵ_{lmn} is the Levi-Civita symbol. The orbital indices are defined in the following way: $l = 1, 2, 3$ for, respectively, the orbital d_{yz} (B), d_{zx} (A) and d_{xy} (C).

When choosing the parameters of this model, several quantities should be fitted to target values, the most important ones being the shape of the Fermi surfaces and

the effective masses of each band. When choosing the target values, one can use the value coming from experiments, or coming from DFT. While there is a good agreement between the two in the case of the shape of the Fermi surfaces, this is not the case for the effective masses because of strong correlation effects [116].

There are two possible approaches to this problem. The first one is to use a hopping model whose bare masses are the ones from DFT, and to add some finite interaction whose value will be fitted so that the renormalised mass will be the one from experiments. One then needs an approximation that deals with the finite interaction, like dynamical mean-field theory (DMFT) [116] or the random phase approximation (RPA)[117].

The second one is to use a hopping model whose bare masses are already the experimental ones and to add only a vanishingly small interaction. In the limit of vanishing interaction, the band masses will stay at their bare values, which are already the experimental ones. Since the BCS instability occurs even at vanishingly small interaction, it is possible to study superconductivity even in a model with such a small interaction. This is the method used in this thesis. The parameters were therefore chosen so as to reproduce the shape of the Fermi surfaces and so that the Fermi level density of states of the different bands are consistent with the measured effective quasiparticle masses [1, 118]: In dimensionless units, $(t, t^{\perp}, t', t'', \mu, \mu_C, t''', \eta) = (1.0, 0.1, 0.8, 0.3, 1.0, 1.1, 0.01, 0.1)$. With these parameters, the relative contribution to the Fermi level density of states in our hopping model is given by

$$\begin{aligned} \frac{\rho_{\boldsymbol{\alpha}}}{\rho} &\simeq 0.16 \\ \frac{\rho_{\boldsymbol{\beta}}}{\rho} &\simeq 0.30 \\ \frac{\rho_{\boldsymbol{\gamma}}}{\rho} &\simeq 0.54 \end{aligned} \tag{3.7}$$

where $\rho = \rho_{\boldsymbol{\alpha}} + \rho_{\boldsymbol{\beta}} + \rho_{\boldsymbol{\gamma}}$ is the total density of states at the Fermi level. In order to reproduce the measured quasiparticle masses, one should use $t \sim 0.2$ eV [114]. As explained in Section 5.3, in the weak coupling limit, this overall scale for t only enters the problem through an overall factor $(U/t)^2$ for the pairing matrix g defined

in Chapter 2. One can therefore use $t = 1$ throughout the calculation and add this factor of $(U/t)^2$ in front of the pairing eigenvalue in the formula for T_c at the end of the calculation.

Note that this scheme obviously neglects an important part of the strongly correlated Fermi liquid: by modelling the normal state by a free fermion gas with a bare mass given by the experimental mass, we neglect the imaginary part of the self-energy which gives the finite lifetime of quasiparticles, and the renormalization constant Z being smaller than 1 [97].

3.2.2 Interactions

The second step is to write down the interaction Hamiltonian. Since our tight-binding model reproduces the dispersion of the renormalised quasiparticles close to the Fermi level, the interaction should be the one sensed by these quasiparticles. Since computing this interaction explicitly is in general not possible, we will use a phenomenological approach. Due to screening, the interaction decays exponentially with distance, and is expected to be sizable only over a few lattice sites. Following Hubbard [94], we only keep the on-site interaction term as it is expected to capture the correct qualitative behaviour. Furthermore, we neglect the orbital anisotropy due to the ions neighboring each Ruthenium atom, and write the interaction as if the Ruthenium atom was isolated (this approximation could be easily lifted but it would lead to more parameters, with for example a different value of U for the d_{xy} orbital and the d_{zx}, d_{zy} orbitals). The projection of the screened interaction to the t_{2g} orbitals can then be expressed in terms of two phenomological parameters, U and J:

$$\begin{aligned} H_I = &\sum_{i,a,s\neq s'} \frac{U}{2} n_{ias} n_{ias'} + \sum_{i,a\neq b,s,s'} \frac{U'}{2} n_{ias} n_{ibs'} \\ &+ \sum_{i,a\neq b,s,s'} \frac{J}{2} c^\dagger_{ias} c^\dagger_{ibs'} c_{ias'} c_{ibs} + \sum_{i,a\neq b,s\neq s'} \frac{J'}{2} c^\dagger_{ias} c^\dagger_{ias'} c_{ibs'} c_{ibs} \end{aligned} \tag{3.8}$$

where i is the site index, $a = A, B, C$ is the orbital index, $\overline{s} \equiv -s$, $n_{ias} \equiv c^\dagger_{ias} c_{ias}$, $U' = U - 2J$, and $J' = J$ [95]. This Hamiltonian can be rewritten as the generic

multi-orbital Hubbard model studied in Chapter 2,

$$H_I = \frac{1}{4} \sum_{\mathbf{k}_1+\mathbf{k}_2=\mathbf{k}_3+\mathbf{k}_4} \sum_{a_i,s_i} V_{a_1,s_1,a_2,s_2;a_3,s_3,a_4,s_4}\ c^\dagger_{\mathbf{k}_1,a_1,s_1} c^\dagger_{\mathbf{k}_2,a_2,s_2} c_{\mathbf{k}_3,a_3,s_3} c_{\mathbf{k}_4,a_4,s_4} \tag{3.9}$$

by choosing

$$\begin{aligned} V_{a_1,s_1,a_2,s_2;a_3,s_3,a_4,s_4} &= U\delta_{a_1,a_2}\delta_{a_2,a_3}\delta_{a_3,a_4}\delta_{s_1,-s_2}\delta_{s_3,-s_4}(\delta_{s_2,s_3} - \delta_{s_2,s_4}) \\ &+ U'(1-\delta_{a_1,a_2})(\delta_{a_1,a_4}\delta_{s_1,s_4}\delta_{a_2,a_3}\delta_{s_2,s_3} - \delta_{a_1,a_3}\delta_{s_1,s_3}\delta_{a_2,a_4}\delta_{s_2,s_4}) \\ &+ J(1-\delta_{a_1,a_2})(\delta_{a_1,a_3}\delta_{s_1,s_4}\delta_{a_2,a_4}\delta_{s_2,s_3} - \delta_{a_1,a_4}\delta_{s_1,s_3}\delta_{a_2,a_3}\delta_{s_2,s_4}) \\ &+ J'(1-\delta_{a_2,a_3})\delta_{s_1,-s_2}\delta_{a_1,a_2}\delta_{a_3,a_4}(\delta_{s_2,s_3}\delta_{s_1,s_4} - \delta_{s_2,s_4}\delta_{s_1,s_3}). \end{aligned} \tag{3.10}$$

where $\delta_{i,j}$ is 1 if $i = j$ and 0 otherwise.

We can now rewrite the entire Hamiltonian $H = H_K + H_I$ in the band and pseudo-spin basis:

$$\begin{aligned} H = H_K + H_I &= \sum_{\mathbf{k}} \xi_{\mathbf{k},\alpha}(c^\dagger_{\mathbf{k},\alpha,\sigma=+1} c_{\mathbf{k},\alpha,\sigma=+1} + c^\dagger_{\mathbf{k},\alpha,\sigma=-1} c_{\mathbf{k},\alpha,\sigma=-1}) \\ &+ \frac{1}{4} \sum_{\mathbf{k}_1+\mathbf{k}_2=\mathbf{k}_3+\mathbf{k}_4} \sum_{\alpha_i,\sigma_i} V_{\mathbf{k}_1,\alpha_1,\sigma_1,\mathbf{k}_2,\alpha_2,\sigma_2;\mathbf{k}_3,\alpha_3,\sigma_3,\mathbf{k}_4,\alpha_4,\sigma_4} c^\dagger_{\mathbf{k}_1,\alpha_1,\sigma_1} c^\dagger_{\mathbf{k}_2,\alpha_2,\sigma_2} c_{\mathbf{k}_3,\alpha_3,\sigma_3} c_{\mathbf{k}_4,\alpha_4,\sigma_4} \end{aligned} \tag{3.11}$$

where

$$\begin{aligned} &V_{\mathbf{k}_1,\alpha_1,\sigma_1,\mathbf{k}_2,\alpha_2,\sigma_2;\mathbf{k}_3,\alpha_3,\sigma_3,\mathbf{k}_4,\alpha_4,\sigma_4} = \\ &\sum_{a_i,s_i} V_{a_1,s_1,a_2,s_2;a_3,s_3,a_4,s_4}\ u^{\alpha_1,\sigma_1}_{a_1,s_1}(\mathbf{k}_1)\ u^{\alpha_2,\sigma_2}_{a_2,s_2}(\mathbf{k}_2)\ (u^{\alpha_3,\sigma_3}_{a_3,s_3}(\mathbf{k}_3))^*\ (u^{\alpha_4,\sigma_4}_{a_4,s_4}(\mathbf{k}_4))^* \end{aligned} \tag{3.12}$$

and

$$c^\dagger_{\mathbf{k},\alpha,\sigma} = \sum_{a,s} u^{\alpha,\sigma}_{a,s}(\mathbf{k}) c^\dagger_{\mathbf{k},a,s}. \tag{3.13}$$

Using the fact that $[H_I, M_z] = 0$ and that

$$M_z c^\dagger_{\mathbf{k},\alpha,\sigma} M_z^{-1} = \sigma c^\dagger_{\mathbf{k},\alpha,\sigma}, \tag{3.14}$$

one finds that $V_{\mathbf{k}_1,\alpha_1,\sigma_1,\mathbf{k}_2,\alpha_2,\sigma_2;\mathbf{k}_3,\alpha_3,\sigma_3,\mathbf{k}_4,\alpha_4,\sigma_4}$ is non-zero only if $\sigma_1\sigma_2\sigma_3\sigma_4 = 1$. In the

basis $\sigma_1, \sigma_2 = [+-, -+, ++, --]$, V is thus given by the following matrix:

$$\begin{pmatrix} V_{+-;+-} & V_{+-;-+} & 0 & 0 \\ V_{-+;+-} & V_{-+;-+} & 0 & 0 \\ 0 & 0 & V_{++;++} & V_{++;--} \\ 0 & 0 & V_{--;++} & V_{--;--} \end{pmatrix} \tag{3.15}$$

where the $\mathbf{k}, \alpha$ indices were left implicit. This means that the interaction conserves total pseudo-spin modulo 4, which was used in Chapter 2 to show that the helical and chiral sectors are decoupled.

3.3 Weak coupling analysis

Following the formalism developed in Chapter 2, we treat the weak-coupling limit, which corresponds to $U, J \ll t$ where J/U is a finite constant that fully parametrises the interaction. Although this method is exact in the vanishing interaction limit, all real systems have finite interaction strengths and one is therefore forced to extrapolate this technique's results out of its strict regime of validity in order to make a link with experiments. We will discuss the potential shortcomings of such an extrapolation in Section 5.2.

We remind the reader of the main results of Chapter 2, with a simplified notation that leaves spin indices implicit for now. The eigenmodes of the effective interaction in the Cooper channel are solutions of

$$\sum_\beta \int_{S_\beta} \frac{d\mathbf{q}_\beta}{|S_\beta|} g_{\mathbf{k}_\alpha, \mathbf{q}_\beta} \varphi_{\mathbf{q}_\beta} = \lambda \, \varphi_{\mathbf{k}_\alpha} \tag{3.16}$$

where

$$g_{\mathbf{k}_\alpha, \mathbf{q}_\beta} = \sqrt{\rho_\alpha \frac{\overline{v_\alpha}}{v_{\mathbf{k}_\alpha}}} \Gamma_{\mathbf{k}_\alpha, \mathbf{q}_\beta} \sqrt{\rho_\beta \frac{\overline{v_\beta}}{v_{\mathbf{q}_\beta}}}, \tag{3.17}$$

and where $\Gamma_{\mathbf{k}_\alpha, \mathbf{q}_\beta}$ is the two-particle irreducible vertex in the Cooper channel calculated at one-loop order, S_α is the Fermi surface of band α, $|S_\alpha|$ its area, ρ_α is the

density of states (DOS) of the band α at the Fermi level, $v_{\mathbf{k}_\alpha}$ is the Fermi velocity of band α and $\overline{v_\alpha}$ its average. Since $\mathbf{k}_\alpha$ and $\mathbf{q}_\beta$ are constrained to lie on their respective FS, Eq. (3.16) is solved in matrix form once the FSs are discretized.

The superconducting instability happens at a critical temperature given by

$$T_c = \mathcal{W} \exp\left(-\frac{1}{|\lambda|}\right) \tag{3.18}$$

where λ is the most negative eigenvalue of g and $\mathcal{W}$ is of the order of the bandwidth. The gap is proportional to the corresponding eigenvector:

$$\Delta_{\mathbf{k}_\alpha} \propto \sqrt{\frac{v_{\mathbf{k}_\alpha}}{\overline{v_\alpha}\rho_\alpha}}\varphi_{\mathbf{k}_\alpha}. \tag{3.19}$$

As explained in Chapter 2, the pseudospin dependence of the order parameter is advantageously written as:

$$\Delta_{\mathbf{k}_\alpha} = \begin{pmatrix} \Delta_{++} & \Delta_{+-} \\ \Delta_{-+} & \Delta_{--} \end{pmatrix}_{\mathbf{k}_\alpha} = \begin{pmatrix} -d_x + id_y & d_z + \Delta_s \\ d_z - \Delta_s & d_x + id_y \end{pmatrix}_{\mathbf{k}_\alpha}, \tag{3.20}$$

which defines a scalar order parameter Δ_s for the singlet case and a vectorial order parameter $\vec{d}$ for the triplet case. Since they are respectively even and odd under inversion, these two cases are mutually exclusive.

As explained in Chapter 2, thanks to a convenient choice of pseudo-spin basis, the pseudo-spin $\vec{d}$ transforms like a vector under the point group symmetry transformations as long as they are performed simultaneously in real and spin space. Since Sr_2RuO_4 is tetragonal, $\vec{d}$ has to be in a given irreducible representation of D_{4h}. As shown in Table 3.1, the odd-parity representations can be split into two groups: the chiral state $\vec{d} = (p_x \pm ip_y)\hat{z}$ and the helical states $\vec{d} = p_x\hat{x} \pm p_y\hat{y}$ and $\vec{d} = p_y\hat{x} \pm p_x\hat{y}$. The symbols $p_{x,y}$ stand for any function of momentum that has the same properties as $\sin(k_{x,y})$ under the symmetry operations of D_{4h}. The unit vectors $\hat{x}$, $\hat{y}$, and $\hat{z}$ are along the directions a, b, and c.

Γ	$\vec{d}(\mathbf{k})$	Dimension	TRSB	Type	^{3}He phase
A_{1u}	$\hat{x}p_x + \hat{y}p_y$	1	No	Helical	BW
A_{2u}	$\hat{x}p_y - \hat{y}p_x$	1	No	Helical	
B_{1u}	$\hat{x}p_x - \hat{y}p_y$	1	No	Helical	
B_{2u}	$\hat{x}p_y + \hat{y}p_x$	1	No	Helical	
E_u	$\hat{z}(p_x \pm ip_y)$	2	Yes	Chiral	ABM

Table 3.1: Odd-parity irreducible representations of D_{4h}, from Ref. [12]. TRSB stands for Time Reversal Symmetry Breaking. BW (ABM) stands for the Balian - Werthamer[13] (Anderson - Brinkman - Morel[14, 15]) phase of superfluid ^{3}He. Note that components odd under $k_z \to -k_z$ were not included in the $\vec{d}(\mathbf{k})$ column, as they would correspond to inter-plane components of the pairing, which are expected to be strongly disfavored due to the highly two-dimensional character of Sr_2RuO_4.

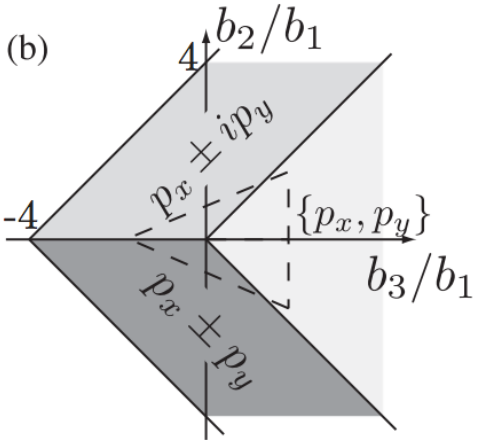

Figure 3.2: Phase diagram for the Ginzburg-Landau functional given in the text. The $\{p_x, p_y\}$ phase corresponds to $(\eta_x, \eta_y) = (1, 0)$ or $(\eta_x, \eta_y) = (0, 1)$. The $p_x \pm ip_y$ phase corresponds to $(\eta_x, \eta_y) = (1, \pm i)$. The $p_x \pm p_y$ phase corresponds to $(\eta_x, \eta_y) = (1, \pm 1)$. The white region is out of the stability domain. The dashed triangle is not relevant to the present discussion. Reprinted figure with permission from Ref. [7]: [Mark H. Fischer and Erez Berg, Phys. Rev. B 93, 054501, 2016]. Copyright 2016 by the American Physical Society.

3.3.1 Degenerate case

As mentioned previously, the irreducible representation E_u is two-dimensional. The eigenvalues λ of the E_u sector of $g_{\mathbf{k}_\alpha, \mathbf{q}_\beta}$ are therefore doubly-degenerate, which means that the p_x and p_y components have the same T_c. If the most negative eigenvalue is in the E_u representation, the order parameter below T_c will be given by a linear

combination of the corresponding two eigenvectors

$$\Delta_{\mathbf{k}_\alpha} = \eta_x f_x(\mathbf{k}_\alpha) + \eta_y f_y(\mathbf{k}_\alpha) \tag{3.21}$$

where $f_x(\mathbf{k}_\alpha)$ and $f_y(\mathbf{k}_\alpha)$ are the gap functions of the p_x and p_y components as obtained from the eigenvectors of g from Eq. 3.19. Note that $f_x(\mathbf{k}_\alpha)$ and $f_y(\mathbf{k}_\alpha)$ can be chosen real.

In order to discriminate between the different possible linear combinations, one needs to go to the next order in $|\Delta|^2$ in the perturbation theory of the gap equation below T_c (given in Eq. 2.98), or equivalently include quartic terms in the Ginzburg-Landau free energy functional. This functional is given by [87]

$$F[\eta_x, \eta_y] = a(|\eta_x|^2 + |\eta_y|^2) + b_1(|\eta_x|^2 + |\eta_y|^2)^2 + \frac{b_2}{2}((\eta_x^*)^2\eta_y^2 + (\eta_y^*)^2\eta_x^2) + b_3|\eta_x|^2|\eta_y|^2 \tag{3.22}$$

where we omitted gradient terms and higher order terms and where $a = a_0(T - T_c)$. The stability condition which ensures F is bounded from below is given by $4b_1 - b_2 + b_3 > 0$ and $4b_1 + b_2 + b_3 > 0$. Depending on b_2/b_1 and b_3/b_1, three different solutions can minimise F: $(\eta_x, \eta_y) = (1, 0)$, corresponding to the $\{p_x, p_y\}$ phase, $(\eta_x, \eta_y) = (1, \pm 1)$ corresponding to the $p_x \pm p_y$ phase, and $(\eta_x, \eta_y) = (1, \pm i)$ corresponding to the $p_x \pm ip_y$ phase. The phase diagram is shown in Fig. 3.2. We expect $p_x \pm ip_y$ to be favored for realistic values of b_2/b_1 and b_3/b_1 since it is the only state that does not have line nodes. The presence of nodes at the Fermi surface decreases the condensation energy.

The coefficients in the functional can be derived from BCS for a clean superconductor in the weak coupling limit, as shown by Gor'kov [119]. In this case, they are given by

$$\begin{aligned} b_1 &= b_0 \left\langle |f_x|^4 \right\rangle_{\mathrm{FS}} \\ b_2 &= 2b_0 \left\langle (f_x^*)^2 f_y^2 + (f_y^*)^2 f_x^2 \right\rangle_{\mathrm{FS}} \\ b_3 &= b_0 \left(4 \left\langle |f_x^*|^2 |f_y|^2 \right\rangle_{\mathrm{FS}} - 2 \left\langle |f_x|^4 \right\rangle_{\mathrm{FS}} \right) \end{aligned} \tag{3.23}$$

where b_0 is a positive constant that is not relevant to the present discussion. The

Fermi surface average is defined by

$$\langle h_{\mathbf{k},\alpha} \rangle_{\mathrm{FS}} = \frac{1}{\rho} \sum_{\alpha} \int_{\mathrm{FS}_\alpha} \frac{d\hat{\mathbf{k}}}{(2\pi)^D} \frac{1}{v_{\mathbf{k},\alpha}} h_{\mathbf{k},\alpha} \tag{3.24}$$

where ρ is the total density of states at the Fermi level. We found numerically that, for all the highest-T_c E_u states predicted from our calculations, the coefficients b_1, b_2, b_3 are always in the $p_x \pm ip_y$ part of the phase diagram. For example, for $J/U = 0.06$, we found $b_2/b_1 = 0.683$ and $b_3/b_1 = -0.633$.

3.4 Results

3.4.1 Gap anisotropy and chiral versus helical

Since within our approach, J and U are phenomological parameters, we will study *a priori* a large range of possible values for J/U. The estimates found in the literature[116, 117, 120, 121] for the ratio J/U range from 0.059 to 0.23. A survey of these estimates is given in the Section 3.4.4. We will focus on the range $0 \leq J/U \leq 0.3$. The singlet case appears only for $J/U > 0.29$ and has a strongly dominant gap on $\boldsymbol{\gamma}$. Based on the ample evidence in favor of a triplet order parameter, this case will be discarded in the rest of this Chapter. Notwithstanding, we will show in Chapter 5 that singlet order parameters could become more favorable than triplet ones under strong uniaxial strain, a regime that was reached in a recent experiment [10]. While, for $J/U < 0.065$, the chiral state is favored in agreement with the most prevailing assumption in the field, the helical state $\vec{d} = p_x\hat{x} + p_y\hat{y}$ takes over for $0.065 < J/U < 0.29$. As a reminder, the helical state is the two-dimensional (2D) equivalent of superfluid ^{3}He-B [13].

While a helical state would be in contradiction with the evidence for time-reversal symmetry breaking coming from muon spin relaxation [74] and optical Kerr effect [75] experiments, it would help explain other experiments that seem at odds with a chiral state. It would provide a simple explanation for the presence of edge states[78] but the

absence of edge currents [80, 81]. The absence of spin susceptibility decrease below T_c for both in-plane and out-of-plane fields measured by NMR Knight shift experiments [68, 69] has been interpreted as evidence in favor of a weakly pinned $\vec{d} \parallel c$ that can be rotated to the plane by a field $h \parallel c$ smaller than 20 mT. We emphasize that a helical state with a weakly pinned $\vec{d} \perp c$ that would be rotated by a field $h \parallel ab$ smaller than 150 mT would also be consistent with these experiments. It would also explain the emergence of out-of-plane spin fluctuations in the superconducting state [122, 123], which require in-plane fluctuations of $\vec{d}$. The disappearance of these fluctuations under an in-plane magnetic field would also be consistent with the expulsion of $\vec{d}$ from the plane under such a field. Half-quantum vortices, measured recently in a mesoscopic sample of Sr_2RuO_4 [31], correspond to a spatially dependent rotation of $\vec{d}$ in order to accommodate a half-integer flux. They require a freeing of $\vec{d}$ from its intrinsic direction imposed by SOC and their existence is therefore equally plausible in the chiral and the helical state. Given these contradictory experimental results, we will study these two states on an equal footing.

Once the mode with the most negative eigenvalue is identified, its eigenvector provides valuable information regarding the gap. The gap scale is too small to be measured directly by angle-resolved photoemission spectroscopy (ARPES) but specific heat measurements have revealed properties of the order parameter [9, 66]. In Fig. 3.3, we compare the measured [8] critical jump in specific heat $\frac{\Delta C}{C}$ with its value calculated using BCS theory with the gap functions obtained from the weak coupling calculation (the explicit formula was given in Chapter 2). The experimental estimate for this ratio is given by $\frac{\Delta C}{C} = 0.75 \pm 0.05$ [8, 9]. The two highlighted regions correspond to a prediction for $\frac{\Delta C}{C}$ in this range: the chiral OP at $J/U \simeq 0.06$ and the helical OP at $J/U \simeq 0.08$.

The departure of $\frac{\Delta C}{C}$ from its well-known BCS maximal value of 1.43 measures the anisotropy of the gap over the three FS. A large difference between the scale of the gap amplitudes on the different bands corresponds to a value of $\frac{\Delta C}{C}$ that is smaller than experiments, as can be seen in Fig. 3.3. Accordingly, the two predicted OPs in agreement with specific heat data have gaps of the same order on the three

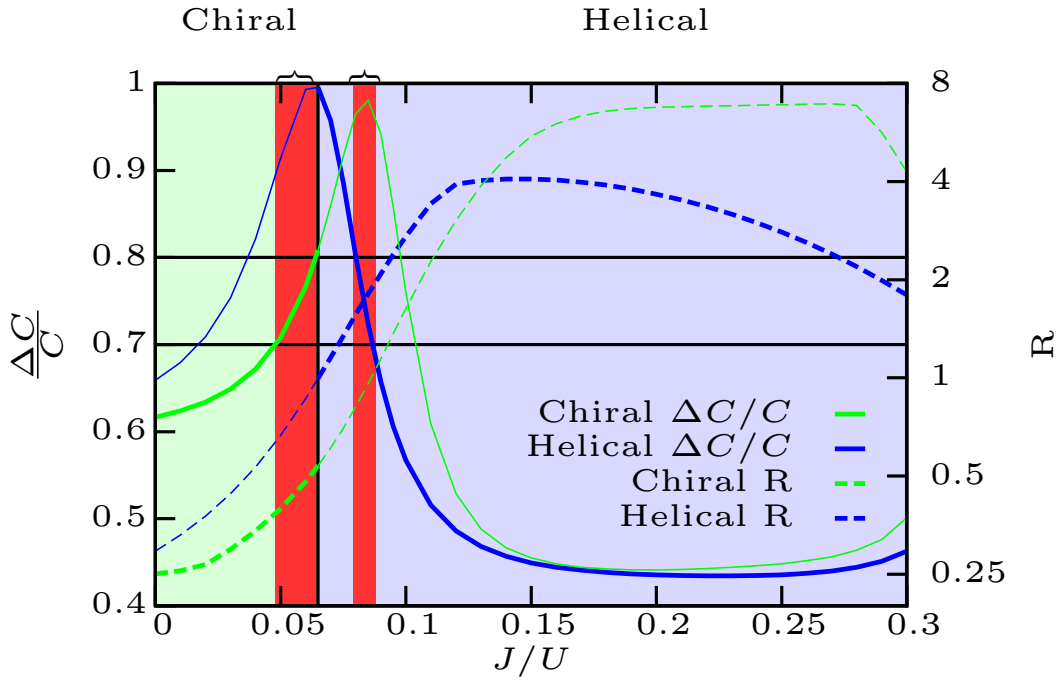

Figure 3.3: Critical specific heat jump $\frac{\Delta C}{C}$ and ratio of the maxima of the gap amplitudes over the different bands $R = \frac{\max|\Delta_{\alpha,\beta}|}{\max|\Delta_{\gamma}|}$. The vertical line separates the stability regions of the chiral and helical OPs. The curve for a given OP is drawn in full width only in the OP's stability region. The horizontal lines delimit the range of $\frac{\Delta C}{C}$ estimated from experiments: $\frac{\Delta C}{C} = 0.75 \pm 0.05$ [8, 9]. The braces indicate the range of J/U for which the prediction is compatible with experiments.

bands. The slightly dominant band is different in the two cases: The chiral state has a gap approximately two times larger on $\boldsymbol{\gamma}$ than on $\boldsymbol{\alpha}$ and $\boldsymbol{\beta}$, while the ratio of the helical gap amplitude on $\boldsymbol{\gamma}$ over the one on $\boldsymbol{\alpha}$ and $\boldsymbol{\beta}$ is approximately 0.7. By tuning J/U towards smaller values, it is possible to obtain a largely dominant gap on $\boldsymbol{\gamma}$ like previously reported [52, 55, 64, 124, 125].

As shown in Fig. 3.4, the gaps on $\boldsymbol{\alpha}$ and $\boldsymbol{\beta}$ present near-nodes near the direction $\langle 110 \rangle$ in both cases. The incommensurate peak $\mathbf{Q}$ in the antiferromagnetic fluctuation spectrum [51] of these bands is known to be responsible for the appearance of these near-nodes [9, 61]. As its fluctuations are mostly ferromagnetic, the $\boldsymbol{\gamma}$ band has been previously thought to host a fairly isotropic gap of the type $d_z = \sin(k_x) + i\sin(k_y)$, with only mild minima along $\langle 100 \rangle$ [52, 55, 64, 124, 125] and a complex phase roughly given by the polar angle around the Fermi surface. Interestingly, we

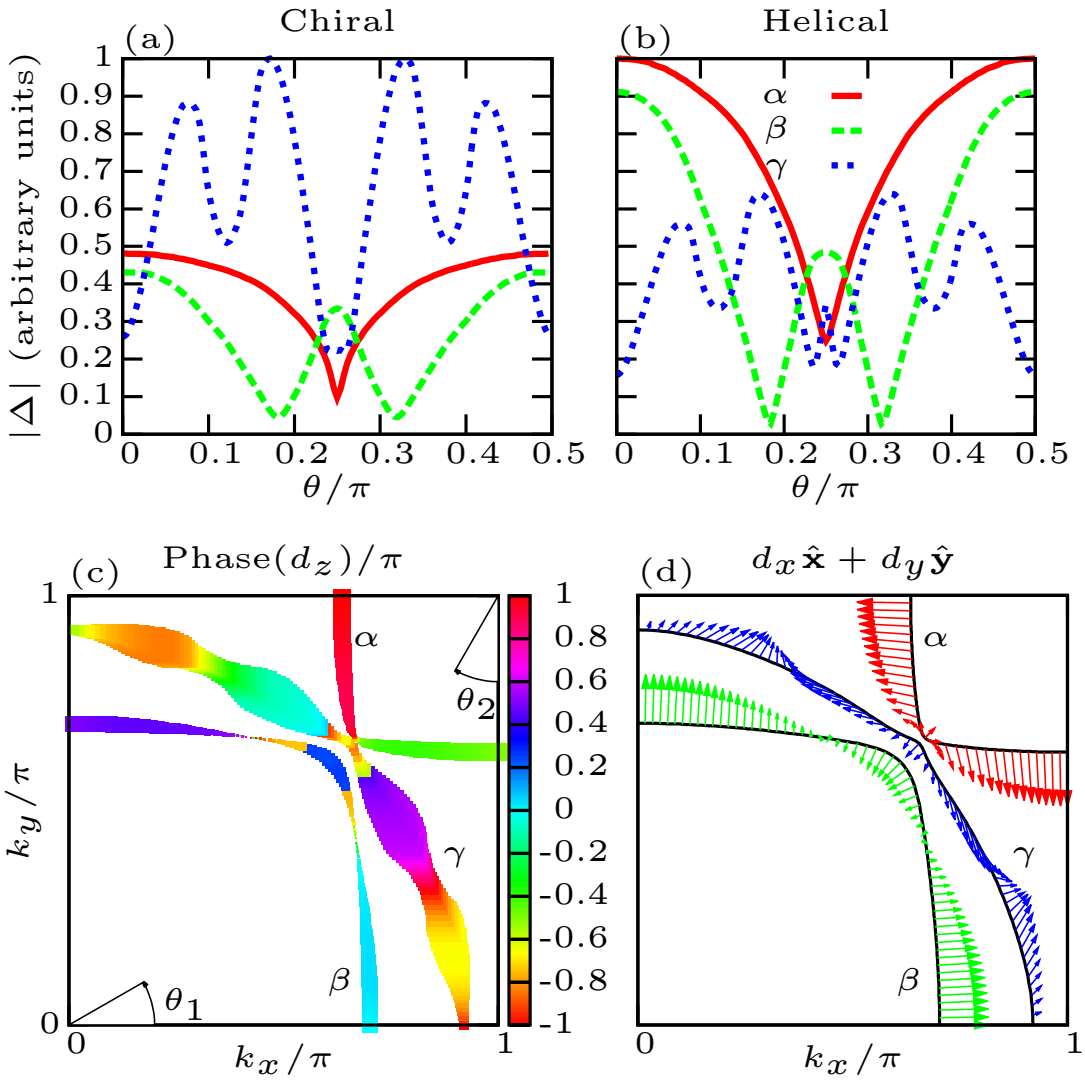

Figure 3.4: We represent the chiral OP $\vec{d} = d_z\hat{\mathbf{z}}$ for $J/U = 0.06$ (left) and the helical OP $\vec{d} = d_x\hat{\mathbf{x}} + d_y\hat{\mathbf{y}}$ for $J/U = 0.08$ (right). Panels (a) and (b) show the gap magnitude $|\Delta| \equiv \sqrt{\mathbf{d}\cdot\mathbf{d}^*}$. In panel (c), the color code gives the complex phase of d_z around the three FSs. The width of the curve is proportional to $|\Delta|$. In panel (d), the vectors are proportional to (d_x, d_y), where d_x and d_y are real. The angle θ refers to θ_1 (θ_2) in the case of β and γ (α).

find gap minima on $\boldsymbol{\gamma}$ along $\langle 110\rangle$, which shows that the quasi-one-dimensional (quasi-1D) antiferromagnetic fluctuations peak $\mathbf{Q}$ is a source of anisotropy on this band as well. In Chapter 4, we will show that the strong anisotropy of these gap functions can be reproduced by a simple pairing function with dominant higher lattice harmonics.

The rationale behind the association of the chiral state with a dominant $\boldsymbol{\gamma}$ and the helical state with dominant $\boldsymbol{\alpha}$ and $\boldsymbol{\beta}$ lies in the anisotropy of the normal-state

spin dynamics. The chiral (helical) state has an out-of-plane (in-plane) **d** and is therefore driven by in-plane (out-of-plane) magnetic fluctuations. Due to SOC, the incommensurate peak **Q** is larger for the out-of-plane component of the susceptibility [126], thereby favoring a helical state when the quasi-1D bands are dominant. On the other hand, the (ferromagnetic) long wavelength part of the spectrum is larger for the in-plane component, which favors a chiral state when $\boldsymbol{\gamma}$ is dominant.

By a microscopic accounting of multiband and SOC effects, our model reconciles the two distinct scenarios of 2D superconductivity on $\boldsymbol{\gamma}$ versus quasi-1D superconductivity on $\boldsymbol{\alpha}$ and $\boldsymbol{\beta}$ inside one framework. As required by specific heat data[9] and in contrast to previous calculations [55, 61], similarly sized gaps on all three bands are obtained and, depending on the interaction parameter, the balance can be slightly tilted one way or another. As shown in Fig. 3.3, this result is true for both the chiral and the helical state and is therefore robust regardless of the favored pairing symmetry.

We now discuss experiments probing the relative size of the gaps on the different bands. Recently, out-of-plane STM [9] has exhibited the presence of a near-nodal gap of 0.350 meV. Based on orbital anisotropy, it was argued that this gap is present on $\boldsymbol{\alpha}$ and $\boldsymbol{\beta}$: The tunnelling matrix element for out-of-plane tunnelling is expected to be much larger for the d_{zx} and d_{zy} orbitals since they stick out of the plane, while the d_{xy} orbital does not. We find a position for the near-nodes on $\boldsymbol{\alpha}$ and $\boldsymbol{\beta}$ that is consistent with their phenomenological model. The fact that the measured gap size corresponds to $2\Delta/T_c \simeq 5$, which is close to the BCS value, was interpreted as evidence that $\boldsymbol{\alpha}$ and $\boldsymbol{\beta}$ are dominant. A gap 0.7 times smaller on $\boldsymbol{\gamma}$ was then inferred from the specific heat jump value, in agreement with our findings for the helical state.

On the other hand, the conductance of in-plane tunneling junctions [78] has been reported to present a two-step peak shape that is consistent with a dominant gap of 0.93 meV on $\boldsymbol{\gamma}$ and a subdominant gap of 0.28 meV on $\boldsymbol{\alpha}$ and $\boldsymbol{\beta}$. The relative sizes of the gap amplitude on the different bands would then point towards the chiral scenario.

The inclusion of η is crucial to study the orientation of $\vec{d}$ since, without SOC, the

spin $SU(2)$ symmetry would be preserved and the chiral and helical states would be degenerate. The splitting between the pairing eigenvalue of these states grows with the magnitude of η but our conclusions are robust against a change in this parameter: The favored state is always chiral with a (slightly) dominant $\boldsymbol{\gamma}$ for small J/U and helical with (slightly) dominant $\boldsymbol{\alpha}$ and $\boldsymbol{\beta}$ for larger J/U.

Finally, we emphasize the need for new experiments that would make it possible to discriminate between the two proposed states. In-plane STM could be one of them since it could also probe the gap on the d_{xy} orbitals. Experiments probing the phase of the order parameter, including quasiparticle interference and Josephson tunneling spectroscopy[76, 108, 109], could be discriminating but their interpretation is nontrivial given the reported convoluted dependence of that phase on the in-plane orientation. Methods to detect helical edge modes have also been proposed recently [127].

3.4.2 Pairing eigenvalue

In Fig. 3.5, we show the pairing eigenvalue λ for different pairing symmetries. The favoured state is the one with the largest value of $|\lambda|$. We show the eigenvalue for two odd-parity channels: one for the chiral state $\vec{d} = (p_x \pm ip_y)\hat{\mathbf{z}}$ and one for the most favoured helical state $\vec{d} = p_x\hat{\mathbf{x}} + p_y\hat{\mathbf{y}}$. We also show the most favoured state in the even-parity (i.e. pseudo-spin singlet) channel. Except for very high J/U (> 0.29), the even-parity channel is never favoured.

The splitting between the pairing eigenvalue of the helical states and the chiral state is shown in Fig. 3.6. The chiral state is favoured for $J/U < 0.065$ while the helical state $\vec{d} = p_x\hat{\mathbf{x}} + p_y\hat{\mathbf{y}}$ takes over for $J/U > 0.065$.

3.4.3 Impact of spin-orbit coupling

The impact of η on the splitting between the pairing eigenvalue of the helical state and the chiral state is shown in Fig. 3.7. The curves are fairly similar for all values of η: a region of negative splitting (i.e. favoured chiral state) at small J/U and

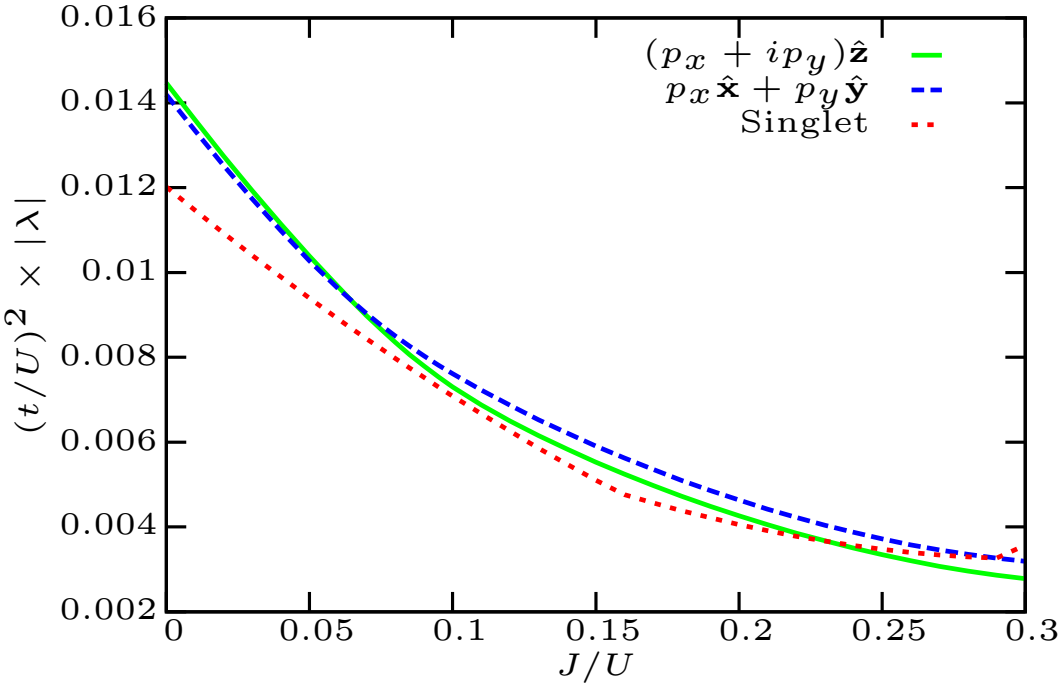

Figure 3.5: Pairing eigenvalue λ for the chiral state, the most favoured helical state and the singlet state for the parameters given in the main text.

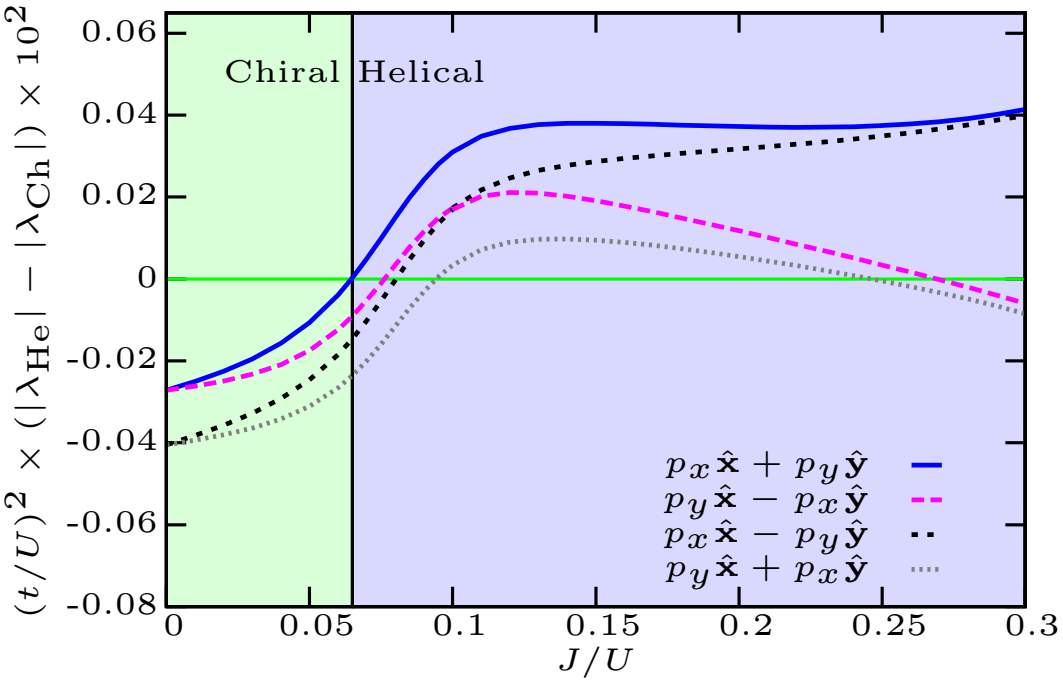

Figure 3.6: Splitting of the pairing eigenvalue λ between the four different helical states and the chiral state for the parameters given in the main text.

a region of positive splitting (i.e. favoured helical state) at large J/U. These two regions are linked by a cross-over at a certain value for J/U. As indicated by the arrows in Fig. 3.7, increasing η does mostly two things: it increases the amplitude of the splitting (be it positive or negative) in the two aforementionned regions and slightly increases the value of J/U at which the cross-over happens. It also makes the cross-over smoother. In the limit $\eta \to 0$, the splitting would go to zero, from below in the former region and from above in the latter.

The ratio of the maxima of the gap amplitudes over the different bands $R = \frac{\max|\Delta_{\alpha,\beta}|}{\max|\Delta_{\gamma}|}$ for different SOC parameters η is shown in Fig. 3.8. Regardless of the value of η, the chiral state favoured at small J/U has a larger gap magnitude on $\boldsymbol{\gamma}$ while the helical state at larger J/U has a larger gap amplitude on $\boldsymbol{\alpha}$ and $\boldsymbol{\beta}$.

In summary, the amplitude of η does not modify qualitatively our findings of a favoured chiral state with a (slightly) dominant $\boldsymbol{\gamma}$ for small J/U and a favoured helical state with (slightly) dominant $\boldsymbol{\alpha}$ and $\boldsymbol{\beta}$ for larger J/U.

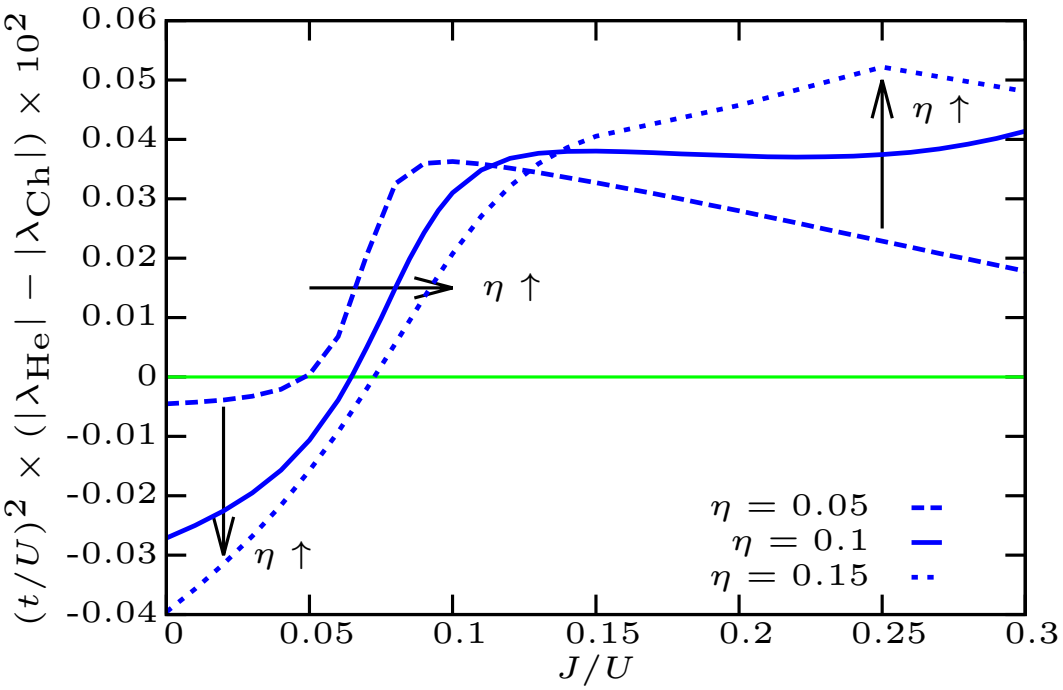

Figure 3.7: Splitting of the pairing eigenvalues λ between the chiral and the helical state for different SOC parameters η. All the other parameters are given in the main text.

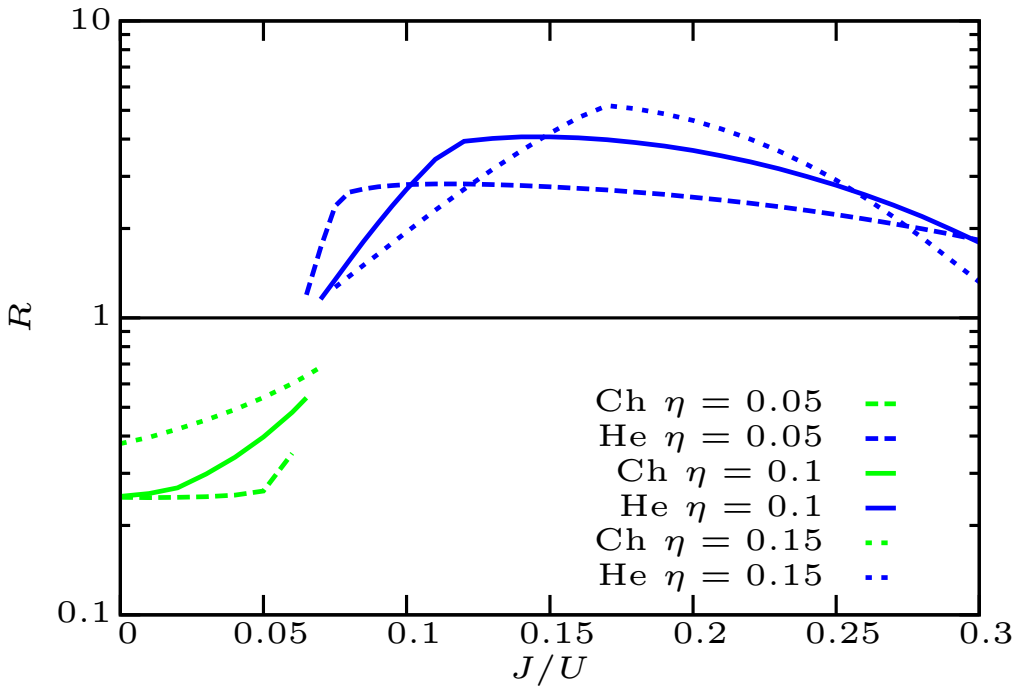

Figure 3.8: Ratio of the maxima of the gap amplitudes over the different bands $R = \frac{\max|\Delta_{\alpha,\beta}|}{\max|\Delta_{\gamma}|}$ for different SOC parameters η. All the other parameters are given in the main text. At each value of J/U, only the curve for the most favoured state (chiral or helical) is shown. "Ch" stands for chiral and "He" stands for helical.

3.5 Conclusion

In this chapter, we studied superconductivity in Sr_2RuO_4 in the weak coupling limit using a model that includes spin-orbit coupling and multiband effects. We showed these effects to be crucial to discriminate between the possible order parameters. In contrast to previous results and without the necessity of fine-tuning, we obtained pseudospin-triplet gaps of the same order of magnitude on the two-dimensional $\boldsymbol{\gamma}$ band and the quasi-one-dimensional $\boldsymbol{\alpha}$ and $\boldsymbol{\beta}$ bands. The ratio of the gap amplitude on the different bands varies continuously with the interaction parameter. The favored pairing symmetry was shown to be chiral when $\boldsymbol{\gamma}$ is slightly dominant and helical when $\boldsymbol{\alpha}$ and $\boldsymbol{\beta}$ are slightly dominant.

4. Edge Currents

4.1 Introduction

As explained in Chapter 3, the most favored odd-parity superconducting order parameter in Sr_2RuO_4 can be either chiral or helical. Chiral superconductors break time-reversal symmetry, have a $\mathbb{Z}$ topological number (called hereby the Chern number C and defined below) and exhibit chiral Majorana edge modes while helical superconductors are time-reversal symmetric, have a $\mathbb{Z}_2$ topological number and exhibit counter-propagating Majorana edge modes that are time-reversed partners. In this section, we focus on the chiral case, and compute the Chern number of the predicted order parameter. We show this Chern number to be -7, instead of the usually assumed $+1$. This large Chern number leads to drastic differences for several experiments, including thermal and charge edge current measurements. Note that the above classification appears for two-dimensional systems, while Sr_2RuO_4 is strictly speaking three-dimensional. Yet, thanks to the very small k_z dispersion in Sr_2RuO_4, we approximate it by a strictly two-dimensional system in the following. The currents computed in this Chapter should therefore be understood per layer.

4.2 Chern number

In this section, we first define the Chern number in the simple case of a single-band, spinless superconductor, and then we generalize this to the multi-band spinful case relevant to Sr_2RuO_4. The experimental implications of a non-zero Chern number will be discussed in the next section.

4.2.1 Single-band spinless case

For a single-band, spinless (or spin polarized) superconductor, the mean-field Hamiltonian is given by [35]:

$$H = \frac{1}{2}\sum_{\mathbf{k}} \psi_{\mathbf{k}}^{\dagger} \mathcal{H}_{\mathbf{k}} \psi_{\mathbf{k}} \tag{4.1}$$

with $\psi_{\mathbf{k}}^{\dagger} = [c_{\mathbf{k}}^{\dagger}, c_{-\mathbf{k}}]$ and with

$$\mathcal{H}_{\mathbf{k}} = \begin{pmatrix} \xi_{\mathbf{k}} & d_{z,\mathbf{k}} \\ d_{z,\mathbf{k}}^{*} & -\xi_{\mathbf{k}} \end{pmatrix}. \tag{4.2}$$

The Bogolyubov transformation can be written as

$$\begin{aligned} c_{\mathbf{k}}^{\dagger} &= v'_{\mathbf{k}} a_{\mathbf{k}}^{\dagger} + v_{\mathbf{k}}^{*} a_{-\mathbf{k}} \\ a_{\mathbf{k}}^{\dagger} &= (v'_{\mathbf{k}})^{*} c_{\mathbf{k}}^{\dagger} - v_{\mathbf{k}}^{*} c_{-\mathbf{k}} \\ v'_{\mathbf{k}} &= i e^{-i\Theta_{\mathbf{k}}/2} \cos(\theta_{\mathbf{k}}) \\ v_{\mathbf{k}} &= -i e^{i\Theta_{\mathbf{k}}/2} \sin(\theta_{\mathbf{k}}) \\ \cot(2\theta_{\mathbf{k}}) &= \frac{\xi_{\mathbf{k}}}{|d_{z,\mathbf{k}}|} \\ |v'_{\mathbf{k}}|^2 + |v_{\mathbf{k}}|^2 &= 1 \\ |v'_{\mathbf{k}}|^2 - |v_{\mathbf{k}}|^2 &= \frac{\xi_{\mathbf{k}}}{E_{\mathbf{k}}} \\ (v'_{\mathbf{k}})^{*} v_{\mathbf{k}} &= -\frac{1}{2}\frac{d_{z,\mathbf{k}}}{E_{\mathbf{k}}} \\ E_{\mathbf{k}} &= \sqrt{\xi_{\mathbf{k}}^2 + |d_{z,\mathbf{k}}|^2} \end{aligned} \tag{4.3}$$

where $d_{z,\mathbf{k}} = |d_{z,\mathbf{k}}| e^{i\Theta_{\mathbf{k}}}$.

After this transformation, the Hamiltonian reads

$$H = \sum_{\mathbf{k}} E_{\mathbf{k}} a_{\mathbf{k}}^{\dagger} a_{\mathbf{k}} + E_0 \tag{4.4}$$

with $E_0 = -\frac{1}{2}\sum_{\mathbf{k}}(E_{\mathbf{k}} - \xi_{\mathbf{k}})$. As long as $|d_{z,\mathbf{k}}| \neq 0$ everywhere on the Fermi surface, the ground state (defined by $a_{\mathbf{k}} |\mathrm{GS}\rangle = 0$) is gapped and one can define a Chern

number $C \in \mathbb{Z}$ according to [128]:

$$C = \frac{1}{4\pi} \int d\mathbf{k}\ \hat{m}(\mathbf{k}) \cdot \left(\partial_{k_x} \hat{m}(\mathbf{k}) \times \partial_{k_y} \hat{m}(\mathbf{k})\right) \tag{4.5}$$

where $\vec{m}(\mathbf{k}) = \{\mathrm{Re}[d_{z,\mathbf{k}}], -\mathrm{Im}[d_{z,\mathbf{k}}], \xi_{\mathbf{k}}\}$, $\hat{m} = \vec{m}/|\vec{m}|$, and where the integral is over the Brillouin zone. This topological index gives the homotopy class of the map from the 2D torus (the Brillouin zone) to the sphere (the target space of a three-dimensional unit vector) defined by $\hat{m}(\mathbf{k})$. It can be shown that the Chern number is also given by the winding of the complex phase of d_z around the Fermi surface [129]:

$$C = \frac{1}{2\pi} \oint_{\mathrm{FS}} \nabla(\Theta_{\mathbf{k}}) \cdot d\mathbf{k} \tag{4.6}$$

where the Fermi surface is a directed boundary between the "electron" region ($\xi < 0$) on the inside and the "hole" region ($\xi > 0$) on the outside.

The gap is given by the minimum of $E_{\mathbf{k}} = |\vec{m}(\mathbf{k})|$ over the Brillouin zone, and a state is thus fully gapped as long as $|\vec{m}(\mathbf{k})| \neq 0\ \forall \mathbf{k}$. The Chern number is invariant under smooth deformations of $\vec{m}(\mathbf{k})$. It can only change if the gap closes, making $\hat{m}(\mathbf{k})$ ill-defined at some momentum.

Note that we always assume that the chemical potential lies within the band, and that we can therefore use the concept of a Fermi surface. This corresponds to the so-called weak pairing (or BCS) regime, as opposed to the the strong pairing (or BEC) regime [38].

4.2.2 Multi-band spinful case

We now wish to discuss the case of interest for Sr_2RuO_4, a chiral superconductor with two pseudo-spin species and multiple bands. At the end of Chapter 2, we obtained a mean-field Hamiltonian for such a superconductor given by

$$H = \frac{1}{2} \sum_{\mathbf{k},\alpha} \psi^{\dagger}_{\mathbf{k},\alpha} \mathcal{H}_{\mathbf{k},\alpha} \psi_{\mathbf{k},\alpha} \tag{4.7}$$

with $\psi^\dagger_{\mathbf{k},\alpha} = [c^\dagger_{\mathbf{k},\alpha,+} c^\dagger_{\mathbf{k},\alpha,-} c_{-\mathbf{k},\alpha,+} c_{-\mathbf{k},\alpha,-}]$ and with

$$\mathcal{H}_{\mathbf{k},\alpha} = \begin{pmatrix} \xi_{\mathbf{k},\alpha} & 0 & 0 & d_{z,\mathbf{k},\alpha} \\ 0 & \xi_{\mathbf{k},\alpha} & d_{z,\mathbf{k},\alpha} & 0 \\ 0 & d^*_{z,\mathbf{k},\alpha} & -\xi_{\mathbf{k},\alpha} & 0 \\ d^*_{z,\mathbf{k},\alpha} & 0 & 0 & -\xi_{\mathbf{k},\alpha} \end{pmatrix}. \tag{4.8}$$

Since this Hamiltonian is diagonal in band space, we can treat each band as an independent system, and the total Chern number C will be given by the sum of C for each band:

$$C = \sum_\alpha C_\alpha. \tag{4.9}$$

While the pairing couples electrons of different pseudo-spin σ species, it is possible to perform a pseudo-spin rotation so that the pairing is diagonal in the new pseudo-spin species σ'. This rotation is given by

$$\begin{aligned} c^\dagger_{\mathbf{k},\alpha,+'} &= \frac{1}{\sqrt{2}} \left(c^\dagger_{\mathbf{k},\alpha,+} + c^\dagger_{\mathbf{k},\alpha,-} \right) \\ c^\dagger_{\mathbf{k},\alpha,-'} &= \frac{1}{\sqrt{2}} \left(c^\dagger_{\mathbf{k},\alpha,+} - c^\dagger_{\mathbf{k},\alpha,-} \right). \end{aligned} \tag{4.10}$$

The Hamiltonian then reads

$$\mathcal{H}_{\mathbf{k},\alpha} = \begin{pmatrix} \xi_{\mathbf{k},\alpha} & 0 & d_{z,\mathbf{k},\alpha} & 0 \\ 0 & \xi_{\mathbf{k},\alpha} & 0 & -d_{z,\mathbf{k},\alpha} \\ d^*_{z,\mathbf{k},\alpha} & 0 & -\xi_{\mathbf{k},\alpha} & 0 \\ 0 & -d^*_{z,\mathbf{k},\alpha} & 0 & -\xi_{\mathbf{k},\alpha} \end{pmatrix}. \tag{4.11}$$

in the basis given by $[c^\dagger_{\mathbf{k},\alpha,+'} c^\dagger_{\mathbf{k},\alpha,-'} c_{-\mathbf{k},\alpha,+'} c_{-\mathbf{k},\alpha,-'}]$. For each band, we therefore have two decoupled spin-polarized chiral superconductors, one for the $+'$ species with an order parameter given by $d_{z,\mathbf{k},\alpha}$ and one for the $-'$ species with an order parameter given by $-d_{z,\mathbf{k},\alpha}$. We can use the formula given in the previous section for each species separately. Since $d_{z,\mathbf{k},\alpha}$ and $-d_{z,\mathbf{k},\alpha}$ have the same complex phase up to an additive uniform π constant, the two species have the same Chern number. In this thesis, C

will be used as the Chern number per spin species so as to avoid factors of two.

4.2.3 The case of Sr_2RuO_4

In Chapter 2, we showed that, with an appropriate choice of pseudo-spin basis, pseudo-spin $\vec{d}$ transforms like a vector under the double group of the crystal. As a reminder, the double group is the group of discrete symmetry transformations of the crystal performed simultaneously in real and spin space. Since Sr_2RuO_4 is tetragonal, $\vec{d}$ should transform according to a given irreducible representation of D_{4h}. Among the odd-parity irreducible representations of D_{4h} (given in Table 3.1), the only one corresponding to a chiral state is E_u, for which the order parameter should be given by $d_z = h_x + i\ h_y$ (or $d_z = h_x - i\ h_y$ for the opposite chirality) where $h_{x,y}$ stands for any function of momentum that transforms in the same way as $\sin(k_{x,y})$ under the symmetry operations of D_{4h}.

Let us first discuss the simplest example:

$$d^{\text{Naive}}_{z,\mathbf{k},\alpha} \equiv \sin(k_x) + i \sin(k_y)\ \forall\ \alpha, \tag{4.12}$$

where $\alpha = \boldsymbol{\alpha}, \boldsymbol{\beta}, \boldsymbol{\gamma}$ is the band index. In this case, in analogy with superfluid ^{3}He-A, the superconducting state is supposed to be driven by ferromagnetic fluctuations on the fairly isotropic $\boldsymbol{\gamma}$ band, which is therefore the dominant band in this scenario. The two other bands, called $\boldsymbol{\alpha}$ and $\boldsymbol{\beta}$, are then merely spectators. Considering d^{Naive}_z as shown in Fig. 4.1(b), it is easy to see that $C = +1$ for a FS centered at $(0, 0)$ and $C = -1$ for a FS centered at (π, π). Since there are two bands of the former type ($\boldsymbol{\beta}$ and $\boldsymbol{\gamma}$) and one band of the latter type ($\boldsymbol{\alpha}$) in Sr_2RuO_4, the total Chern number in this case is $C = 1$.

The issue with this scenario is that a chiral superconductor with $C = 1$ is generically expected to have non-zero edge currents, which have been elusive so far despite intense scrutiny[80, 81, 130]. Spontaneous angular momentum and currents in chiral superfluids have been studied extensively[131–136] and it was confirmed recently that, for $C = 1$, in both the continuum case and the case of a square lattice with nearest-

neighbor pairing, these currents are quite inevitable[137–140]. The apparent contradiction between measurements of time-reversal symmetry breaking and the absence of measurable edge currents has been a long-standing puzzle about Sr_2RuO_4[141].

The dominant $\boldsymbol{\gamma}$ scenario was challenged by a microscopic calculation[99, 142, 143] that showed that, in the weak-coupling limit, the quasi-one-dimensional (1D) $\boldsymbol{\alpha}$ and $\boldsymbol{\beta}$ bands are actually driving superconductivity through antiferromagnetic fluctuations caused by the nesting of their FSs[56–62]. The gap was therefore thought to be dominant on these two bands whose total Chern number is zero for an OP given by d_z^{Naive}, thereby making Sr_2RuO_4 a topologically trivial superconductor. STM data showed that these bands have a gap amplitude in accordance with BCS theory given the value of T_c, thus supporting the idea that the main gap is on the $\boldsymbol{\alpha}$ and $\boldsymbol{\beta}$ bands[9]. The problem with this scenario is that, from thermodynamic data, it is believed that the gap should be of similar size on all three bands[8, 9, 65], and that therefore $\boldsymbol{\gamma}$ should have a sizable gap which must lead to a nontrivial topology and presumably sizable edge currents. Futhermore, while the Chern numbers of $\boldsymbol{\alpha}$ and $\boldsymbol{\beta}$ are opposite in the case of d_z^{Naive}, this is not true in general, and it is in particular not true for the type of order parameter favored by the nesting of $\boldsymbol{\alpha}$ and $\boldsymbol{\beta}$, as we will show later on.

In Chapter 3, we used a weak coupling microscopic calculation which includes inter-band coupling and spin-orbit coupling to study the most favoured superconducting order parameters. The inclusion of these effects was shown to be crucial since it enabled us to obtain a similarly-sized gap on all three bands without any fine tuning, in agreement with thermodynamic data and in contrast to previous results. Depending on the ratio of Hund's coupling J to Hubbard interation U, this calculation could either favour a chiral state in the E_u representation, or a helical state in the A_{1u} representation. Because of the evidence of time-reversal symmetry breaking, we will focus on the former case in this Chapter. We will use the order parameter predicted for $J/U = 0.06$, as it was shown to reproduce the correct specific heat jump in Chapter 3. The gap function we obtain in the E_u representation $d_{z,\mathbf{k},\alpha}^{\text{Calc}}$ has a highly non-trivial momentum dependence (see Fig. 4.1(c)), indicative of pairing with a range longer than nearest neighbors.

The main result of this Chapter is the following: instead of having $C = +1$ for each FS centered at $\mathbf{k} = (0, 0)$, like for d_z^{Naive} and for a continuum $p_x + ip_y$ state, the OP d_z^{Calc} has a Chern number of -3 for the bands $\boldsymbol{\beta}$ and $\boldsymbol{\gamma}$, as seen in Fig. 4.1(c). This is allowed by symmetry, since being in the E_u representation fixes the Chern number of a FS centered at $(0, 0)$ to be 1, but only modulo 4. Adding $C_{\boldsymbol{\alpha}} = -1$ (which has a different value from $\boldsymbol{\beta}$ and $\boldsymbol{\gamma}$ since it is centered at (π, π) and not at $(0, 0)$), this leads to a total Chern number of -7. This is a dramatic change compared to the continuum case and this shows that, when lattice effects are strong, it can be misleading to have continuum OPs in mind.

4.2.4 Source of anisotropy

Before discussing the experimental implications of this result, let us first give an intuitive understanding of the source of this longer range pairing. Generically, the real (imaginary) part of an OP in the E_u representation, called h_x (h_y), can be written as a linear combination of all possible harmonics $g_x(\mathbf{k})$ ($g_y(\mathbf{k})$) that transform under D_{4h} in the same way as $\sin(k_x)$ ($\sin(k_y)$). The most simple one is obviously

$$g_{x,1}(\mathbf{k}) = \sin(k_x) \tag{4.13}$$

and corresponds to nearest neighbor pairing. We find that the non-trivial anisotropy of $d^{\nu}_{z,\text{RG}}(\mathbf{k})$ originates from two longer range pairing components that are favored on all three orbitals and that are given by

$$\begin{aligned} g_{x,2}(\mathbf{k}) &\equiv \sin(k_x)\cos(k_y) \\ g_{x,3}(\mathbf{k}) &\equiv \sin(3k_x). \end{aligned} \tag{4.14}$$

These components are favored due to the presence of strong fluctuations at the nesting wavevectors $(\pm 2\pi/3, \pi)$ and $(\pm 2\pi/3, \pm 2\pi/3)$, respectively.

In order to gain some intuition about this problem, it is instructive to first look at the simple case of a single-orbital Hubbard model. As shown in Chapter 2, applying

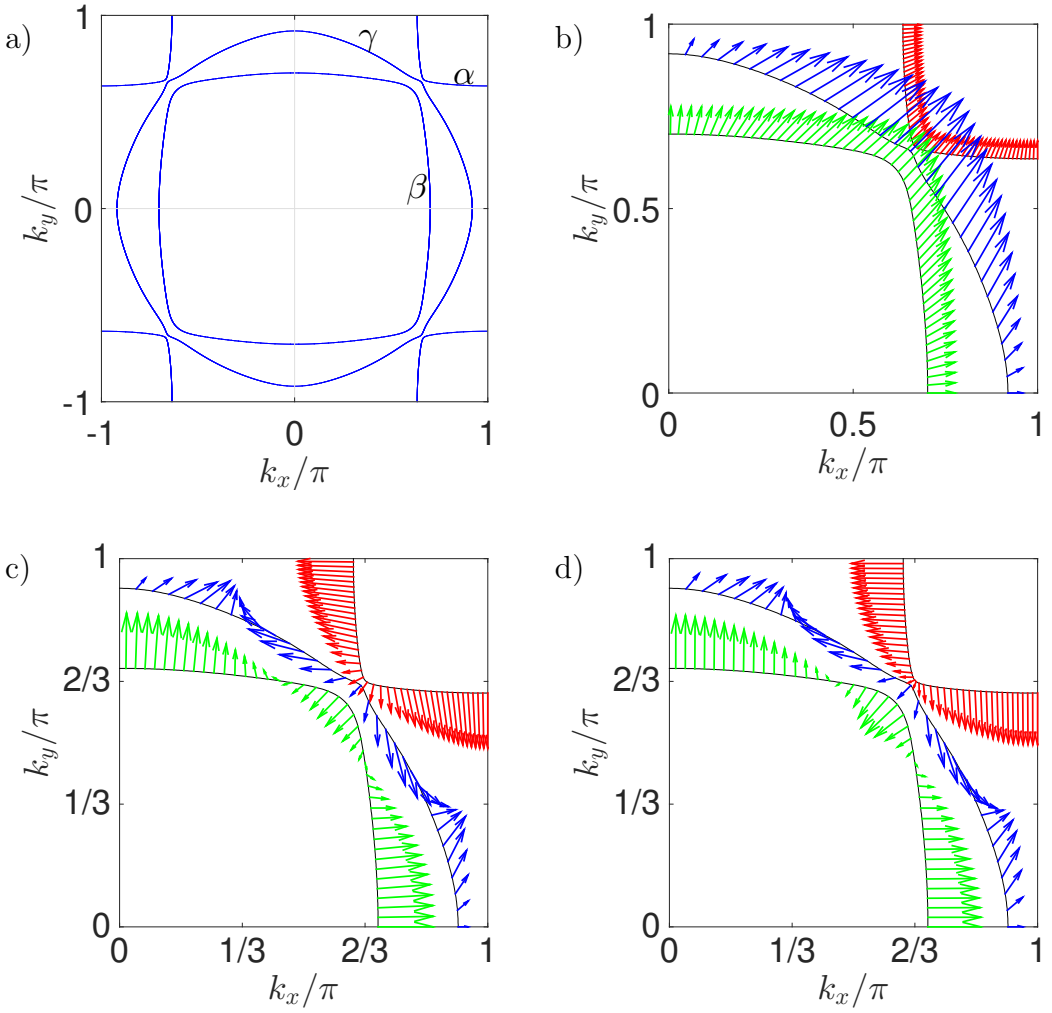

Figure 4.1: (a) Fermi surfaces for the tight-binding model given in Chapter 3. (b) Order parameter $d^{\text{Naive}}_{z,\mathbf{k},\alpha}$. The x and y components of the arrows give the real and imaginary part of d_z, respectively. The units are arbitrary. (c),(d) Same plot for $d^{\text{Calc}}_{z,\mathbf{k},\alpha}$ (obtained for $J/U = 0.06$), $d^{\text{Fit}}_{z,\mathbf{k},\alpha}$, respectively. Even though the gap has deep minima, it remains finite at all $\mathbf{k}$. Note that, unlike $d^{\text{Calc}}_{z,\mathbf{k}}$, $d^{\text{Fit}}_{z,\mathbf{k}}$ is not strictly diagonal in band space. Yet, its inter-band components are comparatively smaller and we therefore only plot $d^{\text{Fit}}_{z,\mathbf{k},\alpha} \equiv d^{\text{Fit}}_{z,\mathbf{k},\alpha,\alpha}$.

the weak coupling scheme to this case, one finds an effective interaction in the odd-parity superconducting channel given by

$$\hat{\Gamma}_{\mathbf{k},\mathbf{q}} = -U^2 \chi(\mathbf{k}-\mathbf{q}) \tag{4.15}$$

where χ is the particle-hole susceptibility and has maxima at the nesting wavevectors $\mathbf{Q}$. Neglecting Fermi velocity factors which are explained in full details in Chapter 2, the most favored superconducting OP $\Delta(\mathbf{k}) = d_{z,\mathbf{k}}$ is the eigenvector of $\hat{\Gamma}_{\mathbf{k},\mathbf{q}}$ with the most negative eigenvalue. In order to achieve a maximally negative eigenvalue, it is favourable to have

$$\arg\left[\Delta(\mathbf{k}+\mathbf{Q})\right] = \arg\left[\Delta(\mathbf{k})\right] \tag{4.16}$$

where $\mathbf{k}$ and $\mathbf{k}+\mathbf{Q}$ both lie on the FS. Depending on the value of $\mathbf{Q}$, this will favour certain gap functions over others.

As stated earlier, the driving force behind superconductivity are the strong fluctuations created by the nesting of the $\boldsymbol{\alpha}$ and $\boldsymbol{\beta}$ FSs. These FSs are generated by the small hybridization of the d_{xz} and d_{yz} orbitals, whose unhybridized FSs are given by almost straight lines at $k_x = \pm k_F$ (resp. $k_y = \pm k_F$), with $k_F \simeq 2\pi/3$. Let us first neglect hybridization and focus on d_{xz} only. If there was no hopping along the y direction at all, the FSs would be straight lines, and the nesting wavevectors would be given by $(\pm 2k_F, k_y)$ for any k_y. Instead, the small nearest-neighbor hopping along the y direction (given by $t^{\perp}$) creates a warping of the FSs that is such that the nesting wavevectors are given by $(\pm 2k_F, \pi)$. The constraint can then be rewritten as

$$\arg\left[\Delta(k_F - 2k_F, k_y + \pi)\right] = \arg\left[\Delta(k_F, k_y)\right]. \tag{4.17}$$

For $\sin(k_x)$, these two values have opposite sign and it is therefore expected for this pairing to be strongly suppressed on the quasi-1D orbitals. On the contrary, the gap function $\sin(k_x)\cos(k_y)$, corresponding to a second neighbor pairing, satisfies the above constraint and is expected to be favored [61].

Now, once hybridization is taken into account, the nesting wavevector becomes

$\mathbf{Q} = (\pm 2k_F, \pm 2k_F) \simeq (\mp 2\pi/3, \mp 2\pi/3)$, in accordance with neutron data[51]. In this case, the condition from Eq. 4.16 is clearly satisfied by the function $\sin(3k_x)$, corresponding to a pairing with a neighbour separated by three lattice constants along $\langle 100 \rangle$ [63].

The argument given so far only applied to the quasi-1D orbitals. Yet, thanks to spin-orbit coupling, inter-orbital hopping and inter-orbital interaction, superconductivity naturally arises on all the three bands, even though nesting originates from $\boldsymbol{\alpha}$ and $\boldsymbol{\beta}$ [144]. We therefore expect $g_2(\mathbf{k})$ and $g_3(\mathbf{k})$ to be present along with $g_1(\mathbf{k})$ on the quasi-2D orbital d_{xy} which dominantly contributes to $\boldsymbol{\gamma}$ at the Fermi level.

4.2.5 Change to orbital basis

The contribution of these lattice harmonics $g_{1,2,3}(\mathbf{k})$ to $d^{\text{Calc}}_{z,\mathbf{k},\alpha}$ can be made explicit by computing the gap in the atomic orbital basis. Using the unitary transformation defined in Chapter 2,

$$c^{\dagger}_{\mathbf{k},\alpha,\sigma} = \sum_{a,s} u^{\alpha,\sigma}_{a,s}(\mathbf{k}) c^{\dagger}_{\mathbf{k},a,s}, \tag{4.18}$$

the order parameter can be computed in orbital basis:

$$\Delta^{\text{Calc}}_{\mathbf{k},a_1,s_1,a_2,s_2} = \sum_{\alpha} d^{\text{Calc}}_{z,\mathbf{k},\alpha} (u^{\alpha,+}_{a_1,s_1}(\mathbf{k}) u^{\alpha,-}_{a_2,s_2}(-\mathbf{k}) + u^{\alpha,-}_{a_1,s_1}(\mathbf{k}) u^{\alpha,+}_{a_2,s_2}(-\mathbf{k})). \tag{4.19}$$

As a reminder, $a = A, B, C$ (labels for, respectively, zx, yz, xy) is the orbital index and $s = \pm 1$ is the spin index. $\Delta^{\text{Calc}}_{\mathbf{k},a_1,s_1,a_2,s_2}$ is defined such that the pairing term in the Hamiltonian is given by

$$H_{\Delta} = \sum_{\mathbf{k},a_1,a_2,s_1,s_2} \Delta^{\text{Calc}}_{\mathbf{k},a_1,s_1,a_2,s_2} c^{\dagger}_{\mathbf{k},a_1,s_1} c^{\dagger}_{-\mathbf{k},a_2,s_2} + \text{h.c.} \tag{4.20}$$

For each momentum $\mathbf{k}$, the sum over indices a_1, a_2, s_1, s_2 in H_Δ is given by

$$\begin{pmatrix} c^\dagger_{A\downarrow} & c^\dagger_{B\downarrow} & c^\dagger_{C\uparrow} & c^\dagger_{A\uparrow} & c^\dagger_{B\uparrow} & c^\dagger_{C\downarrow} \end{pmatrix} \begin{pmatrix} 0 & 0 & 0 & \Delta^{\text{Calc}}_{A\downarrow A\uparrow} & \Delta^{\text{Calc}}_{A\downarrow B\uparrow} & \Delta^{\text{Calc}}_{A\downarrow C\downarrow} \\ 0 & 0 & 0 & \Delta^{\text{Calc}}_{B\downarrow A\uparrow} & \Delta^{\text{Calc}}_{B\downarrow B\uparrow} & \Delta^{\text{Calc}}_{B\downarrow C\downarrow} \\ 0 & 0 & 0 & \Delta^{\text{Calc}}_{C\uparrow A\uparrow} & \Delta^{\text{Calc}}_{C\uparrow B\uparrow} & \Delta^{\text{Calc}}_{C\uparrow C\downarrow} \\ \Delta^{\text{Calc}}_{A\uparrow A\downarrow} & \Delta^{\text{Calc}}_{A\uparrow B\downarrow} & \Delta^{\text{Calc}}_{A\uparrow C\uparrow} & 0 & 0 & 0 \\ \Delta^{\text{Calc}}_{B\uparrow A\downarrow} & \Delta^{\text{Calc}}_{B\uparrow B\downarrow} & \Delta^{\text{Calc}}_{B\uparrow C\uparrow} & 0 & 0 & 0 \\ \Delta^{\text{Calc}}_{C\downarrow A\downarrow} & \Delta^{\text{Calc}}_{C\downarrow B\downarrow} & \Delta^{\text{Calc}}_{C\downarrow C\uparrow} & 0 & 0 & 0 \end{pmatrix} \begin{pmatrix} c^\dagger_{A\downarrow} \\ c^\dagger_{B\downarrow} \\ c^\dagger_{C\uparrow} \\ c^\dagger_{A\uparrow} \\ c^\dagger_{B\uparrow} \\ c^\dagger_{C\downarrow} \end{pmatrix} + \text{h.c.}$$

where the momentum indices are implicit. The block diagonal form of $\Delta^{\text{Calc}}_{\mathbf{k},a_1,s_1,a_2,s_2}$ arises from the mirror symmetry M_z discussed in Chapter 3.

As a result of the calculations described in Chapter 2 and 3, we obtained $d^{\text{Calc}}_{z,\mathbf{k},\alpha}$ at the FSs. We can therefore compute $\Delta^{\text{Calc}}_{\mathbf{k},a_1,s_1,a_2,s_2}$ numerically at the Fermi surface by using Eq. 4.19. In order to perform lattice BdG calculations, it will be advantageous to generate an order parameter $\Delta^{\text{Fit}}_{\mathbf{k},a_1,s_1,a_2,s_2}$ which approximately fits $\Delta^{\text{Calc}}_{\mathbf{k},a_1,s_1,a_2,s_2}$ at the Fermi surface and that can be expressed in terms of a few lattice harmonics. Since the inter-orbital ($a_1 \neq a_2$) terms in $\Delta^{\text{Calc}}_{\mathbf{k},a_1,s_1,a_2,s_2}$ were found numerically to be comparatively smaller, we assume for the sake of simplicity that $\Delta^{\text{Fit}}_{\mathbf{k},a_1,s_1,a_2,s_2} \propto \delta_{a_1,a_2}$. Furthermore, From Eq. 4.19 and the explicit matrix form given above, one finds

$$\begin{aligned} \Delta^{\text{Calc}}_{\mathbf{k},a,\uparrow,a,\uparrow} &= \Delta^{\text{Calc}}_{\mathbf{k},a,\downarrow,a,\downarrow} = 0 \\ \Delta^{\text{Calc}}_{\mathbf{k},a,\uparrow,a,\downarrow} &= \Delta^{\text{Calc}}_{\mathbf{k},a,\downarrow,a,\uparrow} \neq 0. \end{aligned} \tag{4.21}$$

Based on these relations, we introduce

$$\Delta^{\text{Fit}}_{\mathbf{k},a_1,s_1,a_2,s_2} \equiv \delta_{a_1,a_2}\delta_{s_1,-s_2} d^{\text{Fit}}_{z,\mathbf{k},a} \tag{4.22}$$

with

$$d^{\text{Fit}}_{z,\mathbf{k},a} = \sum_{j=1,2,3} \Delta_{a,x,j}\ g_{x,j}(\mathbf{k}) + i\ \Delta_{a,y,j}\ g_{y,j}(\mathbf{k}) \tag{4.23}$$

as an ansatz to fit $\Delta^{\text{Calc}}_{\mathbf{k},a_1,s_1,a_2,s_2}$. The lattice harmonics are given by

$$\begin{aligned} g_{x,1}(\mathbf{k}) &= \sin(k_x) \\ g_{x,2}(\mathbf{k}) &= \sin(k_x)\cos(k_y) \\ g_{x,3}(\mathbf{k}) &= \sin(3k_x) \\ g_{y,j}(k_x,k_y) &= g_{x,j}(k_y,k_x) \end{aligned} \tag{4.24}$$

and $\Delta_{a,x,j}$ and $\Delta_{a,y,j}$ are fitting parameters subject to the following constraints:

$$\begin{aligned} \Delta_{B,y,j} &= \Delta_{A,x,j} \\ \Delta_{A,y,j} &= \Delta_{B,x,j} = 0 \\ \Delta_{C,x,j} &= \Delta_{C,y,j}. \end{aligned} \tag{4.25}$$

Asking for $\Delta^{\text{Fit}}_{\mathbf{k},a_1,s_1,a_2,s_2} \simeq \Delta^{\text{Calc}}_{\mathbf{k},a_1,s_1,a_2,s_2}$ for $\mathbf{k}$ at the Fermi surface, we find the best fit for

$$\begin{aligned} &(\Delta^{\text{Fit}}_{A,x,1}, \Delta^{\text{Fit}}_{A,x,2}, \Delta^{\text{Fit}}_{A,x,3}) = (0, 0.2, 1) \\ &(\Delta^{\text{Fit}}_{B,y,1}, \Delta^{\text{Fit}}_{B,y,2}, \Delta^{\text{Fit}}_{B,y,3}) = (0, 0.2, 1) \\ &(\Delta^{\text{Fit}}_{C,x,1}, \Delta^{\text{Fit}}_{C,x,2}, \Delta^{\text{Fit}}_{C,x,3}) = (\Delta^{\text{Fit}}_{C,y,1}, \Delta^{\text{Fit}}_{C,y,2}, \Delta^{\text{Fit}}_{C,y,3}) = (0.18, 0.15, -0.3). \end{aligned} \tag{4.26}$$

We give an illustration of these two order parameters after having transformed them back to band space in Fig. 4.1(c-d).

4.3 Implications for experiments

Possible experimental implications of a higher Chern number are now discussed. First, C gives the number of branches of chiral Majorana modes that can be found at sample edges and at dislocations with a Burgers vector whose component along $\langle 001 \rangle$ is non-zero[145, 146]. This could lead to specific signatures in tunnelling measurements [9, 78, 147] and edge state spectroscopy using angle-resolved photoemission spectroscopy. These chiral Majorana modes lead to a quantization of the low temperature thermal

Table 4.1: Chern numbers and Ginzburg-Landau coefficients (arbitrary units) for the two order parameters studied in this work

OP	$C_{\boldsymbol{\alpha}}$	$C_{\boldsymbol{\beta}}$	$C_{\boldsymbol{\gamma}}$	C	$k_{3,\boldsymbol{\alpha}}$	$k_{3,\boldsymbol{\beta}}$	$k_{3,\boldsymbol{\gamma}}$	$\overline{k_3}$
d_z^{Naive}	-1	1	1	1	0.50	0.99	1.14	1.0
d_z^{Calc}	-1	-3	-3	-7	-0.04	0.07	-0.14	-0.06

Hall conductance, whose value is proportional to C [38, 148]:

$$K_{xy} = \frac{C}{2}\frac{\pi^2 k_B^2 T}{6\pi\hbar}, \tag{4.27}$$

where k_B is Boltzmann constant and T is the temperature. The fact that this quantity differs both in magnitude (by a factor of 7) and in sign between the cases of d_z^{Naive} and d_z^{Calc} provides a strong motivation to realise this experiment.

4.3.1 Charge currents - Ginzburg-Landau

We now discuss implications for edge currents in Sr_2RuO_4. Since charge is not conserved in a superconductor, the charge Hall conductance G_{xy} is not universal and depends on the microscopic details, unlike K_{xy}. In a rotationally invariant system, there is only one possible angular dependence of the gap for a given value of C: $d_z \propto e^{i\theta C}$, where $\theta = \arctan(p_y/p_x)$ is the polar angle. Taking advantage of this, it was shown that having edge currents and a total orbital angular momentum "of order one" is inevitable for a $|C| = 1$ chiral superfluid in a rotationally invariant system [137–140]. On the contrary, these two quantities were shown to vanish in the case of $|C| > 1$ [137–140]. These results apply to a sharp edge, i.e. an edge potential that increases over a length scale much smaller than the coherence length, which is the regime expected to be relevant to experiments. As pointed out in Refs [139, 140], for smooth enough edge potential (which is not expected to be physically relevant), the edge currents are never suppressed for any non-zero Chern number.

When lattice effects cannot be neglected, like for Sr_2RuO_4, there are lots of possible OPs for a given Chern number, and the aforementioned dichotomy present in the continuum breaks down. In this case, the magnitude of edge currents can vary greatly

from one OP to the other, even if they have the same Chern number. In order to estimate the edge currents for the different OPs discussed in this work, we follow the Ginzburg-Landau (GL) calculation given in Ref. [139, 140] (see also Refs. [87, 134, 149–151]). In this theory, it can be shown that, for an edge along $\langle 100 \rangle$ (or $\langle 010 \rangle$), the current density coming from band ν is proportional to the following coefficient

$$k_{3,\nu} \propto \langle h_{x,\nu}(\mathbf{k}) h_{y,\nu}(\mathbf{k}) v_{x,\nu}(\mathbf{k}) v_{y,\nu}(\mathbf{k}) \rangle_{\mathrm{FS}_\nu} \tag{4.28}$$

where h_x and h_y are the dimensionless p_x and p_y components of the $p_x + ip_y$ OP and $v_{x,y}$ are the Fermi velocity components and the average is over the FS of band ν.

As shown in Ref. [139], the dichotomy between $|C| = 1$ and $|C| > 1$ in rotationally invariant systems can be easily understood from the above formula for k_3: the Fermi surface average vanishes identically for $|C| > 1$. In a rotationally invariant system, one has $v_x \propto \cos(\theta)$, $v_y \propto \sin(\theta)$, $h_x \propto \cos(C\theta)$ and $h_y \propto \sin(C\theta)$, where $\theta = \arctan(p_y/p_x)$. The Fermi surface average is then simply an integral over θ, which vanishes for $|C| > 1$.

The total current is proportional to the average of the $k_{3,\nu}$ coefficients weighted by the respective density of states at the Fermi level: $\overline{k_3} = (1/\rho) \times \sum_\nu \rho_\nu k_{3,\nu}$. In Table 4.1, we give the values of $k_{3,\nu}$ and $\overline{k_3}$ for d_z^{Naive} and d_z^{Calc}. We find that $\overline{k_3}$ is reduced by a factor of roughly 20 for d_z^{Calc} compared to d_z^{Naive}.

4.3.2 Charge currents - Bogolyubov-de Gennes

Since the gap d_z^{Calc} has deep minima, it is expected that finite temperature effects should lead to a large current reduction over a temperature scale set by this gap minima. In order to estimate this effect for d_z^{Calc}, we performed a Bogoliubov-de Gennes (BdG) calculation on a square lattice in a cylinder geometry with open boundary conditions along x and periodic boundary conditions along y.

4.3.2.1 Model

In a system with periodic boundary conditions along both directions, the Hamiltonian would read

$$H = H_K + H_\Delta = \sum_{\mathbf{k},a_1,a_2,s_1,s_2} h_{\mathbf{k},a_1,s_1,a_2,s_2} c^\dagger_{\mathbf{k},a_1,s_1} c_{\mathbf{k},a_2,s_2} + \left(\sum_{\mathbf{k},a_1,a_2,s_1,s_2} \Delta^{\text{Fit}}_{\mathbf{k},a_1,s_1,a_2,s_2} c^\dagger_{\mathbf{k},a_1,s_1} c^\dagger_{-\mathbf{k},a_2,s_2} + \text{h.c.} \right) \tag{4.29}$$

where $h_{\mathbf{k},a_1,s_1,a_2,s_2}$ includes the hoppings, the chemical potential and spin-orbit coupling and was given explicitly in Chapter 3 and $\Delta^{\text{Fit}}_{\mathbf{k},a_1,s_1,a_2,s_2}$ is the fitted gap introduced previously. We use the fitted gap because it is conveniently expressed as a sum of three lattice harmonics $g_{1,2,3}(\mathbf{k})$, which will lead in real space to pairing terms with three different neighbors: nearest-neighbor, next-to-nearest neighbor, and the neighbors at a distance of three sites along x or y. In order to implement open boundary conditions along x, we use the Fourier transform

$$c^\dagger_{x,k_y,a,s} = \frac{1}{\sqrt{L}} \sum_{k_x} e^{-ik_x x} c^\dagger_{k_x,k_y,a,s} \tag{4.30}$$

and we set to zero the hopping and pairing terms that would include operators with x outside the domain $[1, L]$.

After implementing this procedure, we find the pairing term for open boundary

conditions along x. It is given by $H_\Delta^{\mathrm{OBC}} = \sum_{k_y} H_\Delta(k_y)$ with

$$\begin{aligned} H_\Delta(k_y) = &\sum_a h^\Delta_{a,0}(k_y) \sum_{x=1,\dots,L} c^\dagger_{x,k_y,a,s_a} c^\dagger_{x,-k_y,a,-s_a} \\ &+ \sum_a h^\Delta_{a,+1}(k_y) \sum_{x=1,\dots,L-1} c^\dagger_{x,k_y,a,s_a} c^\dagger_{x+1,-k_y,a,-s_a} \\ &+ \sum_a h^\Delta_{a,-1}(k_y) \sum_{x=2,\dots,L} c^\dagger_{x,k_y,a,s_a} c^\dagger_{x-1,-k_y,a,-s_a} \\ &+ \sum_a h^\Delta_{a,+3}(k_y) \sum_{x=1,\dots,L-3} c^\dagger_{x,k_y,a,s_a} c^\dagger_{x+3,-k_y,a,-s_a} \\ &+ \sum_a h^\Delta_{a,-3}(k_y) \sum_{x=4,\dots,L} c^\dagger_{x,k_y,a,s_a} c^\dagger_{x-3,-k_y,a,-s_a} \\ &+ \text{h.c.} \end{aligned} \tag{4.31}$$

with $s_a = 1$ for $a = A, B$ and $s_a = -1$ for $a = C$ and with

$$\begin{aligned} h^\Delta_{a,0}(k_y) &= \Delta_{a,y,1} i \sin(k_y) + \Delta_{a,y,3} i \sin(3k_y) \\ h^\Delta_{a,+1}(k_y) &= \Delta_{a,x,1} \frac{-i}{2} + \Delta_{a,x,2} \frac{-i}{2} \cos(k_y) + \Delta_{a,y,2} \frac{1}{2} i \sin(k_y) \\ h^\Delta_{a,-1}(k_y) &= \Delta_{a,x,1} \frac{i}{2} + \Delta_{a,x,2} \frac{i}{2} \cos(k_y) + \Delta_{a,y,2} \frac{1}{2} i \sin(k_y) \\ h^\Delta_{a,+3}(k_y) &= \Delta_{a,x,3} \frac{-i}{2} \\ h^\Delta_{a,-3}(k_y) &= \Delta_{a,x,3} \frac{i}{2}. \end{aligned} \tag{4.32}$$

For the sake of simplicity, we do not impose self-consistency and instead impose a uniform gap for which the overall magnitude is given by the BCS formula [42]

$$\eta(T) \simeq \Delta(0) \sqrt{1 - \frac{T}{T_c}} \tag{4.33}$$

where $\Delta(0)$ was computed in Chapter 2. The gap parameters are therefore given by:

$$\begin{aligned}
(\Delta^{\mathrm{Fit}}_{A,x,1}, \Delta^{\mathrm{Fit}}_{A,x,2}, \Delta^{\mathrm{Fit}}_{A,x,3}) &= \eta(T)(0, 0.2, 1) \\
(\Delta^{\mathrm{Fit}}_{B,y,1}, \Delta^{\mathrm{Fit}}_{B,y,2}, \Delta^{\mathrm{Fit}}_{B,y,3}) &= \eta(T)(0, 0.2, 1) \\
(\Delta^{\mathrm{Fit}}_{C,x,1}, \Delta^{\mathrm{Fit}}_{C,x,2}, \Delta^{\mathrm{Fit}}_{C,x,3}) &= \eta(T)(0.18, 0.15, -0.3) \\
(\Delta^{\mathrm{Fit}}_{C,y,1}, \Delta^{\mathrm{Fit}}_{C,y,2}, \Delta^{\mathrm{Fit}}_{C,y,3}) &= \eta(T)(0.18, 0.15, -0.3).
\end{aligned} \tag{4.34}$$

We will compare this case with the the fully gapped, $C = 1$ case given by d_z^{Naive}. This case can be well approximated in orbital space by nearest-neighbour pairing on all three orbitals:

$$\begin{aligned}
(\Delta^{\mathrm{Naive}}_{A,x,1}, \Delta^{\mathrm{Naive}}_{A,x,2}, \Delta^{\mathrm{Naive}}_{A,x,3}) &= \eta(T)(1, 0, 0) \\
(\Delta^{\mathrm{Naive}}_{B,y,1}, \Delta^{\mathrm{Naive}}_{B,y,2}, \Delta^{\mathrm{Naive}}_{B,y,3}) &= \eta(T)(1, 0, 0) \\
(\Delta^{\mathrm{Naive}}_{C,x,1}, \Delta^{\mathrm{Naive}}_{C,x,2}, \Delta^{\mathrm{Naive}}_{C,x,3}) &= \eta(T)(-1, 0, 0) \\
(\Delta^{\mathrm{Naive}}_{C,y,1}, \Delta^{\mathrm{Naive}}_{C,y,2}, \Delta^{\mathrm{Naive}}_{C,y,3}) &= \eta(T)(-1, 0, 0).
\end{aligned} \tag{4.35}$$

As shown in Eq. 3.1, the term H_K includes a hopping part and a spin-orbit coupling part, $H_K = H_{\mathrm{Hop}} + H_{\mathrm{SOC}}$. Since the spin-orbit coupling is an on-site term, it is not affected by the boundary conditions and can be used as such. The hopping terms are transposed to open boundary conditions using the same procedure as before, $H^{\mathrm{OBC}}_{\mathrm{Hop}} = \sum_{k_y} H_{\mathrm{Hop}}(k_y)$:

$$\begin{aligned}
H_{\mathrm{Hop}}(k_y) = &\sum_a h^{\mathrm{Hop}}_{a,0}(k_y) \sum_{x=1,\ldots,L} (c^\dagger_{x,k_y,a,\uparrow} c_{x,k_y,a,\uparrow} + c^\dagger_{x,k_y,a,\downarrow} c_{x,k_y,a,\downarrow}) \\
&+ \left(\sum_{a_1,a_2} h^{\mathrm{Hop}}_{a_1,a_2,+1}(k_y) \sum_{x=1,\ldots,L-1} (c^\dagger_{x,k_y,a_1,\uparrow} c_{x+1,k_y,a_2,\uparrow} + c^\dagger_{x,k_y,a_1,\downarrow} c_{x+1,k_y,a_2,\downarrow}) + \mathrm{h.c.} \right)
\end{aligned} \tag{4.36}$$

with the non-zero elements of $h^{\text{Hop}}_{a,0}(k_y)$ and $h^{\text{Hop}}_{a_1,a_2,+1}(k_y)$ given by

$$\begin{aligned}
h^{\text{Hop}}_{A,0}(k_y) &= -2t^{\perp}\cos(k_y) - \mu \\
h^{\text{Hop}}_{B,0}(k_y) &= -2t\cos(k_y) - \mu \\
h^{\text{Hop}}_{C,0}(k_y) &= -2t'\cos(k_y) - \mu_C \\
h^{\text{Hop}}_{A,A,+1}(k_y) &= -t \\
h^{\text{Hop}}_{B,B,+1}(k_y) &= -t^{\perp} \\
h^{\text{Hop}}_{C,C,+1}(k_y) &= -t' - 2t''\cos(k_y) \\
h^{\text{Hop}}_{A,B,+1}(k_y) &= h_{B,A,+1}(k_y) = 2it'''\sin(k_y).
\end{aligned} \tag{4.37}$$

4.3.2.2 Current

In this section, we will use a real space basis in both directions and we will consider only one spin species and therefore omit the spin index. The creation operator in this basis is given by $c^{\dagger}_{\vec{x},a}$ with $\vec{x} = x\ \hat{x} + y\ \hat{y}$, with $x = 1, \ldots, L$ and $y \in \mathbb{Z}$ and where $\hat{x}$ and $\hat{y}$ are the unit vectors. Since we only consider one spin species, the current we obtain should be multiplied by 2 to obtain the total current.

Consider a generic hopping model given by

$$H_{\text{Hop}} = \sum_{a_1,a_2}\sum_{\vec{\delta}} t_{\vec{\delta},a_1,a_2} \sum_{\vec{x}} c^{\dagger}_{\vec{x},a_1} c_{\vec{x}+\vec{\delta},a_2}, \tag{4.38}$$

with $t_{\vec{\delta},a_1,a_2} = t^{*}_{-\vec{\delta},a_2,a_1}$ to ensure hermiticity. The operator for the current flowing between two sites $\vec{x}_1$ and $\vec{x}_2$ is given by [152]

$$\begin{aligned}
\vec{j}_{\vec{x}_1,\vec{x}_2} &= i(\vec{x}_2 - \vec{x}_1)\sum_{a_1,a_2}\left(t_{\vec{x}_2-\vec{x}_1,a_1,a_2} c^{\dagger}_{\vec{x}_1,a_1} c_{\vec{x}_2,a_2} - t_{\vec{x}_1-\vec{x}_2,a_2,a_1} c^{\dagger}_{\vec{x}_2,a_2} c_{\vec{x}_1,a_1}\right) \\
&= -2(\vec{x}_2 - \vec{x}_1)\sum_{a_1,a_2} \text{Im}\left[t_{\vec{x}_2-\vec{x}_1,a_1,a_2} c^{\dagger}_{\vec{x}_1,a_1} c_{\vec{x}_2,a_2}\right].
\end{aligned} \tag{4.39}$$

Note that $\vec{j}_{\vec{x}_1,\vec{x}_2} = \vec{j}_{\vec{x}_2,\vec{x}_1}$.

In a cylindrical geometry, spontaneous currents will flow towards, say, negative y at the left edge (i.e. close to $x = 1$) and towards positive y at the right edge

(i.e. close to $x = L$). These currents are localized at the edge within a length scale that is roughly given by the coherence length, which scales like t/Δ. We choose L much larger than the coherence length so that the two edges do not interact with each other. We then compute the integrated current over the left half of the cylinder $[1, L/2]$ in order to isolate the contribution from one edge only. We only calculate the y component of the total current, as its x component vanishes by symmetry. This current operator is given by

$$\begin{aligned}\hat{I} = &-2 \sum_{n=1,\ldots,L/2} \mathrm{Im} \left[\sum_a t_{\hat{y},a,a} c^\dagger_{n\hat{x},a} c_{n\hat{x}+\hat{y},a} \right] \\ &- 2 \sum_{n=1,\ldots,L/2} \mathrm{Im} \left[\sum_{a_1,a_2} \left(t_{\hat{x}+\hat{y},a_1,a_2} c^\dagger_{n\hat{x},a_1} c_{n\hat{x}+\hat{x}+\hat{y},a_2} + t_{-\hat{x}+\hat{y},a_1,a_2} c^\dagger_{n\hat{x},a_1} c_{n\hat{x}-\hat{x}+\hat{y},a_2} \right) \right]\end{aligned} \tag{4.40}$$

where the terms including operators with x outside the domain $[1, L/2]$ should be set to zero and where the non-zero hoppings are given by

$$\begin{aligned} t_{\hat{y},A,A} &= t^\perp \\ t_{\hat{y},B,B} &= t \\ t_{\hat{y},C,C} &= t' \\ t_{\hat{x}+\hat{y},C,C} &= t_{-\hat{x}+\hat{y},C,C} = t'' \\ t_{\hat{x}+\hat{y},A,B} &= -t_{-\hat{x}+\hat{y},A,B} = t''' \\ t_{\hat{x}+\hat{y},B,A} &= -t_{-\hat{x}+\hat{y},B,A} = t'''. \end{aligned} \tag{4.41}$$

Finally, we compute $I = \langle \hat{I} \rangle$ where the brackets indicate a thermal average for the Hamiltonian $H^{\mathrm{OBC}} = H^{\mathrm{OBC}}_{\mathrm{Hop}} + H^{\mathrm{OBC}}_{\Delta}$. The Bogolyubov transformation that diagonalizes this Hamiltonian is easily found numerically for system sizes up to $L \sim 1250$.

In Fig. 4.2, we show the spontaneous currents I_{Naive} and I_{Fit} for Δ^{Naive} and Δ^{Fit}, respectively. We find that (1) at zero temperature, I_{Fit} is reduced by a factor of 30 compared to I_{Naive}, in overall agreement with the Ginzburg-Landau result; (2) unlike in the case of d_z^{Naive}, finite temperature effects generate a large drop in current in the case of d_z^{Calc}. We emphasize that this reduction should be very robust and appear

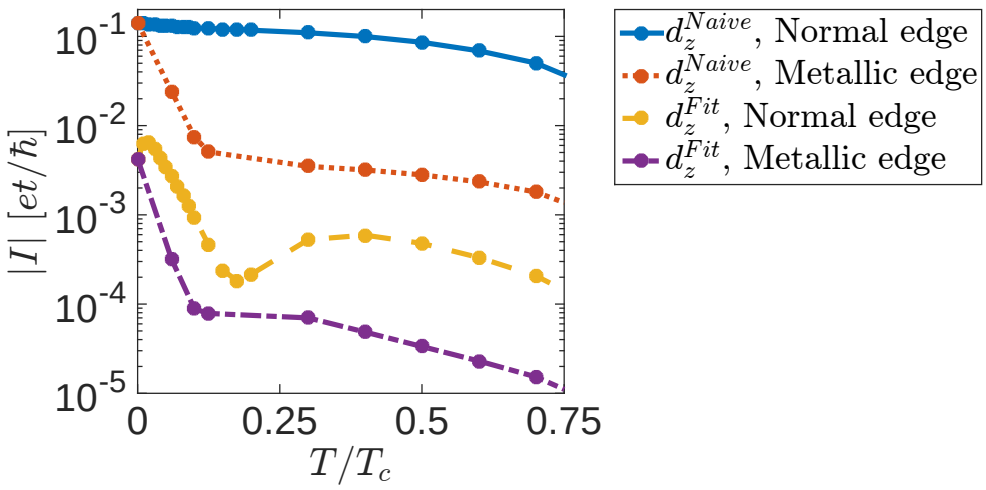

Figure 4.2: Spontaneous currents I_{Naive} and I_{Fit} for the gap functions d_z^{Naive} and d_z^{Calc}, respectively, as calculated from BdG. A superconducting region of width $L = 750$ sites was taken in which the gap takes a uniform value given by $T_c = 0.01t$. In the metallic edge case, a region of width $L_M = 500$ sites was added at the edge in which the gap is set to zero.

both at edges and domain walls, since it comes from an intrinsic property of the bulk superconducting state.

There are other proposals for edge currents reduction [136, 150, 151, 153–155] that could combine with the present one. In particular, the fact that sample edges are metallic, as observed by in-plane tunneling spectroscopy [78], was shown to generate a large reduction in predicted edge currents[151]. Following Ref. [151], we model the metallic edge by a region of width L_M sites where the gap is set to zero. As shown in Fig. 4.2, the presence of a metallic edge generates an even larger drop of the current over a temperature scale given by $T/T_c \sim \xi/L_M$, with ξ the coherence length.

Experimental data[80, 81, 130] restricts edge currents to be three orders of magnitude smaller than the Matsumoto-Sigrist prediction obained for d_z^{Naive} [79], which is of the same order as the value we find for I_{Naive} at $T = 0$. As seen in Fig. 4.2, the current predicted for d_z^{Calc} at the temperature relevant to experiments ($T/T_c = 0.2$) is roughly three orders of magnitude smaller than I_{Naive} at $T = 0$. This prediction could therefore potentially explain the absence of measurable edge currents generated fields.

4.4 Conclusion

In conclusion, we have shown from a microscopic calculation that a chiral state whose two dominant gap functions are $\sin(3k_x) + i\sin(3k_y)$ and $\sin(k_x)\cos(k_y) + i\sin(k_y)\cos(k_x)$ is favored on the three bands of Sr_2RuO_4, at least in the weak coupling limit. This OP leads to a Chern number of -7, in contrast to the previously assumed value of $+1$. This state naturally predicts both time-reversal symmetry breaking and the possibility of a large reduction of edge currents, thereby helping to reconcile two sets of experiments: optical Kerr effect and muon spin relaxation on one side, and negative results obtained in the search for edge currents on the other. The present results could be an important piece of the puzzle in reconciling the absence of edge currents with the presence of a chiral superconducting state in Sr_2RuO_4.

Admittedly, the weak-coupling technique we used to predict d_z^{Calc} is exact only in the $U/t \to 0$ limit, while this ratio is finite for a realistic material. The gap in the real material will therefore be renormalized compared to d_z^{Calc}. Nevertheless, this gap function was shown to reproduce the specific heat data[144]. Furthermore, d_z^{Calc} has deep minima on $\boldsymbol{\alpha}$ and $\boldsymbol{\beta}$, as required by STM[9](the gap function on $\boldsymbol{\gamma}$ cannot be observed directly in STM because of atomic orbitals anisotropy). Also, finite coupling calculations have shown similar results: the pairing on $\boldsymbol{\gamma}$ was shown to have a substantial g_2 component from a singular-mode functional renormalization group (RG) calculation[55] and a large g_3 component was shown to be favored from a calculation combining RG with the constrained random phase approximation[63].

5. Strain

5.1 Introduction

One interesting property of unconventional superfluids and superconductors is their high sensitivity to relatively small variations of the properties of the system. For example, superfluid ^{3}He exhibits different superconducting phases under pressure and magnetic fields, like the A and the B phase discussed previously [27]. There is also some compelling evidence for a rich phase diagram under magnetic field for UPt_3, a heavy fermion compound that is another candidate for odd-parity superconductivity [156]. Finally, Sr_2RuO_4 is the most disorder-sensitive of all known superconductors [157].

It is therefore highly instructive to study the evolution of superconductivity in Sr_2RuO_4 under various perturbations. A common way of varying the electronic structure of unconventional superconductors is to use chemical doping, like in cuprates [24]. Sadly, the critical temperature of Sr_2RuO_4 drops very sharply with doping because of the disorder it induces [157]. Instead, it has been shown that uniaxial pressure can be used to tune the electronic structure without inducing disorder [10, 11]. In these experiments, uniaxial pressure is applied along specific crystal axes by using a piezoelectric apparatus and the critical temperature is determined by measuring the drop in mutual inductance between two coils due to the perfect diamagnetism of the superconducting sample [10, 11]. In this Chapter, we will discuss the evolution of superconductivity under uniaxial pressure along the direction $\langle 100 \rangle$ (direction a in Fig. 1.1). This is of course equivalent to the direction $\langle 010 \rangle$ since Sr_2RuO_4 is tetragonal.

We expect $\langle 100 \rangle$ uniaxial strain to have a non-trivial effect for two reasons. First, it breaks the $x \leftrightarrow y$ symmetry present in the D_{4h} tetragonal point group of the crystal, and therefore splits the degeneracy between the p_x and the p_y component of the order

Γ	$\mathbf{d}(\mathbf{k})$	Dimension	TRSB	Type
A_{1u}	$\hat{x}p_x + \hat{y}p_y$	1	No	Helical
A_{2u}	$\hat{x}p_y - \hat{y}p_x$	1	No	Helical
B_{1u}	$\hat{x}p_x - \hat{y}p_y$	1	No	Helical
B_{2u}	$\hat{x}p_y + \hat{y}p_x$	1	No	Helical
E_u	$\hat{z}(p_x \pm ip_y)$	2	Yes	Chiral

Table 5.1: Odd-parity irreducible representations of D_{4h}. TRSB stands for Time Reversal Symmetry Breaking. p_x (p_y) stands for any function of momentum that transforms like $\sin(k_x)$ ($\sin(k_y)$) under the symmetry operations.

Γ	$\mathbf{d}(\mathbf{k})$	Dimension	TRSB
A_{1u}	$\hat{x}p_x + \hat{y}p'_y$	1	No
B_{1u}	$\hat{x}p_y + \hat{y}p'_x$	1	No
B_{2u}	$\hat{z}p_x$	1	No
B_{3u}	$\hat{z}p_y$	1	No

Table 5.2: Odd-parity irreducible representations of D_{2h}. p_x (p_y) and p'_x (p'_y) stand for any function of momentum that transforms like $\sin(k_x)$ ($\sin(k_y)$) under the symmetry operations. The A_{1u} representation of D_{2h} results from the coupling between the A_{1u} and the B_{1u} representations of D_{4h}, the B_{1u} representation of D_{2h} results from the coupling between the A_{2u} and the B_{2u} representations of D_{4h}, and the B_{2u} and B_{3u} representations of D_{2h} arise from the splitting of the two components of the E_u representation of D_{4h}.

parameter. This degeneracy is required to form a $p_x \pm ip_y$ order parameter at T_c. As explained later, the behaviour of T_c at zero strain is expected to be qualitatively different for a chiral state than for a helical state (or for any other one-dimensional order parameter): there should be a cusp at zero strain for the chiral case, but no such cusp for a helical state [87]. While symmetry requires a cusp to be there, it does not say anything about its size. In this Chapter, we will use our microscopic calculation of T_c to estimate the size of the cusp and we will compare it with the experimental curve shown in Fig. 5.2.

Second, at a given strain ϵ_{vHS}, the $\boldsymbol{\gamma}$ band is expected to go through a Lifshitz transition, i.e. a topological change in the Fermi surface, and an associated Van Hove singularity (vHS) in its density of states. A Van Hove singularity is a singularity in the density of states when the Fermi level crosses an extremum or saddle point of the energy dispersion. The fact that a maximum of T_c was measured at a value of compressive strain that is in rough agreement with the value of ϵ_{vHS} predicted from

Γ	$\Delta_s(\mathbf{k})$	Dimension	TRSB
A_{1g}	1	1	No
A_{2g}	$p_x p_y(p_x^2 - p_y^2)$	1	No
B_{1g}	$p_x^2 - p_y^2$	1	No
B_{2g}	$p_x p_y$	1	No
E_g	$(p_x \pm i p_y)p_z$	2	Yes

Table 5.3: Even-parity irreducible representations of D_{4h}. p_x (p_y) stand for any function of momentum that transforms like $\sin(k_x)$ ($\sin(k_y)$) under the symmetry operations of D_{4h}. Note that E_g order parameters are zero in the $k_z = 0$ plane and could therefore not be studied with our two-dimensional model.

Γ	$\Delta_s(\mathbf{k})$	Dimension	TRSB
A_{1g}	1	1	No
B_{1g}	$p_x p_y$	1	No
B_{2g}	$p_x p_z$	1	No
B_{3g}	$p_y p_z$	1	No

Table 5.4: Even-parity irreducible representations of D_{2h}. p_x (p_y) stand for any function of momentum that transforms like $\sin(k_x)$ ($\sin(k_y)$) under the D_{2h} symmetry operations. The A_{1g} representation of D_{2h} results from the coupling between the A_{1g} and the B_{1g} representations of D_{4h}, the B_{1g} representation of D_{2h} results from the coupling between the A_{2g} and the B_{2g} representations of D_{4h}, and the B_{2g} and B_{3g} representations of D_{2h} arise from the splitting of the two components of the E_g representation of D_{4h}. Note that B_{2g} and B_{3g} order parameters are zero in the $k_z = 0$ plane and could therefore not be studied with our two-dimensional model.

DFT [11] seems to suggest that the Lifshitz transition was reached experimentally. In this Chapter, we give further evidence to this claim by showing from a microscopic calculation that T_c does exhibit a maximum at the vHS. Furthermore, our predicted curve of T_c versus strain is in good agreement with the experimental one over the entire range of strain reached in experiments.

5.2 Model

We assume that the most important change associated with strain is the change in the hopping parameters of the single-particle Hamiltonian H_K introduced in Chapter 3. For the sake of simplicity, we use a phenomenological approach whereby hopping parameters are simple functions of strain. We also assume that there is no rotation of the Oxygen octahedra due to the applied strain. For an applied strain ϵ along $\langle 100 \rangle$,

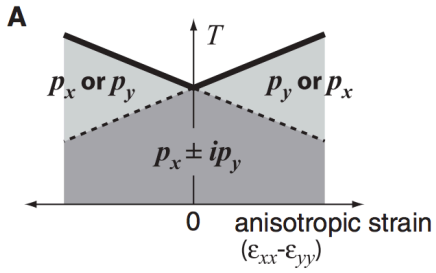

Figure 5.1: General phase diagram expected for $p_x \pm ip_y$ superconductivity in a tetragonal crystal subject to a $x \leftrightarrow y$ symmetry breaking strain. Reprinted figure with permission from Ref. [10]. Copyright 2016 by The American Association for the Advancement of Science.

the change in unit cell lengths is given by

$$\begin{aligned} a &\to a(1+\epsilon) \\ b &\to b(1-\nu\epsilon) \\ c &\to c(1-\nu_z\epsilon) \end{aligned} \tag{5.1}$$

where ν is the in-plane Poisson ratio and ν_z is the out-of-plane Poisson ratio and where positive (negative) ϵ corresponds to tensile (compressive) strain. The Poisson ratios were estimated in Ref.[10] to be $\nu \simeq 0.4$ and $\nu_z \simeq 0.2$. Since our model is two-dimensional, the change of the out-of-plane unit cell length c will be without consequences.

Hopping parameters decay exponentially with the distance l between atoms, $t = t_0 e^{-C(\frac{l}{l_0}-1)}$ with C a constant of order 1 that depends on the orbital, and t_0 the value of hopping for the distance without strain l_0 [158]. Using $\frac{l}{l_0} - 1 = \epsilon \ll 1$, we can linearise the above formula, leading to $t(\epsilon) = t_0(1 - C\epsilon)$. In the following, we will take into account the strain-induced change only for the nearest-neighbor hopping. We will also assume that the value of C is the same for all hoppings. Using this assumption, C can be absorbed into the definition of strain, $C\epsilon \to \epsilon$, and strain is therefore defined up to an overall scale. We will set that scale by fitting ϵ_{vHS} under compression in our model to the value coming from a DFT calculation [11]: $\epsilon_{vHS} \simeq -0.0075$.

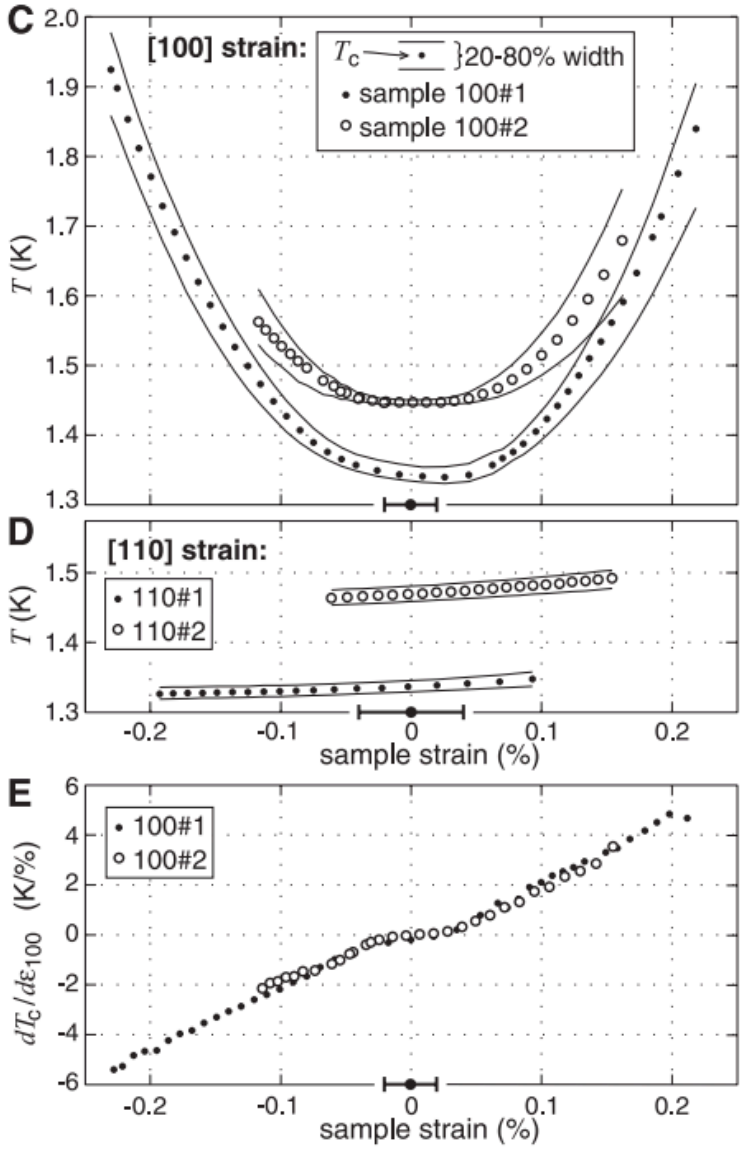

Figure 5.2: (C) T_c versus $\langle 100 \rangle$ strain for two different samples. The transition is detected by measuring the mutual inductance of two coils on top of the sample. The curve of mutual inductance versus T shows a plateau in the normal state, a rapid decrease at the transition, and another plateau in the superconducting phase. The value of T_c is chosen such that the mutual inductance is at 50% between the two plateaus. The temperatures at which the inductance is at 20% and 80% are plotted to give a measure of the transition width. (D) T_c versus $\langle 110 \rangle$ strain for two different samples. The study of $\langle 110 \rangle$ strain is left for future work. (E) $dT_c/d\epsilon$ for the data given in (C). Reprinted figure with permission from Ref. [10]. Copyright 2016 by The American Association for the Advancement of Science.

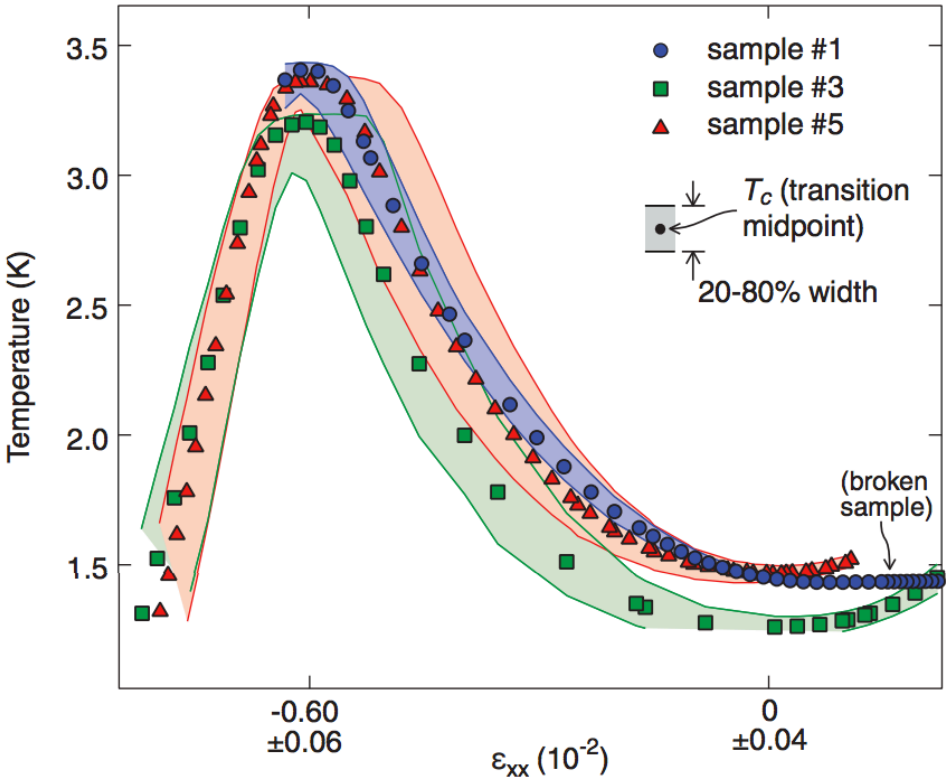

Figure 5.3: T_c versus $\langle 100 \rangle$ strain for three samples. Note that the range of compressive strain reached is larger than in Fig. 5.2. See legend of Fig. 5.2 for the meaning of the $20-80\%$ width. Reproduced from Ref. [11].

We can now write a strain-dependent hopping Hamiltonian $H_K(\epsilon)$:

$$H_K(\epsilon) = \sum_{\mathbf{k},s} \psi_s^\dagger(\mathbf{k}) h_s(\epsilon, \mathbf{k}) \psi_s(\mathbf{k}) \tag{5.2}$$

where $\psi_s(\mathbf{k}) = [c_{k,A,s}; c_{k,B,s}; c_{k,C,-s}]^T$ with $s = 1$ (-1) for up (down) spins. The matrix $h_s(\epsilon, \mathbf{k})$ is given by

$$h_s(\epsilon, \mathbf{k}) = \begin{pmatrix} E_A(\epsilon, \mathbf{k}) & E_{AB}(\mathbf{k}) - si\eta & i\eta \\ E_{AB}(\mathbf{k}) + si\eta & E_B(\epsilon, \mathbf{k}) & -s\eta \\ -i\eta & -s\eta & E_C(\epsilon, \mathbf{k}) \end{pmatrix} \tag{5.3}$$

where

$$\begin{aligned} E_A(\epsilon, \mathbf{k}) &= -2t_x(\epsilon)\cos(k_x) - 2t_y^\perp(\epsilon)\cos(k_y) - \mu(\epsilon) \\ E_B(\epsilon, \mathbf{k}) &= -2t_x^\perp(\epsilon)\cos(k_x) - 2t_y(\epsilon)\cos(k_y) - \mu(\epsilon) \\ E_C(\epsilon, \mathbf{k}) &= -2t_x'(\epsilon)\cos(k_x) - 2t_y'(\epsilon)\cos(k_y) - 4t''\cos(k_x)\cos(k_y) - \mu_C(\epsilon) \\ E_{AB}(\mathbf{k}) &= -4t'''\sin(k_x)\sin(k_y) \end{aligned} \tag{5.4}$$

and where A, B, C stand for the Ru orbitals $4d_{xz}$, $4d_{yz}$, $4d_{xy}$ on each lattice site. The spin-orbit coupling (SOC) parameter is η and the inter-orbital hopping term is $E_{AB}(\mathbf{k})$. The strain dependent hoppings are given by

$$\begin{aligned} t_x(\epsilon) &= t(1-\epsilon) \\ t_y(\epsilon) &= t(1+\nu\epsilon) \\ t_x^\perp(\epsilon) &= t^\perp(1-\epsilon) \\ t_y^\perp(\epsilon) &= t^\perp(1+\nu\epsilon) \\ t_x'(\epsilon) &= t'(1-\epsilon) \\ t_y'(\epsilon) &= t'(1+\nu\epsilon). \end{aligned} \tag{5.5}$$

The parameters at zero strain were already given in Chapter 3. They are reproduced

here for convenience: in dimensionless units,

$$(t, t^{\perp}, t', t'', \mu, \mu_C, t''', \eta) = (1.0, 0.1, 0.8, 0.3, 1.0, 1.1, 0.01, 0.1). \tag{5.6}$$

The chemical potentials are adjusted $\mu(\epsilon) = \mu + \delta\mu(\epsilon)$, $\mu_C(\epsilon) = \mu_C + \delta\mu(\epsilon)$ so that the filling $n \simeq 4/3$ remains unchanged by strain.

This hopping Hamiltonian reproduces qualitatively the results from DFT shown in Fig. 5.4: the $\boldsymbol{\gamma}$ band goes through a Lifshitz transition under both compressive and tensile strain. The Van Hove point located at $(0, \pi)$ (resp. $(\pi, 0)$) is crossed by the Fermi surface under compressive (resp. tensile) $\langle 100 \rangle$ strain. The DOS shows an increase with strain that is fairly symmetric around zero strain. A plot of the density of states from our hopping model is given in Fig. 5.5 and is in good agreement with the same plot obtained from DFT (see Fig. 5.4.C). In a strictly two-dimensional model like the one given by H_K, the DOS diverges logarithmically [106] and the only cutoff is given by discretization effects: the DOS is only computed for a finite number of value of the strain and the Fermi surface therefore never crosses exactly the Van Hove point. Instead, in 3D, the density of states does not diverge and the non-zero dispersion along the c axis therefore provides a cutoff. We chose the discretization in our 2D model such that the maximal increase in DOS at the vHS is of the same order as the one predicted from the 3D DFT calculations (see Fig 5.4).

Using the weak coupling scheme developed in Chapter 2, we can construct the pairing matrix for each value of strain, $g_{\mathbf{k}_\alpha, \mathbf{q}_\beta}(\epsilon)$, and diagonalize it to obtain the gap $\Delta_{\mathbf{k}_\alpha}(\epsilon)$ and the critical temperature $T_c(\epsilon)$ for each irreducible representation of the symmetry group. Writing the strain dependence explicitly and the pseudo-spin dependence implicitly, the main results of Chapter 2 are summarised as

$$\sum_{\beta} \int_{S_\beta(\epsilon)} \frac{d\mathbf{q}_\beta}{|S_\beta|} g_{\mathbf{k}_\alpha, \mathbf{q}_\beta}(\epsilon) \varphi_{\mathbf{q}_\beta}(\epsilon) = \lambda(\epsilon) \varphi_{\mathbf{k}_\alpha}(\epsilon) \tag{5.7}$$

with

$$T_c(\epsilon) = \mathcal{W} \exp\left(-\frac{1}{|\lambda(\epsilon)|}\right) \tag{5.8}$$

where λ is the most negative eigenvalue of g and $\mathcal{W}$ is of the order of the bandwidth. In the following, we will neglect the dependence of $\mathcal{W}$ on strain as the largest part of the strain-dependence comes from the exponential factor. The gap is proportional to the corresponding eigenvector:

$$\Delta_{\mathbf{k}_\alpha}(\epsilon) \propto \sqrt{\frac{v_{\mathbf{k}_\alpha}(\epsilon)}{\overline{v_\alpha}(\epsilon)\rho_\alpha(\epsilon)}}\varphi_{\mathbf{k}_\alpha}(\epsilon). \tag{5.9}$$

Before presenting the results of our calculation, we first discuss its validity. There are two main questions: (1) Is it a good approximation to write a Hamiltonian with a vanishingly small interaction to model a material for which the interaction is finite? (2) Once this Hamiltonian is written, do we find its correct solution by using the above scheme? We start by addressing point (2). The weak coupling technique is valid in the vanishing interaction limit as long as the particle-hole susceptibility χ is non-divergent. If χ diverges, instabilities different from BCS (charge and spin-density waves) can appear even in the weak coupling limit and the assumption of BCS being the only instability therefore breaks down [142]. This is the case in a strictly two-dimensional model at a vHS, since $\chi(\mathbf{k}=0)=\rho$ diverges [106]. In such case, the weak coupling calculation is correct arbitrarily close to the vHS (by making the interaction small enough), but not strictly at the vHS. Besides, if one actually takes into account the inter-layer coupling in Sr_2RuO_4 , one obtains a 3D system for which the density of states does not diverge at a vHS [106] and for which the weak coupling technique therefore works even at the vHS.

We now address point (1). There are two potential problems with assuming $U/t \to 0$. First, one might miss non-superconducting order parameters that are actually more favored than superconductivity but that require a finite coupling. In the case of unstrained Sr_2RuO_4, this is justified by the fact that no instability other than superconductivity was measured, unlike in cuprates or pnictides where charge and magnetic orders were measured. Since only a few experiments have been done so far on strained Sr_2RuO_4, the possibility of non-superconducting order parameters in this case cannot be ruled out from experiments and our assumption therefore has

admittedly less experimental support. Second, even if superconductivity is still the leading instability at finite interaction, the addition of finite coupling could potentially favour an order parameter of a different symmetry than the one favoured in the $U/t \to 0$ limit. Notwithstanding all this, weak coupling models are still very useful as a reference point that can be solved asymptotically exactly, and as a generator of candidates for superconducting order parameters that can be compared with experiments.

5.3 Results

As explained before, the eigenvectors of the pairing matrix are classified according to the irreducible representations of the point group. The point group goes from D_{4h} at zero strain (see Table 5.1) to D_{2h} at finite strain (see Table 5.2). D_{4h} is the tetragonal symmetry group and consists of a four-fold rotation axis along $\langle 001 \rangle$ and of three mirror planes normal to $\langle 100 \rangle$, $\langle 010 \rangle$ and $\langle 001 \rangle$. In contrast, D_{2h} is the orthorombic symmetry group and consists of a two-fold rotation axis along $\langle 001 \rangle$ and of three mirror planes normal to $\langle 100 \rangle$, $\langle 010 \rangle$ and $\langle 001 \rangle$. The two-dimensional $p_x \pm ip_y$ (E_u) representation is split by strain into two one-dimensional representations, p_x (B_{2u}) and p_y (B_{3u}), each with a different T_c. While the pairing eigenvalues $\lambda(\epsilon)$ for the p_x and p_y representations are degenerate at zero strain, they evolve independently with strain since the pairing matrix does not couple them. In other words, there is no level repulsion between them, and their crossing will therefore lead to a cusp in the experimental T_c, which is given by the maximum of $|\lambda|$ over all representations (see Fig. 5.1).

In Chapter 3 we found that, depending on the value of J/U, two odd-parity states consistent with specific heat measurements could be favored: either a chiral state ($\hat{z}(p_x \pm ip_y)$) at $J/U \sim 0.06$ or a helical state ($\hat{x}p_x + \hat{y}p_y$) at $J/U \sim 0.08$. We would like to study the evolution of T_c with strain for these two values of J/U. From the definition of g given in Chapter 2, one finds that the pairing matrix g can be written as $(U/t)^2\tilde{g}$ where $\tilde{g}$ depends only on J/U and not on U/t. This means that the gap

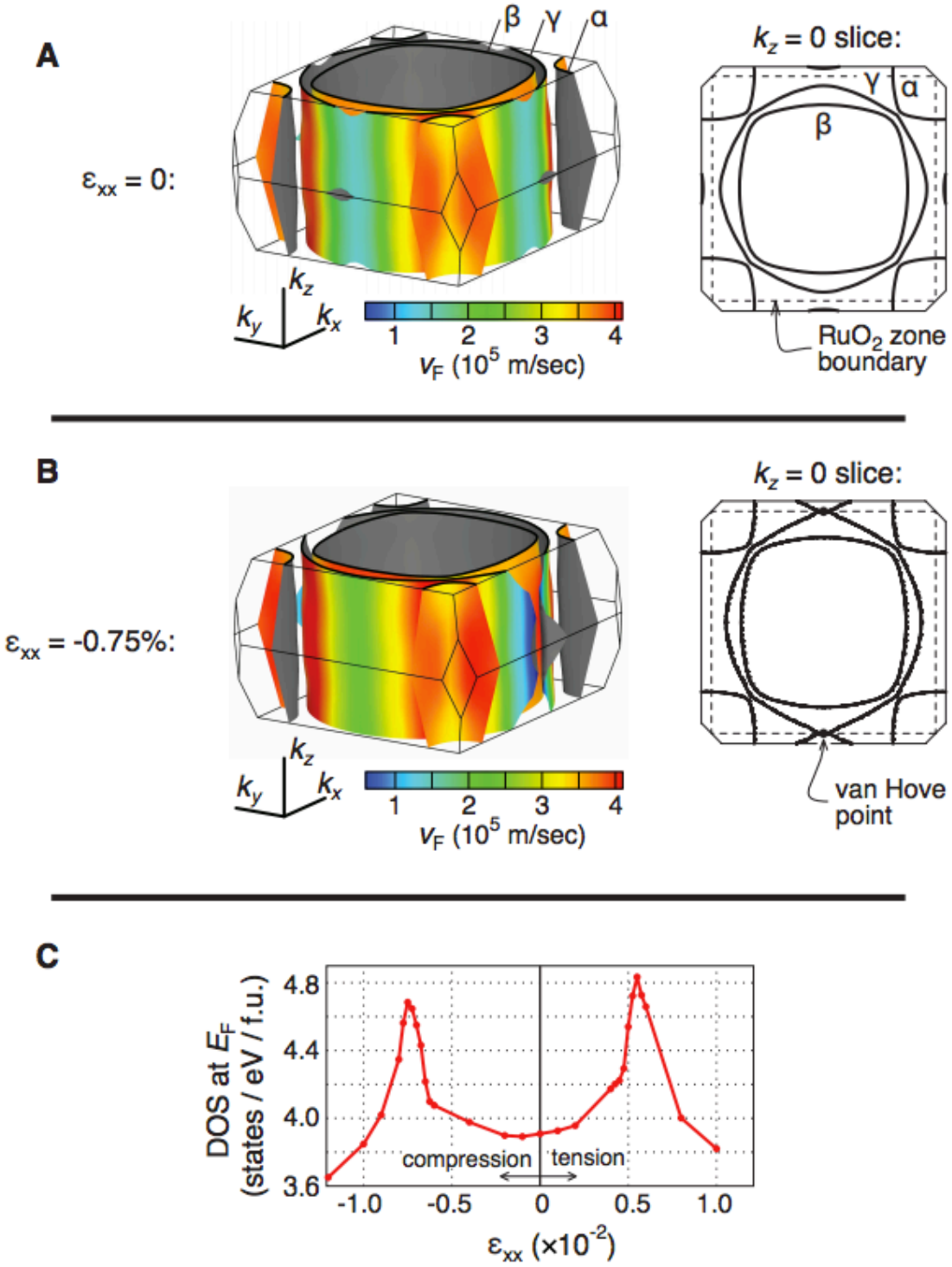

Figure 5.4: DFT calculation results from Ref. [11]. (A) Fermi surfaces of unstrained Sr_2RuO_4 coloured by the Fermi velocity v_F. A cross section through $k_z = 0$ is also shown. The dashed lines indicate the Brillouin zone of an isolated RuO_2 plane, which is the model we have used in this thesis. (B) Calculated Fermi surfaces at $\epsilon = -0.0075$. (C) Calculated density of states versus ϵ.

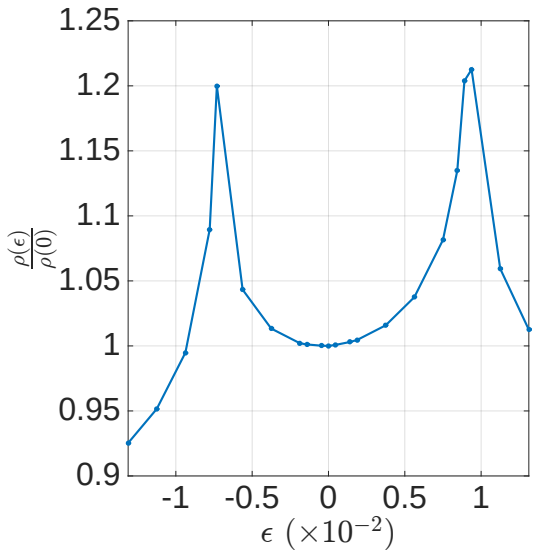

Figure 5.5: Relative increase in DOS with strain as calculated from our hopping model.

form factors $\varphi_{\mathbf{k}_\alpha}$, given by the eigenvectors of g, depend only on J/U and not on U/t. In contrast, the critical temperature is given by

$$T_c = \mathcal{W} \exp\left(\frac{-1}{\left(\frac{U}{t}\right)^2 |\tilde{\lambda}|}\right) \tag{5.10}$$

where $\tilde{\lambda}$ is an eigenvalue of $\tilde{g}$. One therefore needs to choose a value for $\mathcal{W}$ and U/t in order to calculate T_c. We take a phenomenological approach and choose these two parameters so as to fit two properties of the experimental curves shown in Fig. 5.3: $T_c(\epsilon = 0) \simeq 1.5$ K and $T_c(\epsilon = \epsilon_{vHS}) \simeq 3.5$ K. For $J/U = 0.06$, this leads to the following values: $U/t = 6.2$ and $\mathcal{W} = 22.1$ K. For $J/U = 0.08$, this leads to the following values: $U/t = 6.9$ and $\mathcal{W} = 18$ K.

5.3.1 Chiral case

We give in Fig. 5.6 the curves of T_c versus strain for the most favored even and odd-parity order parameters for $J/U = 0.06$. At zero strain, the highest-T_c odd-parity order parameter is in the $\hat{z}(p_x \pm ip_y)$ representation and the highest-T_c even-parity order parameter is in the B_{1g} representation of D_{4h} (see Table 5.3), also called $d_{x^2-y^2}$. At finite strain, the even-parity order parameter is in the A_{1g} representation of D_{2h}

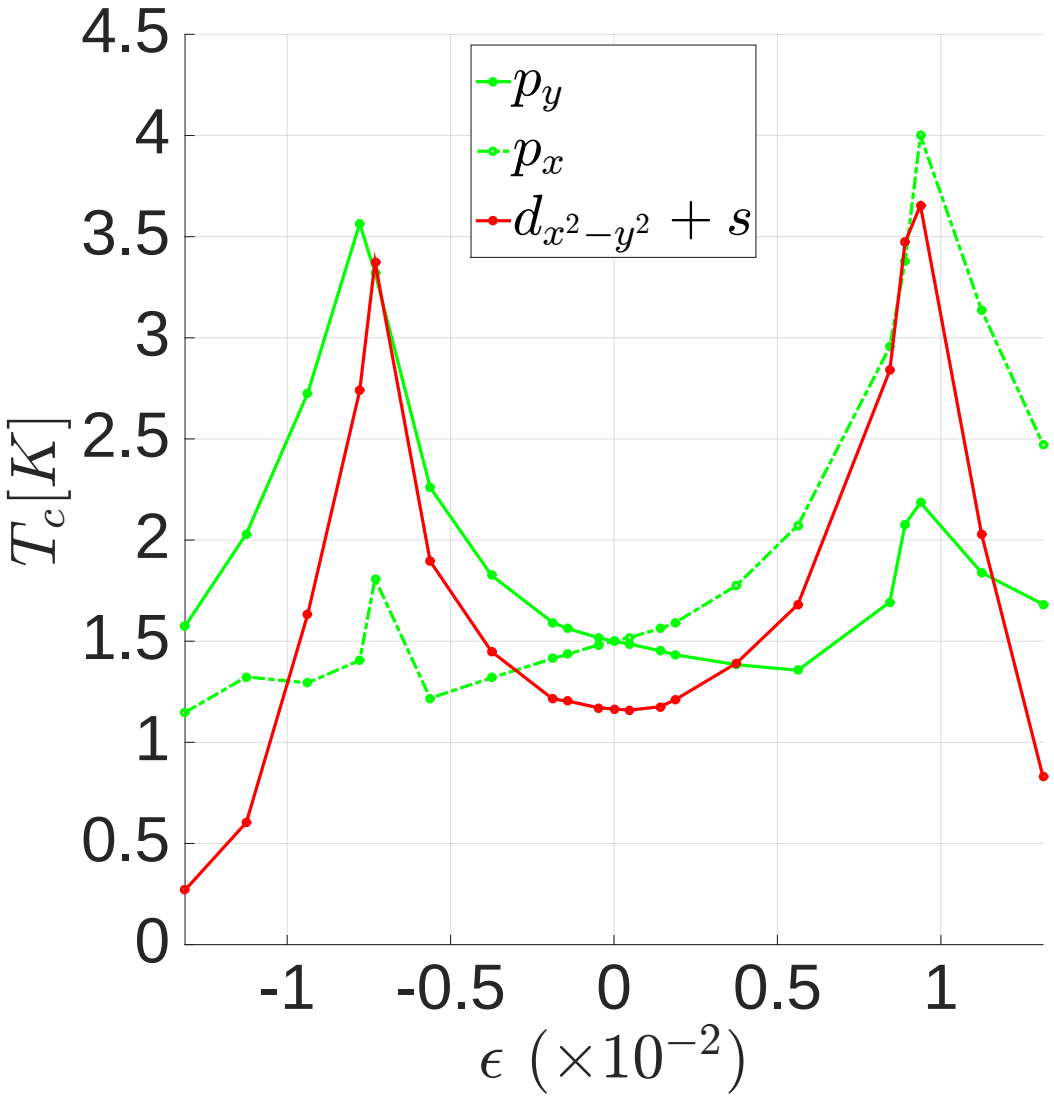

Figure 5.6: T_c versus strain for the two highest-T_c odd-parity order parameters and the highest-T_c even-parity order parameter for $J/U = 0.06$.

(see Table 5.4) and arises from the mixing of $d_{x^2-y^2}$ and of the trivial representation of D_{4h} (also called s). This gap is therefore denoted as $d_{x^2-y^2}+s$ in the following.

$p_y\hat{z}$ and $p_x\hat{z}$ are respectively the highest-T_c odd-parity order parameters under compression and tension: compression favours p_y because it increases the DOS on the sections of the FS where the p_y gap is the largest, and similarly for tension and p_x. T_c of the p_x and p_y components cross at zero strain, thereby leading to the cusp of T_c expected by symmetry. Yet, the small slope of the curves at zero strain leads to a very small cusp: $|dT_c/d\epsilon| \sim 0.3$ K/%. Although no cusp was seen in experiments (see Figure 5.2), the resolution of these experiments does not rule out a cusp of such a small magnitude. Furthermore, it was shown that this cusp can be rounded by fluctuations [7]. The source of this small $dT_c/d\epsilon$ at zero strain can be traced back to the flatness of the DOS at zero strain, as seen in Fig. 5.5.

For both even and odd-parity order parameters, the evolution of T_c is approximately symmetric between tensile and compressive strain and reaches a maximum at the Van Hove singularity. Even though the even-parity OP has a lower T_c at zero strain, its relative increase with strain is larger and it becomes a strong competitor for the highest-T_c close to the vHS. One should therefore consider the possibility of a phase transition at finite strain from odd-parity to even-parity superconductivity.

The momentum space structure of the order parameters at $\epsilon = 0$ and $\epsilon \simeq \epsilon_{vHS}$ is given in Fig. 5.7. For both parities, the structure of $\Delta(\mathbf{k})$ is quite complicated; one should remember that p_x and p_y are labels of irreducible representations and not accurate descriptions of the full gap structure. Concerning the behaviour of the gap close to the Van Hove point, there is a fundamental difference between even and odd-parity order parameters: in the odd-parity case, the gap at the Van Hove point $\mathbf{k}_{vHS} = (0, \pi)$ has to vanish, since $-\mathbf{k}_{vHS}$ is related to $\mathbf{k}_{vHS}$ by a reciprocal lattice vector. This prevents odd-parity order parameters from taking full advantage of the increased DOS close to the Van Hove point, and explains the larger relative increase of T_c for the even-parity OPs.

This effect can be quantified by looking at the upper critical field $H_{c,2}$ for fields along the c axis. Following Ref. [159], it is possible to compute the orbital-limited

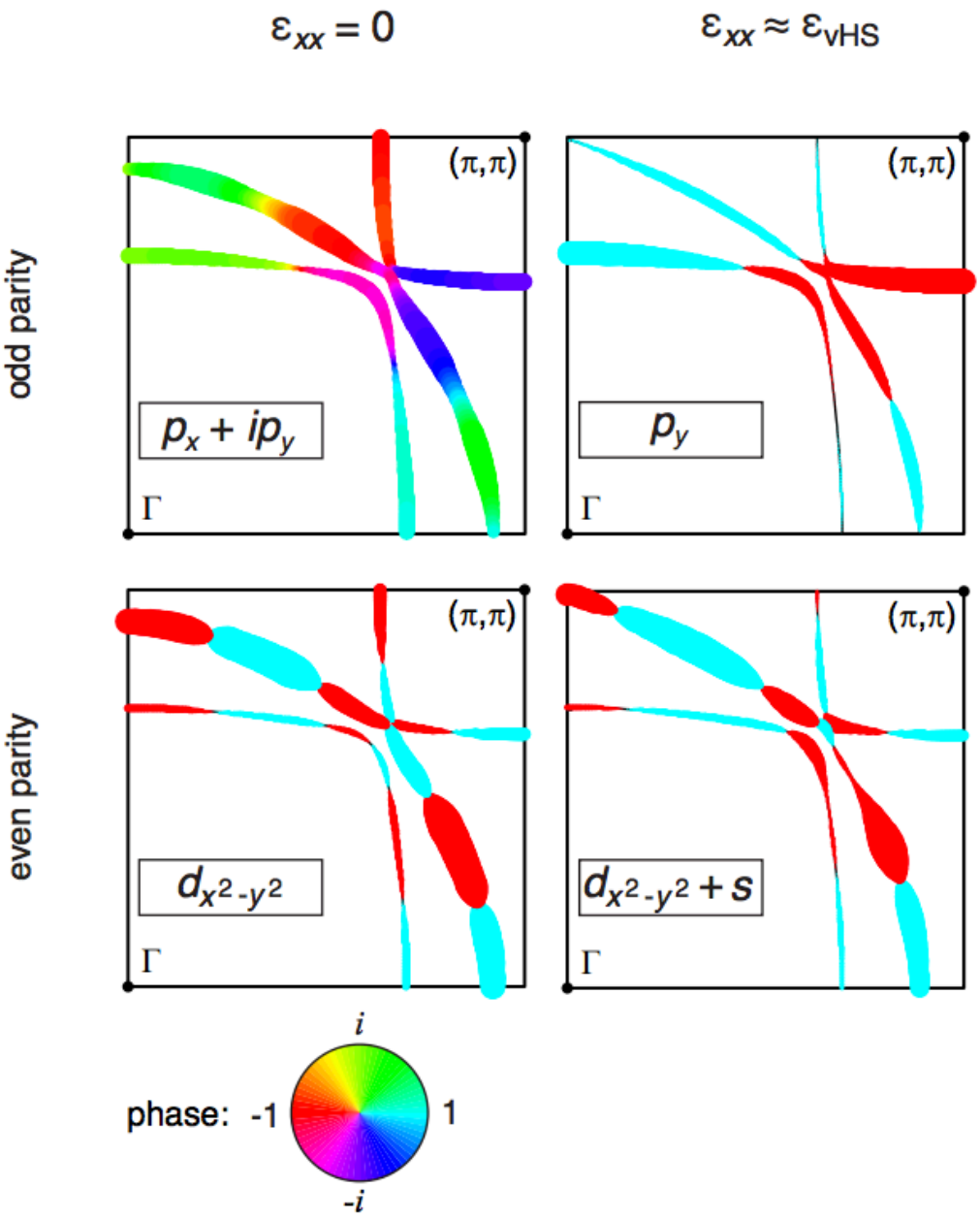

Figure 5.7: Order parameters for $J/U = 0.06$ at $\epsilon = 0$ and $\epsilon \simeq \epsilon_{vHS}$. The width of the traces is proportionnal to the gap magnitude and the color indicates the phase. The Van Hove point is located at $(0, \pi)$. Top: odd-parity order parameter $d_z(\mathbf{k})$. Bottom: even-parity order parameter $\Delta_s(\mathbf{k})$.

critical field at zero temperature in the quasi-classical limit. It is given by

$$H_{c,2} = 2\pi e^{-\gamma} \frac{\Phi_0}{\hbar^2} (k_B T_c)^2 \exp\left[-2 \sum_\alpha \int_{\mathrm{FS}_\alpha} \frac{d\mathbf{k}_\alpha}{S_{F,\alpha}} |\varphi_{\mathbf{k}_\alpha}|^2 \log(\tilde{v}_{\mathbf{k}_\alpha}) \right] \tag{5.11}$$

where $\gamma \simeq 0.577216$ is Euler's constant, Φ_0 is the flux quantum, k_B is Boltzmann constant, and

$$\tilde{v}_{\mathbf{k}_\alpha} = \sqrt{\chi_\alpha^{-1/2} v_{x,\mathbf{k}_\alpha}^2 + \chi_\alpha^{1/2} v_{y,\mathbf{k}_\alpha}^2} \tag{5.12}$$

with $\chi_\alpha = \overline{v_{x,\alpha}^2} / \overline{v_{y,\alpha}^2}$ and

$$\overline{v_{x,\alpha}^2} = \rho_\alpha^{-1} \int_{\mathrm{FS}_\alpha} d\mathbf{k}_\alpha \frac{v_{x,\mathbf{k}_\alpha}^2}{v_{\mathbf{k}_\alpha}} \tag{5.13}$$

with $v_{\mathbf{k}_\alpha} = \sqrt{v_{x,\mathbf{k}_\alpha}^2 + v_{y,\mathbf{k}_\alpha}^2}$. As an illustrative remark, we note that, for the simple case of a uniform $\tilde{v}_{\mathbf{k}_\alpha} = v$ on all bands, the formula would simplify to

$$H_{c,2} = 2\pi e^{-\gamma} \frac{\Phi_0}{\hbar^2 v^2} T_c^2. \tag{5.14}$$

The prediction of this ratio as a function of strain for even and odd-parity OPs is given in Fig. 5.8. In the odd-parity (even-parity) case, the ratio decreases (increases) by a factor of ~ 2 at the vHS compared to its zero-strain value. As explained above, $H_{c,2}/T_c^2$ is proportional to a weighted average of the inverse Fermi velocity squared, where the weight is given by the magnitude of the gap. The increase of this ratio in the even-parity case is easily explained by the contribution from the vanishing velocity at the Van Hove point, since the gap is non-zero at that point. In contrast, the odd-parity gap is zero at the Van Hove point and its upper critical field therefore cannot benefit from this effect. Furthermore, the odd-parity gap can be seen in Fig. 5.7 to become smaller on $\boldsymbol{\gamma}$ and larger on $\boldsymbol{\alpha}$ and $\boldsymbol{\beta}$ close to the vHS. Since $\boldsymbol{\alpha}$ and $\boldsymbol{\beta}$ have larger Fermi velocities, this leads to a reduction of $H_{c,2}/T_c^2$.

Interestingly, the critical field and critical temperature measured experimentally are given by $H_{c,2} = 75$ mT and $T_c = 1.5$ K at zero strain and $H_{c,2} = 1.5$ T and $T_c = 3.4$ K at ϵ_{vHS} [11]. This leads to an increase of $H_{c,2}/T_c^2$ by a factor of ~ 4 at the vHS compared to the zero-strain value. This increase therefore seems qualitatively in

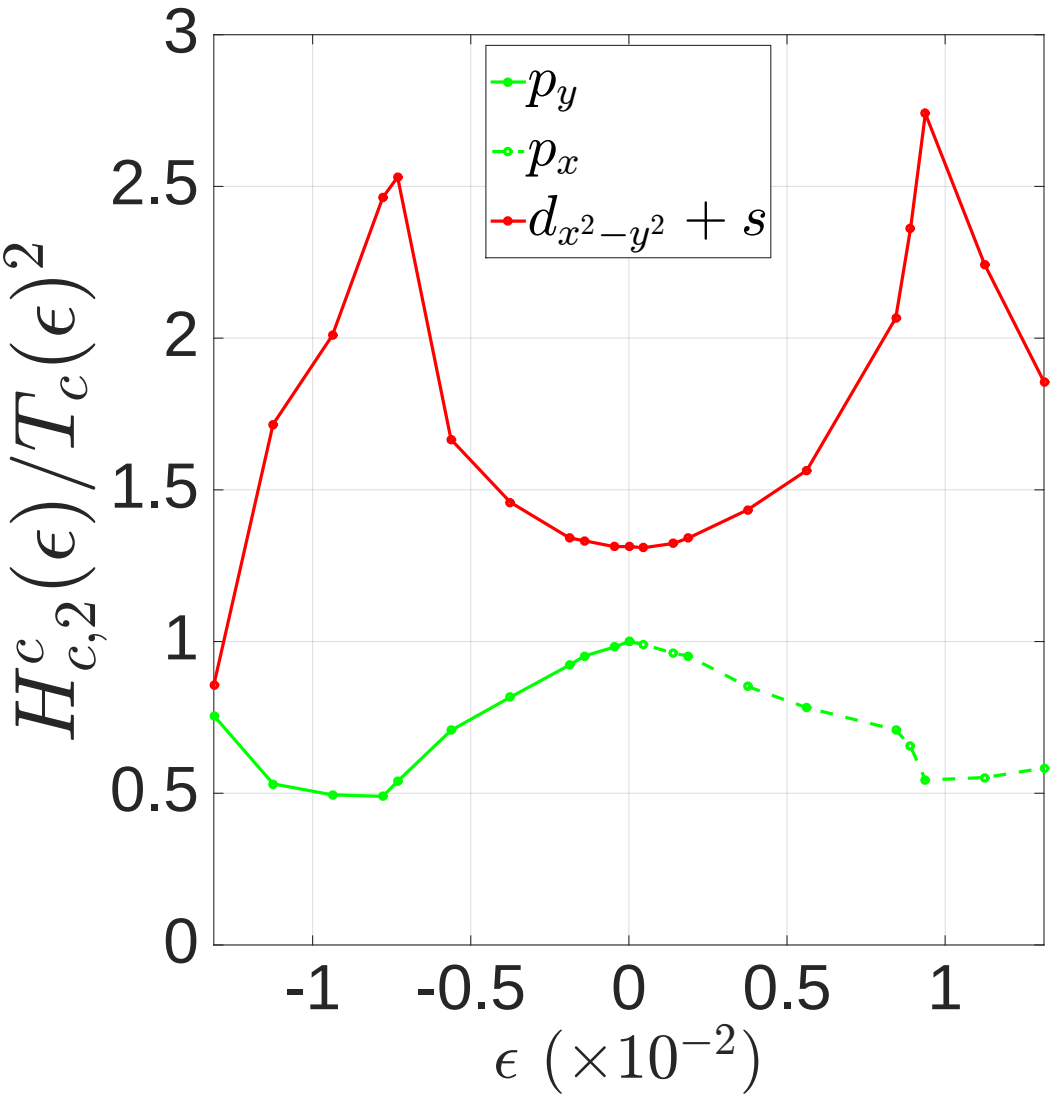

Figure 5.8: $H_{c,2}/T_c^2$ for $J/U = 0.06$. The results are normalized by the value at zero strain for the odd-parity order parameter. The green curve gives $H_{c,2}/T_c^2$ for the highest-T_c odd parity order parameter at any given strain, which is in the p_y representation under compression and in the p_x representation under tension.

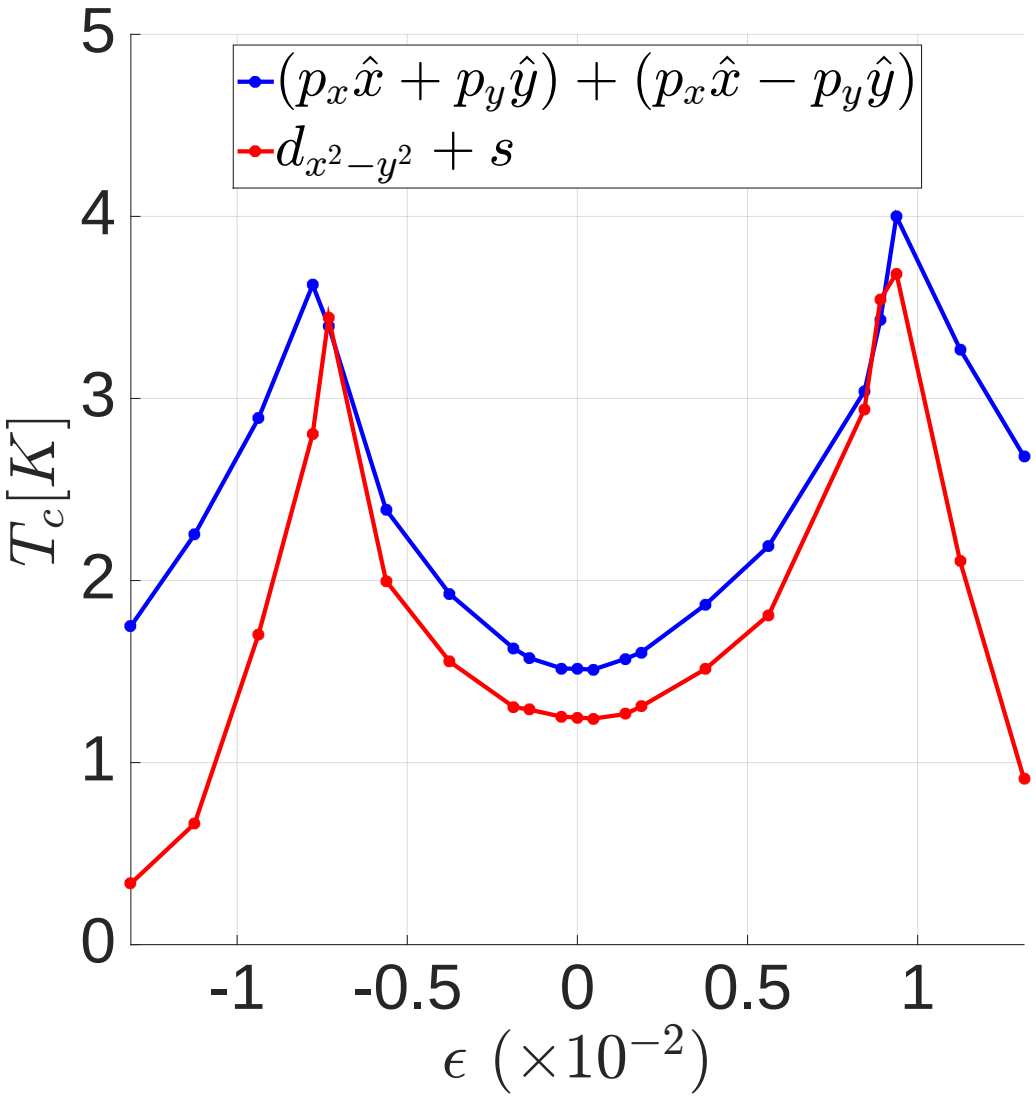

Figure 5.9: T_c versus strain for the highest-T_c even and odd-parity order parameters for $J/U = 0.08$.

agreement with an even-parity order parameter. According to Fig. 5.8, if a transition from odd-parity to even-parity were to occur at finite strain, there should be a jump of $H_{c,2}/T_c^2$ at the transition. It would therefore be extremely interesting to measure this ratio for the entire strain range.

The absolute value of $H_{c,2}/T_c^2$ can also be compared with experiments. Using the experimental value of the average Fermi velocity given in Ref. [1] to set the value of t in our model and using Eq. 5.11, we obtain an estimate for $H_{c,2}/T_c^2$ given by ~ 0.016 T/K^2 at zero strain. The corresponding experimental value is given by ~ 0.033 T/K^2.

5.3.2 Helical case

We now discuss the results for $J/U = 0.08$, in which case the zero-strain highest-T_c state is a helical state in the $p_x\hat{x} + p_y\hat{y}$ representation, as explained in Chapter 3. While, in the chiral case, there was a very small but finite cusp of T_c at zero strain, there is no such cusp for the helical state since it is a one-dimensional representation and the corresponding eigenvalue is therefore non-degenerate. Apart from this, as seen in Fig. 5.9, the evolution of T_c with strain is similar to the case of $J/U = 0.06$. At finite strain, the odd-parity order parameter is in the A_{1u} representation of D_{2h} (see Table 5.2), which is obtained by mixing the representations $p_x\hat{x}+p_y\hat{y}$ and $p_x\hat{x}-p_y\hat{y}$ of D_{4h}. The highest-T_c even-parity order parameter is in the same representation as for $J/U = 0.06$, and becomes a strong competitor close to the vHS. As seen in Fig. 5.11, the ratio $H_{c,2}/T_c^2$ is already two times larger for the even-parity order parameter than for the odd-parity one at zero strain. This is due to the fact that the even-parity gap is larger on $\boldsymbol{\gamma}$, which has a larger density of states, while the helical gap is larger on $\boldsymbol{\alpha}$ and $\boldsymbol{\beta}$. This can be seen in Fig. 5.10 which shows the momentum space structure of the even and odd-parity order parameters. The ratio $H_{c,2}/T_c^2$ increases by a factor of ~ 2 with strain for the even-parity gap, while it is fairly flat for the helical gap. While a measurement of this ratio for the entire strain range would be required to reach a conclusion, the experimental measurement of an increase of this ratio by a factor of 4 at the vHS [11] seems again in agreement with an even-parity order parameter.

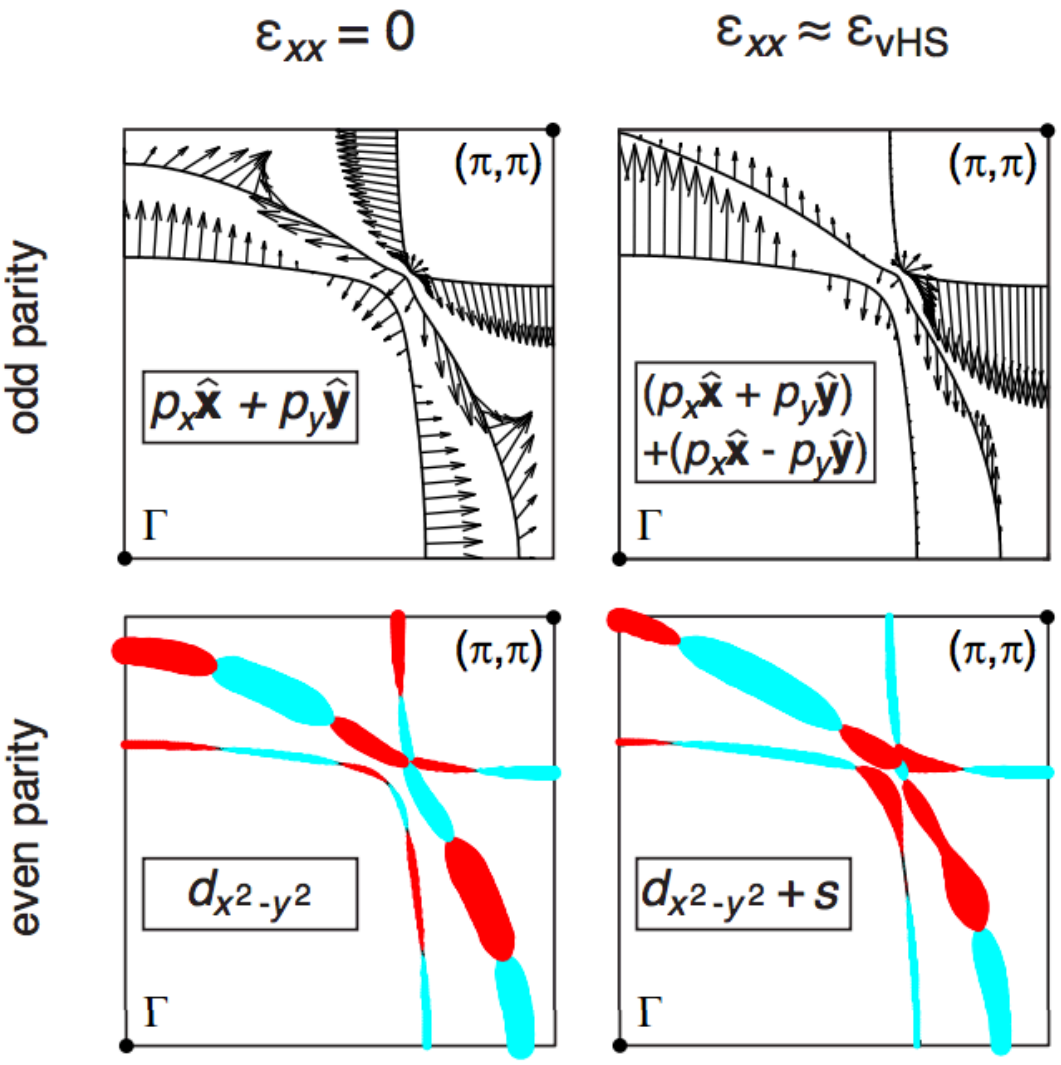

Figure 5.10: Order parameters for $J/U = 0.08$ at $\epsilon = 0$ and $\epsilon \simeq \epsilon_{vHS}$. Top: odd-parity order parameter $\vec{d}(\mathbf{k})$. Bottom: even-parity order parameter $\Delta_s(\mathbf{k})$. The width of the traces is proportional to the gap magnitude and the colour indicates the sign.

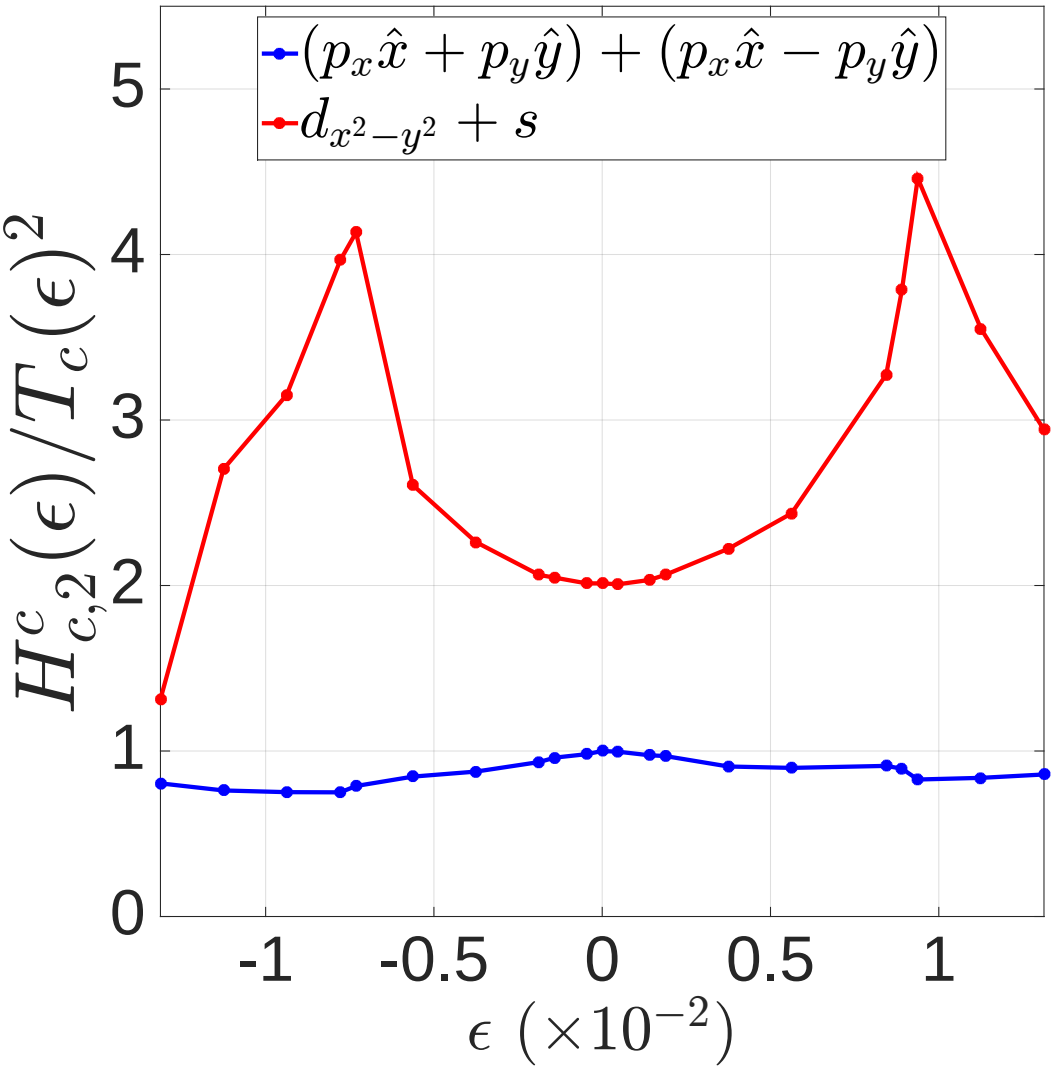

Figure 5.11: $H_{c,2}/T_c^2$ as a function of strain for $J/U = 0.08$. The results are normalised by the value at zero strain for the odd-parity order parameter.

5.4 Conclusion

In this Chapter, we used the weak coupling calculation developed in Chapter 2 to study the evolution of superconductivity in Sr_2RuO_4 under uniaxial $\langle 100 \rangle$ strain. In agreement with experiments, we found that the curve of T_c versus strain is relatively flat at zero strain, shows a large increase at higher strain that is fairly symmetric between compressive and tensile strain, and exhibits a peak when the $\boldsymbol{\gamma}$ band goes through a Lifshitz transition. Although even-parity T_c is lower than odd-parity T_c at zero strain, it has a larger relative increase with strain and becomes a strong competitor close to the vHS. This different behaviour comes from the fact that the odd-parity gap has to vanish at the Van Hove point by symmetry, while this is not the case for the even-parity gap. This leads to a markedly different evolution of the ratio $H_{c,2}/T_c^2$ under strain: it increases (decreases) for the even (odd-)parity order parameter. Since an increase by a factor of ~ 4 of this ratio was measured between the zero-strain value and the value at the vHS, this suggests a possible transition from an odd to an even-parity order parameter at finite strain.

6. Conclusion

Even though superconductivity was discovered more than a century ago, the study of this phenomenon has continuously generated extremely important concepts in theoretical physics, and is still a very active field of research. In particular, the study of unconventional superconductors has led to the development of very fruitful theoretical tools, from the resonating valence bond model [23] to the functional renormalization group [92], and has brought new light on the long-standing problem of the understanding of strongly correlated electrons. Another extremely active field of condensed matter physics is the study of gapped phases of matter with highly robust, "topological" properties [35]. As explained in Chapter 1, Sr_2RuO_4 occupies a very special place in the class of unconventional superconductors since it is a candidate for $p_x \pm ip_y$ topological superconductivity and therefore lies at the intersection of these two fields.

For most unconventional superconductors, the conduction electrons occupy bands formed by the hybridization of certain atomic d orbitals of transition metal elements. In several cases, like for pnictides and ruthenates, this leads to multiple bands at the Fermi level with a momentum-dependent orbital content. Furthermore, especially for $4d$ and $5d$ transition metals, spin-orbit coupling is non-negligible and leads to some non-trivial momentum-dependent spin-orbital texture of the electronic structure. In Chapter 2, we presented a perturbative theory of superconductivity that can be applied to such a multi-orbital, spin-orbit coupled system. This theory relies on the assumption of a weak interaction compared to the bandwidth. Given a microscopic tight-binding Hamiltonian and a multi-orbital Hubbard-type interaction, this technique leads to a prediction for the highest T_c superconducting order parameters, which can be classified according to the irreducible representations of the point group of the lattice. Useful tools present in the $SU(2)$-symmetric case were generalised in terms of pseudo-spin for the spin-orbit coupled case.

In Chapter 3, after having introduced a three-orbital, spin-orbit coupled Hubbard-

type Hamiltonian for Sr_2RuO_4, we applied the above technique to study the possible superconducting order parameters. We found an odd-parity highest-T_c mode favoured over most of parameter space. Depending on the parameters, this order parameter can either be chiral, a time-reversal symmetry breaking state with chiral Majorana edge modes, or helical, a time-reversal invariant state with counter-propagating Majorana edge modes. In both cases, the gap is highly anisotropic, and has accidental deep minima along certain directions, in accordance with the absence of exponential decay below T_c of the specific heat and of other quantities. Taking advantage of the multi-band nature of our calculation, we showed that the gap is of similar size on all three bands over a finite region of parameter space, and we compared with experiments our prediction for the jump in specific heat at T_c.

In Chapter 4, we studied the chiral order parameters obtained previously. We showed that the $\boldsymbol{\beta}$ and $\boldsymbol{\gamma}$ bands have a Chern number of -3 instead of the usually assumed $+1$. Since the low temperature thermal Hall conductance is proportional to this number, this leads to a drastically different prediction for this quantity. We then studied the charge Hall conductance, whose value is not quantized in a superconductor, and showed that its value is typically smaller by two to three orders of magnitude for our chiral order parameter compared to previous predictions.

In Chapter 5, the evolution of superconductivity in Sr_2RuO_4 under $\langle 100 \rangle$ uniaxial strain was studied. This type of strain is particularly interesting for two reasons: (1) it breaks the $x \leftrightarrow y$ symmetry and therefore splits the degeneracy between the two components of a chiral order parameter, and (2) it can take the $\boldsymbol{\gamma}$ band through a Lifshitz transition, which causes a Van Hove singularity in the density of states. Because of the aforementioned breaking of symmetry, T_c of a chiral state should exhibit a cusp at zero strain, while no such cusp is expected for a one-dimensional order parameter, like a helical state for example. We showed that, within our model, this cusp in the chiral case is typically very small, thereby potentially reconciling the presence of a chiral state with the absence of measurable cusp reported experimentally. Furthermore, we calculated the evolution of T_c at larger strain across the Lifshitz transition for the different symmetry channels. Both even and odd-parity order parameters are

predicted to exhibit a maximum of T_c at the Lifshitz transition, in accordance with experiments. While even-parity order parameters have lower T_c at zero strain, they experience a larger relative increase in T_c with strain, and become strong competitors close to the Lifshitz transition. This larger relative increase for even-parity order parameters is due to the fact that odd-parity gaps have a nodal point at the Van Hove points $(\pi, 0)$ and $(0, \pi)$, while even-parity gaps do not. Finally, we proposed the ratio $H_{c,2}/T_c^2$, where $H_{c,2}$ is the zero temperature critical field for out-of-plane fields, as an experimental measure of the evolution of the density of states at momenta where the gap is the largest. We predicted an increase with strain of this ratio for an even-parity gap and a decrease for an odd-parity gap. The only two experimental measurements available at the time of the writing, one at zero strain and one at the maximum of T_c under compression, show an increase of this ratio with strain, which therefore seems to point to an even-parity order parameter.

While a $p_x \pm ip_y$ superconducting state is in agreement with the experimental signatures of time-reversal symmetry breaking, at the beginning of this work, three experiments seemed, at least at first sight, at odds with such a scenario: (1) the power law behaviour of specific heat and other quantities below T_c (since $p_x \pm ip_y$ gaps do not have symmetry-imposed nodes), (2) the absence of measurable edge currents and (3) the absence of cusp of T_c at zero strain. In this work, we showed that each of these experiments is actually not incompatible with a chiral state, thereby giving more ground to the $p_x \pm ip_y$ scenario.

Yet, the issue is far from settled, and a lot of important questions remain. First, while the presence of deep gap minima explains the power law behaviour of specific heat and other quantities like acoustic attenuation and penetration depth, it only does so for $T > T_{\min}$, where $T_{\min}$ is given by the minimum of the gap magnitude. Below $T_{\min}$, one would expect an exponential decay of these quantities, which was never observed, even down to very low temperature ($T/T_c \sim 1/30$). There are two possibilities: either (1) the gap has symmetry-imposed nodes, which can only happen for an even-parity gap as can be seen from examining the different irreducible representations of D_{4h}, or (2) one should include the contribution of other low-lying

excitations than particle-hole excitations. In the pseudo-spin triplet case, these excitations could be spin waves, which could be very soft since NMR results point towards a very weakly pinned $\vec{d}$, or gapless Majorana modes running through dislocations and edges.

Second, the ratio $H_{c,2}^{ab}/H_{c,2}^{c}$, where $H_{c,2}^{ab}$ ($H_{c,2}^{c}$) is the zero temperature in-plane (out-of-plane) critical field, is 20, which is about 3 times smaller than the intrinsic anisotropy of superconductivity measured by scattering neutrons on the vortex lattice [85, 86]. For an orbital-limited transition, these two ratios are usually in good agreement. This seems to suggest that the breaking of superconductivity under in-plane fields is not caused by the orbital motion of electrons. Furthermore, the superconducting transition under in-plane fields becomes first-order at low temperature [84]. This phenomenology is analogous to the one of Pauli limiting, where superconductivity is killed by the Zeeman splitting of the electrons that form Cooper pairs [42]. If we were to sloppily replace pseudo-spins by spins, we would find that such a Pauli limiting effect for in-plane fields could only appear for a singlet, or for a triplet with $\vec{d}$ strongly pinned in-plane. This scenario is nevertheless inconsistent with NMR and neutron experiments which show no decrease of the spin susceptibility in the superconducting state. This issue motivates the study of (1) the impact of Zeeman coupling on a spin-orbit coupled superconductor and (2) the impact of the non-zero k_z dispersion and three-dimensional effects, which are crucial to study the mixed state under in-plane fields.

Finally, given its usefulness in the study of Sr_2RuO_4, it would be interesting to use the scheme presented in this thesis to study unconventional superconductivity in other spin-orbit coupled, multi-band materials, like FeSe and SrPtAs for example.

Bibliography

[1] A. P. Mackenzie and Y. Maeno, Rev. Mod. Phys. **75**, 657 (2003).

[2] A. P. Schnyder, S. Ryu, A. Furusaki, and A. W. Ludwig, Physical Review B **78**, 195125 (2008).

[3] A. Damascelli, D. H. Lu, K. M. Shen, N. P. Armitage, F. Ronning, D. L. Feng, C. Kim, Z.-X. Shen, T. Kimura, Y. Tokura, Z. Q. Mao, and Y. Maeno, Phys. Rev. Lett. **85**, 5194 (2000).

[4] C. N. Veenstra, Z.-H. Zhu, B. Ludbrook, M. Capsoni, G. Levy, A. Nicolaou, J. A. Rosen, R. Comin, S. Kittaka, Y. Maeno, I. S. Elfimov, and A. Damascelli, Phys. Rev. Lett. **110**, 097004 (2013).

[5] S. Raghu, S. B. Chung, and S. Lederer, Journal of Physics: Conference Series **449**, 012031 (2013).

[6] X.-L. Qi, T. L. Hughes, S. Raghu, and S.-C. Zhang, Phys. Rev. Lett. **102**, 187001 (2009).

[7] M. H. Fischer and E. Berg, Phys. Rev. B **93**, 054501 (2016).

[8] S. Nishizaki, Y. Maeno, and Z. Mao, Journal of the Physical Society of Japan **69**, 572 (2000).

[9] I. A. Firmo, S. Lederer, C. Lupien, A. P. Mackenzie, J. C. Davis, and S. A. Kivelson, Phys. Rev. B **88**, 134521 (2013).

[10] C. W. Hicks, D. O. Brodsky, E. A. Yelland, A. S. Gibbs, J. A. N. Bruin, M. E. Barber, S. D. Edkins, K. Nishimura, S. Yonezawa, Y. Maeno, and A. P. Mackenzie, Science **344**, 283 (2014).

[11] A. Steppke, L. Zhao, M. E. Barber, T. Scaffidi, F. Jerzembeck, H. Rosner, A. S. Gibbs, Y. Maeno, S. H. Simon, A. P. Mackenzie, and C. W. Hicks, ArXiv e-prints (2016), arXiv:1604.06669 [cond-mat.supr-con] .

[12] J. F. Annett, Advances in Physics **39**, 83 (1990).

[13] R. Balian and N. R. Werthamer, Phys. Rev. **131**, 1553 (1963).

[14] P. W. Anderson and P. Morel, Phys. Rev. **123**, 1911 (1961).

[15] P. W. Anderson and W. F. Brinkman, Phys. Rev. Lett. **30**, 1108 (1973).

[16] H. K. Onnes, Commun. Phys. Lab. Univ. Leiden **12**, 1 (1911).

[17] J. Bardeen, L. N. Cooper, and J. R. Schrieffer, Phys. Rev. **108**, 1175 (1957).

[18] D. D. Osheroff, R. C. Richardson, and D. M. Lee, Phys. Rev. Lett. **28**, 885 (1972).

[19] G. R. Stewart, Rev. Mod. Phys. **56**, 755 (1984).

[20] Jerome, D., Mazaud, A., Ribault, M., and Bechgaard, K., J. Physique Lett. **41**, 95 (1980).

[21] S. S. P. Parkin, E. M. Engler, R. R. Schumaker, R. Lagier, V. Y. Lee, J. C. Scott, and R. L. Greene, Phys. Rev. Lett. **50**, 270 (1983).

[22] J. G. Bednorz and K. A. Müller, Zeitschrift für Physik B Condensed Matter **64**, 189 (1986).

[23] P. W. Anderson, Science **235**, 1196 (1987).

[24] C. C. Tsuei and J. R. Kirtley, Rev. Mod. Phys. **72**, 969 (2000).

[25] Y. Maeno, H. Hashimoto, K. Yoshida, S. Nishizaki, T. Fujita, J. Bednorz, and F. Lichtenberg, Nature **372**, 532 (1994).

[26] T. M. Rice and M. Sigrist, Journal of Physics: Condensed Matter **7**, L643 (1995).
[27] A. J. Leggett, Rev. Mod. Phys. **47**, 331 (1975).
[28] C. Buzea and T. Yamashita, Superconductor Science and Technology **14**, R115 (2001).
[29] G. R. Stewart, Rev. Mod. Phys. **83**, 1589 (2011).
[30] C. Nayak, S. H. Simon, A. Stern, M. Freedman, and S. Das Sarma, Rev. Mod. Phys. **80**, 1083 (2008).
[31] J. Jang, D. G. Ferguson, V. Vakaryuk, R. Budakian, S. B. Chung, P. M. Goldbart, and Y. Maeno, Science **331**, 186 (2011).
[32] V. L. Ginzburg and L. D. Landau, Zh. Eksp. Teor. Fiz. **20**, 1064 (1950).
[33] D. J. Thouless, M. Kohmoto, M. P. Nightingale, and M. den Nijs, Phys. Rev. Lett. **49**, 405 (1982).
[34] C. L. Kane and E. J. Mele, Phys. Rev. Lett. **95**, 146802 (2005).
[35] X.-L. Qi and S.-C. Zhang, Rev. Mod. Phys. **83**, 1057 (2011).
[36] A. Kitaev, AIP Conference Proceedings **1134**, 22 (2009).
[37] S. Ryu, A. P. Schnyder, A. Furusaki, and A. W. W. Ludwig, New Journal of Physics **12**, 065010 (2010).
[38] N. Read and D. Green, Phys. Rev. B **61**, 10267 (2000).
[39] A. Kitaev, Annals of Physics **321**, 2 (2006), january Special Issue.
[40] J. Garaud, D. F. Agterberg, and E. Babaev, Phys. Rev. B **86**, 060513 (2012).
[41] A. J. Leggett, Progress of Theoretical Physics **36**, 901 (1966).
[42] M. Tinkham, *Introduction to Superconductivity: Second Edition*, Dover Books on Physics (Dover Publications, 2004).
[43] Y. Maeno, S. Kittaka, T. Nomura, S. Yonezawa, and K. Ishida, Journal of the Physical Society of Japan **81**, 011009 (2012).
[44] C. Kallin and J. Berlinsky, Reports on Progress in Physics **79**, 054502 (2016).
[45] K. Ishida, H. Mukuda, Y. Kitaoka, Z. Q. Mao, Y. Mori, and Y. Maeno, Phys. Rev. Lett. **84**, 5387 (2000).
[46] M. A. Tanatar, S. Nagai, Z. Q. Mao, Y. Maeno, and T. Ishiguro, Phys. Rev. B **63**, 064505 (2001).
[47] K. Izawa, H. Takahashi, H. Yamaguchi, Y. Matsuda, M. Suzuki, T. Sasaki, T. Fukase, Y. Yoshida, R. Settai, and Y. Onuki, Phys. Rev. Lett. **86**, 2653 (2001).
[48] C. Lupien, W. A. MacFarlane, C. Proust, L. Taillefer, Z. Q. Mao, and Y. Maeno, Phys. Rev. Lett. **86**, 5986 (2001).
[49] I. Bonalde, B. D. Yanoff, M. B. Salamon, D. J. Van Harlingen, E. M. E. Chia, Z. Q. Mao, and Y. Maeno, Phys. Rev. Lett. **85**, 4775 (2000).
[50] D. F. Agterberg, T. M. Rice, and M. Sigrist, Phys. Rev. Lett. **78**, 3374 (1997).
[51] Y. Sidis, M. Braden, P. Bourges, B. Hennion, S. Nishizaki, Y. Maeno, and Y. Mori, Phys. Rev. Lett. **83**, 3320 (1999).
[52] T. Nomura and K. Yamada, Journal of the Physical Society of Japan **69**, 3678 (2000).
[53] K. Miyake and O. Narikiyo, Phys. Rev. Lett. **83**, 1423 (1999).
[54] M. E. Zhitomirsky and T. M. Rice, Phys. Rev. Lett. **87**, 057001 (2001).

[55] Q. H. Wang, C. Platt, Y. Yang, C. Honerkamp, F. C. Zhang, W. Hanke, T. M. Rice, and R. Thomale, EPL (Europhysics Letters) **104**, 17013 (2013).
[56] I. I. Mazin and D. J. Singh, Phys. Rev. Lett. **82**, 4324 (1999).
[57] T. Kuwabara and M. Ogata, Phys. Rev. Lett. **85**, 4586 (2000).
[58] M. Sato and M. Kohmoto, Journal of the Physical Society of Japan **69**, 3505 (2000).
[59] T. Takimoto, Phys. Rev. B **62**, R14641 (2000).
[60] K. Kuroki, M. Ogata, R. Arita, and H. Aoki, Phys. Rev. B **63**, 060506 (2001).
[61] S. Raghu, A. Kapitulnik, and S. A. Kivelson, Phys. Rev. Lett. **105**, 136401 (2010).
[62] S. B. Chung, S. Raghu, A. Kapitulnik, and S. A. Kivelson, Phys. Rev. B **86**, 064525 (2012).
[63] M. Tsuchiizu, Y. Yamakawa, S. Onari, Y. Ohno, and H. Kontani, Phys. Rev. B **91**, 155103 (2015).
[64] T. Nomura and K. Yamada, Journal of the Physical Society of Japan **71**, 404 (2002).
[65] K. Deguchi, Z. Q. Mao, H. Yaguchi, and Y. Maeno, Phys. Rev. Lett. **92**, 047002 (2004).
[66] K. Deguchi, Z. Q. Mao, and Y. Maeno, Journal of the Physical Society of Japan **73**, 1313 (2004).
[67] K. D. Nelson, Z. Q. Mao, Y. Maeno, and Y. Liu, Science **306**, 1151 (2004).
[68] K. Ishida, H. Mukuda, Y. Kitaoka, K. Asayama, Z. Mao, Y. Mori, and Y. Maeno, Nature **396**, 658 (1998).
[69] H. Murakawa, K. Ishida, K. Kitagawa, Z. Q. Mao, and Y. Maeno, Phys. Rev. Lett. **93**, 167004 (2004).
[70] J. A. Duffy, S. M. Hayden, Y. Maeno, Z. Mao, J. Kulda, and G. J. McIntyre, Phys. Rev. Lett. **85**, 5412 (2000).
[71] M. W. Haverkort, I. S. Elfimov, L. H. Tjeng, G. A. Sawatzky, and A. Damascelli, Phys. Rev. Lett. **101**, 026406 (2008).
[72] C. N. Veenstra, Z.-H. Zhu, M. Raichle, B. M. Ludbrook, A. Nicolaou, B. Slomski, G. Landolt, S. Kittaka, Y. Maeno, J. H. Dil, I. S. Elfimov, M. W. Haverkort, and A. Damascelli, Phys. Rev. Lett. **112**, 127002 (2014).
[73] C. G. Fatuzzo, M. Dantz, S. Fatale, P. Olalde-Velasco, N. E. Shaik, B. Dalla Piazza, S. Toth, J. Pelliciari, R. Fittipaldi, A. Vecchione, N. Kikugawa, J. S. Brooks, H. M. Rønnow, M. Grioni, C. Rüegg, T. Schmitt, and J. Chang, Phys. Rev. B **91**, 155104 (2015).
[74] G. Luke, Y. Fudamoto, K. Kojima, M. Larkin, J. Merrin, B. Nachumi, Y. Uemura, Y. Maeno, Z. Mao, Y. Mori, H. Nakamura, and M. Sigrist, Nature **394**, 558 (1998).
[75] J. Xia, Y. Maeno, P. T. Beyersdorf, M. M. Fejer, and A. Kapitulnik, Phys. Rev. Lett. **97**, 167002 (2006).
[76] F. Kidwingira, J. D. Strand, D. J. Van Harlingen, and Y. Maeno, Science **314**, 1267 (2006).
[77] K. Saitoh, S. Kashiwaya, H. Kashiwaya, Y. Mawatari, Y. Asano, Y. Tanaka, and Y. Maeno, Phys. Rev. B **92**, 100504 (2015).
[78] S. Kashiwaya, H. Kashiwaya, H. Kambara, T. Furuta, H. Yaguchi, Y. Tanaka, and Y. Maeno, Phys. Rev. Lett. **107**, 077003 (2011).

[79] M. Matsumoto and M. Sigrist, Journal of the Physical Society of Japan **68**, 994 (1999).
[80] J. R. Kirtley, C. Kallin, C. W. Hicks, E.-A. Kim, Y. Liu, K. A. Moler, Y. Maeno, and K. D. Nelson, Phys. Rev. B **76**, 014526 (2007).
[81] C. W. Hicks, J. R. Kirtley, T. M. Lippman, N. C. Koshnick, M. E. Huber, Y. Maeno, W. M. Yuhasz, M. B. Maple, and K. A. Moler, Phys. Rev. B **81**, 214501 (2010).
[82] T. Scaffidi and S. H. Simon, Phys. Rev. Lett. **115**, 087003 (2015).
[83] M. Sigrist, R. Joynt, and T. M. Rice, Phys. Rev. B **36**, 5186 (1987).
[84] S. Yonezawa, T. Kajikawa, and Y. Maeno, Phys. Rev. Lett. **110**, 077003 (2013).
[85] K. Deguchi, M. A. Tanatar, Z. Mao, T. Ishiguro, and Y. Maeno, Journal of the Physical Society of Japan **71**, 2839 (2002).
[86] C. Rastovski, C. D. Dewhurst, W. J. Gannon, D. C. Peets, H. Takatsu, Y. Maeno, M. Ichioka, K. Machida, and M. R. Eskildsen, Phys. Rev. Lett. **111**, 087003 (2013).
[87] M. Sigrist and K. Ueda, Rev. Mod. Phys. **63**, 239 (1991).
[88] S. Maiti and A. V. Chubukov, AIP Conference Proceedings **1550**, 3 (2013).
[89] W. Kohn and J. M. Luttinger, Phys. Rev. Lett. **15**, 524 (1965).
[90] R. Shankar, Rev. Mod. Phys. **66**, 129 (1994).
[91] D. J. Scalapino, Rev. Mod. Phys. **84**, 1383 (2012).
[92] W. Metzner, M. Salmhofer, C. Honerkamp, V. Meden, and K. Schönhammer, Rev. Mod. Phys. **84**, 299 (2012).
[93] A. Abanov, A. V. Chubukov, and J. Schmalian, Advances in Physics **52**, 119 (2003).
[94] J. Hubbard, Proceedings of the Royal Society of London A: Mathematical, Physical and Engineering Sciences **276**, 238 (1963).
[95] E. Dagotto, T. Hotta, and A. Moreo, Physics Reports **344**, 1 (2001).
[96] J. G. Rau, E. K.-H. Lee, and H.-Y. Kee, Annual Review of Condensed Matter Physics **7**, 195 (2016).
[97] H. Bruus and K. Flensberg, *Many-Body Quantum Theory in Condensed Matter Physics: An Introduction (Oxford Graduate Texts)* (Oxford University Press, 2004).
[98] E. E. Salpeter and H. A. Bethe, Phys. Rev. **84**, 1232 (1951).
[99] S. Raghu, S. A. Kivelson, and D. J. Scalapino, Phys. Rev. B **81**, 224505 (2010).
[100] M. Sigrist, AIP Conference Proceedings **789**, 165 (2005).
[101] P.-A. Lindgard, Solid State Communications **16**, 481 (1975).
[102] T. Mishonov and E. Penev, International Journal of Modern Physics B **16**, 3573 (2002).
[103] Y. Okuno and M. Sigrist, Journal of Superconductivity **12**, 563 (1999).
[104] J. M. Luttinger, Phys. Rev. **121**, 942 (1961).
[105] F. D. M. Haldane, Journal of Physics C: Solid State Physics **14**, 2585 (1981).
[106] L. Van Hove, Phys. Rev. **89**, 1189 (1953).
[107] P. G. Kealey, T. M. Riseman, E. M. Forgan, L. M. Galvin, A. P. Mackenzie, S. L. Lee, D. M. Paul, R. Cubitt, D. F. Agterberg, R. Heeb, Z. Q. Mao, and Y. Maeno, Phys. Rev. Lett. **84**, 6094 (2000).
[108] Y. Liu, New Journal of Physics **12**, 075001 (2010).

[109] M. S. Anwar, T. Nakamura, S. Yonezawa, M. Yakabe, R. Ishiguro, H. Takayanagi, and Y. Maeno, Scientific reports **3**, 2480 (2013).
[110] J. F. Annett, G. Litak, B. L. Györffy, and K. I. Wysokiński, Phys. Rev. B **73**, 134501 (2006).
[111] C. M. Puetter and H.-Y. Kee, EPL (Europhysics Letters) **98**, 27010 (2012).
[112] S. Takamatsu and Y. Yanase, Journal of the Physical Society of Japan **82**, 063706 (2013).
[113] C. Bergemann, A. Mackenzie, S. Julian, D. Forsythe, and E. Ohmichi, Advances in Physics **52**, 639 (2003).
[114] H. Kontani, T. Tanaka, D. S. Hirashima, K. Yamada, and J. Inoue, Phys. Rev. Lett. **100**, 096601 (2008).
[115] K. K. Ng and M. Sigrist, EPL (Europhysics Letters) **49**, 473 (2000).
[116] J. Mravlje, M. Aichhorn, T. Miyake, K. Haule, G. Kotliar, and A. Georges, Phys. Rev. Lett. **106**, 096401 (2011).
[117] L. Vaugier, H. Jiang, and S. Biermann, Phys. Rev. B **86**, 165105 (2012).
[118] A. P. Mackenzie, S. R. Julian, A. J. Diver, G. J. McMullan, M. P. Ray, G. G. Lonzarich, Y. Maeno, S. Nishizaki, and T. Fujita, Phys. Rev. Lett. **76**, 3786 (1996).
[119] L. P. Gor'kov, Sov. Phys. JETP **9**, 1364 (1959).
[120] J.-W. Huo, T. M. Rice, and F.-C. Zhang, Phys. Rev. Lett. **110**, 167003 (2013).
[121] M. Behrmann, C. Piefke, and F. Lechermann, Phys. Rev. B **86**, 045130 (2012).
[122] H. Mukuda, K. Ishida, Y. Kitaoka, K. Miyake, Z. Q. Mao, Y. Mori, and Y. Maeno, Phys. Rev. B **65**, 132507 (2002).
[123] Y. Yoshioka and K. Miyake, Journal of the Physical Society of Japan **78**, 074701 (2009).
[124] Y. Yanase and M. Ogata, Journal of the Physical Society of Japan **72**, 673 (2003).
[125] T. Nomura, Journal of the Physical Society of Japan **74**, 1818 (2005).
[126] I. Eremin, D. Manske, and K. H. Bennemann, Phys. Rev. B **65**, 220502 (2002).
[127] B. Béri, Phys. Rev. B **85**, 140501 (2012).
[128] G. E. Volovik, Soviet Journal of Experimental and Theoretical Physics Letters **70**, 609 (1999).
[129] M. Cheng, K. Sun, V. Galitski, and S. Das Sarma, Phys. Rev. B **81**, 024504 (2010).
[130] P. J. Curran, S. J. Bending, W. M. Desoky, A. S. Gibbs, S. L. Lee, and A. P. Mackenzie, Phys. Rev. B **89**, 144504 (2014).
[131] M. Ishikawa, Progress of Theoretical Physics **57**, 1836 (1977).
[132] N. D. Mermin and P. Muzikar, Phys. Rev. B **21**, 980 (1980).
[133] T. Kita, Journal of the Physical Society of Japan **67**, 216 (1998).
[134] A. Furusaki, M. Matsumoto, and M. Sigrist, Phys. Rev. B **64**, 054514 (2001).
[135] M. Stone and R. Roy, Phys. Rev. B **69**, 184511 (2004).
[136] J. A. Sauls, Phys. Rev. B **84**, 214509 (2011).
[137] Y. Tada, W. Nie, and M. Oshikawa, Phys. Rev. Lett. **114**, 195301 (2015).
[138] G. E. Volovik, JETP Letters **100**, 742 (2015).
[139] W. Huang, E. Taylor, and C. Kallin, Phys. Rev. B **90**, 224519 (2014).

[140] W. Huang, S. Lederer, E. Taylor, and C. Kallin, Phys. Rev. B **91**, 094507 (2015).
[141] C. Kallin and A. J. Berlinsky, Journal of Physics: Condensed Matter **21**, 164210 (2009).
[142] S. Raghu and S. A. Kivelson, Phys. Rev. B **83**, 094518 (2011).
[143] W. Cho, R. Thomale, S. Raghu, and S. A. Kivelson, Phys. Rev. B **88**, 064505 (2013).
[144] T. Scaffidi, J. C. Romers, and S. H. Simon, Phys. Rev. B **89**, 220510 (2014).
[145] Y. Ran, ArXiv e-prints (2010), arXiv:1006.5454 [cond-mat.str-el] .
[146] T. L. Hughes, H. Yao, and X.-L. Qi, Phys. Rev. B **90**, 235123 (2014).
[147] K. Yada, A. A. Golubov, Y. Tanaka, and S. Kashiwaya, Journal of the Physical Society of Japan **83**, 074706 (2014).
[148] H. Sumiyoshi and S. Fujimoto, Journal of the Physical Society of Japan **82**, 023602 (2013).
[149] J. Sauls, Advances in Physics **43**, 113 (1994).
[150] A. Bouhon and M. Sigrist, Phys. Rev. B **90**, 220511 (2014).
[151] S. Lederer, W. Huang, E. Taylor, S. Raghu, and C. Kallin, Phys. Rev. B **90**, 134521 (2014).
[152] G. D. Mahan, *Many-Particle Physics*, 2nd ed. (Plenum, New York, N.Y., 1993).
[153] P. E. C. Ashby and C. Kallin, Phys. Rev. B **79**, 224509 (2009).
[154] Y. Imai, K. Wakabayashi, and M. Sigrist, Phys. Rev. B **85**, 174532 (2012).
[155] Y. Imai, K. Wakabayashi, and M. Sigrist, Phys. Rev. B **88**, 144503 (2013).
[156] R. Joynt and L. Taillefer, Rev. Mod. Phys. **74**, 235 (2002).
[157] A. P. Mackenzie, R. K. W. Haselwimmer, A. W. Tyler, G. G. Lonzarich, Y. Mori, S. Nishizaki, and Y. Maeno, Phys. Rev. Lett. **80**, 161 (1998).
[158] R. M. Ribeiro, V. M. Pereira, N. M. R. Peres, P. R. Briddon, and A. H. C. Neto, New Journal of Physics **11**, 115002 (2009).
[159] H. Kusunose, Phys. Rev. B **70**, 054509 (2004).